Synchronization Dynamics of Coupled Chemical Oscillators

A Dissertation

Presented to

The Faculty of the Graduate School of Arts and Sciences

Brandeis University

Physics Department

Seth Fraden, Advisor

In Partial Fulfillment

of the Requirements for the Degree

Doctor of Philosophy

by

Nathan Tompkins

May, 2015

This dissertation, directed and approved by Nathan Tompkins's committee, has been accepted and approved by the Graduate Faculty of Brandeis University in partial fulfillment of the requirements for the degree of:

DOCTOR OF PHILOSOPHY

Eric Chasalow, Dean of Arts and Sciences

Dissertation Committee:

Seth Fraden, Chair

Michael F. Hagan, Physics Department

Irving R. Epstein, Chemistry Department

For my family.

Acknowledgments

Thank you to my advisor for years of guidance and support.

Thank you to my comrades-in-lab for years of collaboration and commiseration.

Thank you to my professors for years of discussion and advice.

Thank you to my family for years of love and patience.

Thank you to Sara for all of the above and so much more.

Abstract

Synchronization Dynamics of Coupled Chemical Oscillators

A dissertation presented to the Faculty of
the Graduate School of Arts and Sciences of
Brandeis University, Waltham, Massachusetts

by Nathan Tompkins

The synchronization dynamics of complex networks have been extensively studied over the past few decades due to their ubiquity in the natural world. Prominent examples include cardiac rhythms, circadian rhythms, the flashing of fireflies, predator/prey population dynamics, mammalian gait, human applause, pendulum clocks, the electrical grid, and of the course the brain. Detailed experiments have been done to map the topology of many of these systems and significant advances have been made to describe the mathematics of these networks. Compared to these bodies of work relatively little has been done to directly test the role of topology in the synchronization dynamics of coupled oscillators. This Dissertation develops technology to examine the dynamics due to topology within networks of discrete oscillatory components. The oscillatory system used here consists of the photo-inhibitable Belousov-Zhabotinsky (BZ) reaction water-in-oil emulsion where the oscillatory drops are diffusively coupled to one another and the topology is defined by the geometry of the diffusive connections. Ring networks are created from a close-packed 2D array of drops using the Programmable Illumination Microscope (PIM) in order to test Turing's theory of morphogenesis directly. Further technology is developed to create custom planar networks of BZ drops in more complicated topologies which can be individually perturbed using illumination from the PIM. The work presented here establishes the validity of using the BZ emulsion system with a PIM to study the topology induced effects on the synchronization dynamics of coupled chemical oscillators, tests the successes and limitations of Turing's theory of morphogenesis, and develops new technology to further probe the effects of network topology on a system of coupled oscillators. Finally, this Dissertation concludes by describing ongoing experiments which utilize this new technology to examine topology induced transitions of synchronization dynamics of diffusively coupled chemical oscillators.

Contents

List of Tables

List of Figures

Chapter 1

Introduction

In the natural world networks of coupled oscillators are ubiquitous with notable biological, physiological, and behavioral systems along with artifactual mechanical and electrical networks. Examples include the flashing of fireflies [49, 109], circadian, cardiac, and pulmonary rhythms [136], the synchronization of spontaneous applause [81], human gait [110], pendulum clocks [82], metronomes [89], the electrical power grid [93, 18], and coupled transistors [70]. The mathematics to study these networks is very advanced [87, 91, 107, 53, 42] with significant theoretical work focused on synchronization [108, 2, 6, 5] and on control algorithms for the dynamics of networks [50, 96, 97, 62, 30]. Recent work has highlighted the advantage of examining the effects of the topology of component networks to better understand the dynamics of networks at large [94]. This Dissertation develops technology such as the Programmable Illumination Microscope (PIM) to examine the effects of topology on networks of coupled oscillators, is applied to the ring networks explored theoretically by Alan Turing in 1952 [124], and develops further technology to study more complicated topologies.

The prototypical oscillatory chemical reaction for the study of coupled oscillators is the Belousov-Zhabotinsky (BZ) reaction [135, 143]. The BZ reaction is the metal ion catalyzed

oxidation of an organic acid which undergoes periodic oxidation and reduction [84, 25, 33, 34]. With the inclusion of the tris(bipyridine)ruthenium(II) (Rubpy) catalyst the BZ reaction is photo-inhibitable [31, 121]. The BZ reaction is the canonical system for studying coupled oscillators due to the mathematical models that accurately describe its behavior [26, 123, 129] and the availability of the constituent reagents. Numerous experimental systems have been created based on the BZ reaction including coupled tank reactors [65, 111, 55], catalyst-free beads [112, 115, 114] and posts [86, 72], micro-emulsions [127], and water-in-oil emulsions [117, 116, 13].

To study the synchronization dynamics due to topology an experimental system would need to able to create the desired topology (such as coupled tank reactors and catalyst-free beads or posts) while simultaneously being able to passively separate the rates of activational and inhibitory coupling (such as the emulsions). Separating the rates of activation and inhibition is possible for coupled tank reactors and catalyst-free beads or posts but these must be applied externally either chemically or optically using peristaltic pumps or light modulation. The separation of coupling rates in the emulsion systems is due to the preferential diffusion of non-polar species into the oil phase which is passive, continuous, and intrinsic. An additional electrochemical system has been used to study network topology [47, 46, 132, 133] but requires electrical connections between oscillatory nodes. In this Dissertation a variant of the BZ water-in-oil emulsion system is used [120] to develop new techniques for the creation of custom planar networks [118] in order to study the effects of topology on network dynamics using programmable illumination [119].

The main goal of this Dissertation is to study the synchronization dynamics of coupled chemical oscillators due to topology. Chapter 2 explores the background of this project including the chemical mechanism of the BZ reaction, an introduction to the mathematics of synchronization, a summary of experimental systems utilizing coupled BZ oscillators, a

brief overview of the instrumentation and materials used, and preliminary experiments that inspired the work performed here. Chapter 3 describes in detail the design and construction of the PIM which is the primary instrumentation used in this work. Chapter 4 reports on a direct test of Turing's mechanism for morphogenesis using the BZ water-in-oil emulsion system and the PIM developed here. Chapter 5 expands the methodology used here to enable the study of custom planar networks with fewer limitations than previous experiments. Finally, Chapter 6 concludes this Dissertation with a summary of what was studied here, the key developments and insights, a description of how this work advances the field, and an overview of experiments in progress that utilize these advances to continue exploring the effects of topology on the synchronization dynamics of coupled oscillators.

Chapter 2

Background

2.1 Belousov-Zhabotinsky Chemical Reaction

The oscillating system used in this work is the Belousov-Zhabotinsky (BZ) reaction, which is the prototypical nonlinear chemical oscillator. The BZ reaction is not a specific combination of chemicals but rather an entire family of reactions that share the same basic properties. The heart of the BZ reaction is the oxidation and bromination of an organic acid subtrate in the presence of a metal ion catalyst in an acidic environment. A BZ reaction then can consist of just four ingredients: an acidic environment for the reaction to take place (typically sulphuric acid), an organic acid substrate (typically citric acid or malonic acid), a bromate source (typically sodium bromate), and a metal ion catalyst (typically cerium, ferroin, or rubpy). In this work we use a six ingredient recipe consisting of 80 mM sulphuric acid (H_2SO_4), 400 mM malonic acid ($CH_2(COOH)_2$) (MA), 300 mM sodium bromate ($NaBrO_3$), 2.5 mM sodium bromide (NaBr), 3 mM ferroin ($Fe(phen)_3^{2+}$), and 1.2 mM rubpy ($Ru(bpy)_3^{2+}$). The specific concentrations used can vary slightly from experiment to experiment based on need but within a range of concentrations the specific value isn't critical. For example the malonic

acid concentration is sometimes used at 640 mM which results in a slightly longer period, the rubpy concentration is sometimes used at 0.4 mM which reduces the photosensitivity slightly, occasionally the rubpy is removed entirely to eliminate photosensitivity, and the initial sodium bromide concentration is sometimes used at 10 mM which lengthens the initial induction period slightly. Sodium bromide is added to obtain a nonzero initial concentration of Br^- (Br^- is created as part of the reaction so this changes only the initial conditions and not the reactions themselves) and our use of two catalysts is due to their unique properties. The color change of ferroin ($Fe(phen)_3^{2+}$) (red) to ferriin ($Fe(phen)_3^{3+}$) (blue) allows for easy monitoring of the chemical state of the system when viewed under green light (ferroin is opaque to green light while ferriin is transparent) and the rubpy catalyst can cause inhibition by exposure to blue light allowing for external inhibition of the reaction. The following sections outline the history and mechanism of the BZ reaction.

2.1.1 Belousov's "Supposedly Discovered Discovery"

The Belousov-Zhabotinsky reaction was first discovered unexpectedly in 1950 by a professor of Chemistry in the USSR, Boris Pavlovitch Belousov, who was attempting to study the Krebs cycle. His discovery however was ignored and even ridiculed by the scientific community of the time. It wasn't until 1961 that a young graduate student by the name of Anatol Zhabotinsky was assigned by his advisor to look into "a citric acid recipe of unknown origin" that the BZ reaction was taken seriously. Although Zhabotinsky kept Belousov updated by mail the two never met. Zhabotinsky's work was first introduced to the western world in 1967 and the oscillating reaction began to become known as the Zhabotinsky Reaction. It wasn't until the 1970s-1980s that the reaction became more commonly known as the the Belousov-Zhabotinsky Reaction. Belousov died in 1970 but in 1980 Belousov, Zhabotinsky,

Krinsky, and Ivanitsky were awarded the USSR's Lenin Prize in recognition for their work on the oscillatory reaction. The BZ reaction was largely introduced to the western scientific community by Arthur Winfree who met Zhabotinsky in 1968 at a scientific symposium in Prague. Despite the awarding of the 1980 Lenin Prize the full details of the discovery of the BZ reaction weren't known in the western world until 1981-83 when Winfree translated papers sent to him by Zhabotinsky. This paragraph is a brief summary of a 1984 article, *The prehistory of the Belousov-Zhabotinsky oscillator*, by Winfree [135].

2.1.2 Chemical Mechanism

Early observational experiments of BZ [143, 134] noted many interesting features of BZ, including that stirring induced synchronization within a tank reactor and the observation of traveling waves in an unstirred dish, but stopped short of delivering a description of the chemical mechanism responsible for the observed features. The first chemical mechanism proposed for the BZ reaction was the Field-Körös-Noyes (FKN) mechanism (Figure 2.1) [84, 25]. The FKN mechanism is a set of ten chemical reactions that demonstrate many of the key features of the BZ reaction but fails to replicate the reaction in its entirety. Combining the FKN mechanism with the ideas of the Brusselator [32] led to the creation of the first computational model of the BZ reaction, the Oregonator (Figure 2.2) [26]. The Oregonator is a three variable model with five reactions that reproduces many of the key features of the BZ reaction including limit cycle behavior.

Despite the success of the FKN mechanism and the Oregonator model these techniques yielded only an approximation to the experimental observations of BZ. A more detailed mechanism followed with the Györgyi-Turányi-Field (GTF) mechanism [33] and a further simplification of that with the subsequent GTF models [123]. The GTF mechanism consists

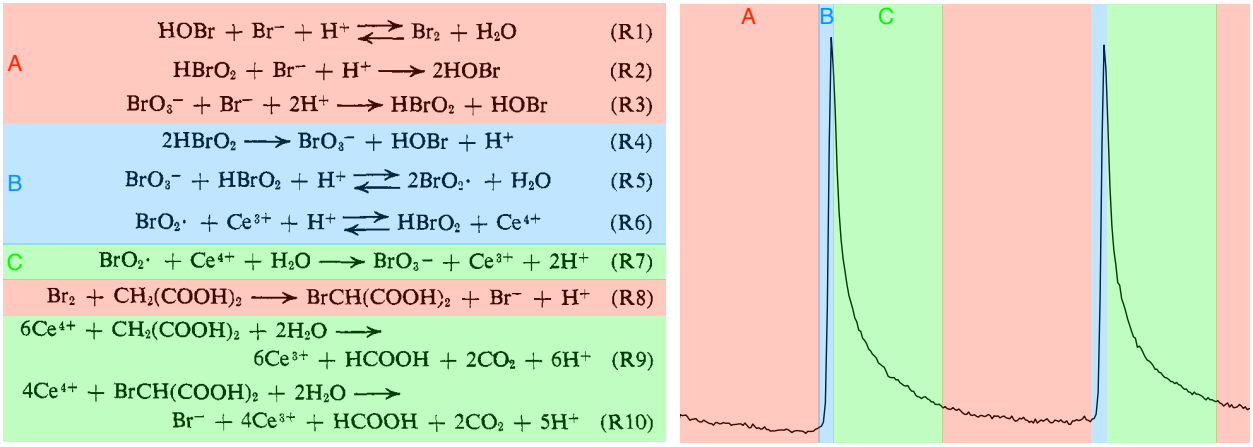

Figure 2.1: Left: The chemical reactions of the FKN mechanism. Right: An intensity trace of ferroin catalyzed BZ. These ten reactions collectively demonstrate the key features of the BZ reaction. The FKN mechanism can be generally split into three groups: Process A (red) of reactions 1, 2, 3, and 8; Process B (blue) of reactions 4, 5, and 6; and Process C (green) of reactions 7, 9, and 10. Process A is the slow reduction of bromate ion (BrO_3^-) by bromide ion (Br^-), Process B is the the rapid autocatalytic oxidation of cerium from Ce^{3+} to Ce^{4+}, and Process C is the relaxation of cerium from Ce^{4+} to Ce^{3+} that produces bromide ion. The oscillatory nature of the reactions arises from Process A lowering the concentration of bromide ion below a critical value that then shifts Process B to dominance which quickly oxidizes the cerium which as it relaxes via Process C raises the bromide ion level back above the critical value shifting the slow Process A back into dominance. During each oscillation some malonic acid is irreversibly oxidized and the reaction ceases when the supply of malonic acid is depleted. Image on left adapted from [25].

$$A + Y \rightleftharpoons X \qquad (M1)$$
$$X + Y \rightleftharpoons P \qquad (M2)$$
$$B + X \rightleftharpoons 2X + Z \qquad (M3)$$
$$2X \rightleftharpoons Q \qquad (M4)$$
$$Z \rightleftharpoons fY \qquad (M5)$$

Figure 2.2: The five reactions of the Oregonator. When equated to the BZ reaction the intermediate variables X, Y, Z are identified as the concentrations of the inhibitor, activator, and oxidized catalyst, respectively. In [26] the species are identified as relating to the FKN mechanism as $X = \mathrm{HBrO_2}$, $Y = \mathrm{Br^-}$, $Z = \mathrm{Ce(IV)}$, $A = B = \mathrm{BrO_3^-}$, and f is a stoichiometric factor of $f \sim 1$. In this model the concentration of malonic acid is considered a constant so the reaction will oscillate indefinitely. The exact forms of the reactions of the Oregonator and the species identifications have been modified over the years as can be seen in [19]. Image adapted from [26].

of 80 chemical reactions (42 in the simplified form) that offers a more accurate description of BZ than the FKN mechanism. The GTF models are three variable models like the Oregonator but in certain situations yield more accurate predictions. A different group proposed the Zhabotinsky-Buchholtz-Kiyatkin-Epstein (ZBKE) model [144] at around the same time as another alternative to the Oregonator. In 2001 Richard Field (the "F" of both FKN and GTF) and coworkers used the most recent experiments to create the 48 reaction Marburg-Budapest-Missoula (MBM) mechanism [34]. (Field is the "Missoula" of MBM.) The MBM mechanism is the best approximation yet to the BZ reaction. Each of these mechanisms added additional layers of complexity to become yet more detailed approximations but to date an absolute mechanism has yet to determined. Given the relative increase in complexity of each successive model compared to the increased accuracy of prediction the new models are used less frequently than their older counterparts. To date the FKN mechanism and Oregonator model are still most widely used in calculations.

Another widely used model of BZ is the Vanag-Epstein (VE) model (Equations D.1) which debuted in 2009 [129]. The VE model is based on the FKN mechanism and similar to the Oregonator but was created specifically for BZ emulsion systems. In addition to the activator (bromate, x), inhibitor (bromide, y), and oxidized catalyst (commonly ferriin, z) from the Oregonator the VE model includes the communicator of inhibition (bromine, u). The inclusion of bromine in the model is significant for in emulsion systems the non-polar diatomic bromine Br_2 is preferentially partitioned into the oil phase creating rapid diffusive inhibitory communication whereas the polar bromide ion Br^- is limited to the aqueous phase. Additionally the activator is able to weakly partition into the oil phase creating comparatively slow activational coupling and the catalyst is constrained to the aqueous phase. The end result of the VE model is a system with a separation of diffusion rates between the activator and inhibitor such as that described by Turing in 1952 [124].

2.2 The Mathematics of Synchronization

The mathematical study of synchronization which began with Christiaan Huygens [82] was largely ignored until the twentieth century [109]. Serious mathematical inquiries into synchronization were first conducted by Arthur Winfree [136], Bard Ermentrout [22], Nancy Kopell [49], Yoshiki Kuramoto [53], and later Steven Strogatz [107]. The term synchronization itself is often used in a few different ways. In some texts synchronization is used to refer to oscillations occurring simultaneously while in other texts synchronization merely means oscillating with a common frequency. This work will use the terminology of Kuramoto where a system is said to be *synchronized* if the oscillators are oscillating at a common frequency and thus *frequency locked*. The specific phase difference between synchronized oscillators will be used to define the attractor pattern for the system where the oscillations will be referred

to as *phase locked*. A system that is not synchronized will be undergoing *phase drift*. The degree of synchronization or frequency locking can be measured by defining a frequency order parameter. The degree of phase locking with a specific phase difference or attractor pattern can be measured by defining an order parameter.

2.2.1 Linearization, Phase Planes, and Limit Cycles

The study of synchronized systems is often made analytically intractable due to nonlinearities in the descriptive equations. A typical first approach is the linear approximation about fixed points. This Linear Stability Analysis (LSA) can determine the stability of the system and what to expect in regions near the fixed points but is severely limited in predictive abilities for the system as a whole. The greatest benefit from linearization is the ability to designate the system into a universality class (of which there are only seven) which tells you general properties but nothing specific or mechanistic. Another approach is to construct the n-dimensional phase plane of the system. Phase plane analysis allows for a detailed trajectory space for the different variables including the attractors they fall into. The key attractor for oscillatory systems is the limit cycle. Finding a stable limit cycle and its basin of attraction is a key test for any proposed set of descriptive equations. However all of these techniques are predicated upon *a priori* knowledge of the descriptive equations, something which is lacking for BZ. While different models such as the Oregonator have been proposed and analyzed showing a stable limit cycle these are but approximations for BZ. Another approach is Attractor Reconstruction which can yield a phase portrait from experimental data (Figure 2.3). Matching the limit cycles from proposed models to these reconstructions can and has been used to extract information about the fundamental nature of BZ.

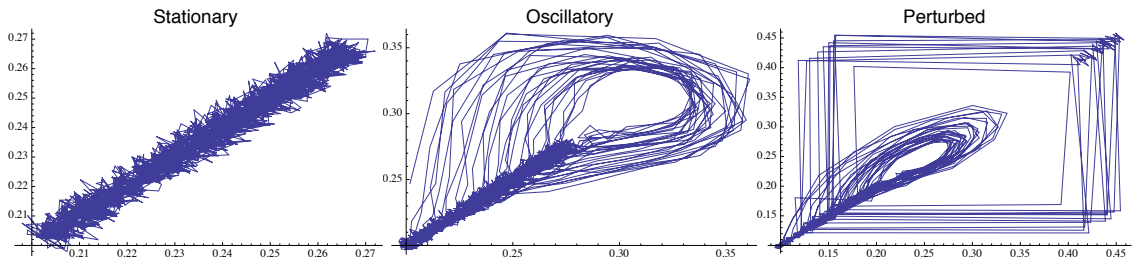

Figure 2.3: Attractor reconstructions from three different drops. The image on the left is from a drop in the stationary state, the image in the middle is from a drop in the unperturbed oscillatory state, and the image on the right is from a drop undergoing periodic perturbation. In all three images the gradual changes due the oxidation of malonic acid is present. The two images on the right demonstrate the limit cycle *like* behavior of the BZ reaction. The image on the far right shows the amplitude perturbations being applied. An attractor reconstruction is created from a single time series $f(t)$ by defining an attractor vector $v_\tau(t) = \{f(t), f(t+\tau)\}$ for some time step τ. The magnitude of the time step is arbitrary but should be small enough to have many steps per period while large enough to show noticeable change. For the above a τ of 6 seconds is used. The attractor vector can be generalized to an arbitrary number of dimensions as $v_\tau(t) = \{f(t), f(t+\tau), ..., f(t+N\tau)\}$ but such vectors are difficult to visualize.

2.2.2 Phase Oscillators, Entrainment, and Coupled Oscillators

The most general possible oscillator consists of three variables, an amplitude A, frequency ω, and phase θ. A general oscillator can be written $x = Af(\omega t + \theta)$ where f is a periodic (often nonlinear) function that describes the oscillator. A system of N of these oscillators then would be $x_i = A_i f(\omega_i t + \theta_i)$ for $i = 1...N$ where f is now a vector function. This system has a total of $3N$ variables but we can usually ignore some of them. A common approach is to ignore the amplitude terms A_i and focus instead on how the phases change in time. This then limits the system to N variables θ_i as the frequences ω_i are considered now constant parameters where $\omega_i = \frac{d\theta_i}{dt}$.

A convenient analogy that describes many of the observable features of such oscillators is a self-flushing toilet that has some sort of filling rate for the reservoir tank (either constant

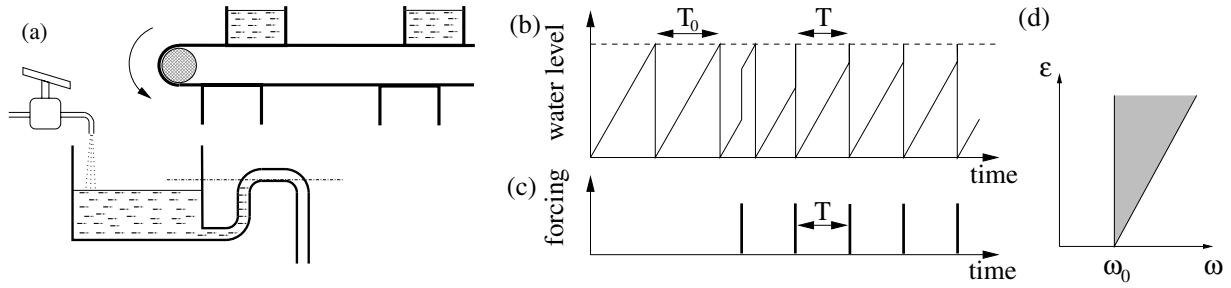

Figure 2.4: An illustration of the "self flushing toilet" analogy. Image (a) illustrates the physical mechanism of the oscillator with a conveyor belt for periodic entrainment. Images (b) and (c) demonstrate the phase of the oscillator before and during entrainment. In this illustration the entrainment period is shorter than the native period and the oscillator synchronizes with the forcing. Image (d) is a plot of the driving frequency ω versus the coupling amplitude ϵ. Since the addition of water is strictly excitatory (positive ϵ) the oscillator can only synchronize to an entrainment frequency greater than or equal to its native frequency ω_0. Image adapted from [91].

or dependent on the volume empty) that automatically flushes when the tank is filled. See Figure 2.4a for an illustration. The phase of system then would be the fraction of the reservoir tank that is filled. When the tank is empty the phase $\theta = 0$ and when the tank is filled $\theta = 2\pi$ and the system flushes returning to empty. The evolution of the phase is then described as $\frac{d\theta}{dt} = \omega$ and the system is described as a relaxation oscillator where the system slowly fills the reservoir tank before entering a brief flushing sequence.

With this analogy it is now easy to consider perturbations to the system as adding or removing water from the reservoir tank. The phase evolution is described as $\frac{d\theta}{dt} = \omega + \epsilon P(\theta)$ where ϵ is the additional water added to the tank (negative for water removed) and $P(\theta)$ is the phase response curve for the system. See Figure 2.4b-c. More generally a positive ϵ refers to excitatory perturbations and a negative ϵ refers to inhibitory perturbations. The phase response term comes from considering that the response of the system to added water will not always have the same effect depending on how full the tank was prior to perturbation. If

the tank was nearly full already the perturbation may be enough to initiate flushing while if the perturbation occurred during flushing it would have no effect at all. The phase response curve is often unknown and complicated and must be measured experimentally for each specific perturbation to each system.

Consider now a periodic perturbation of frequency Ω and phase Θ. At first lets assume $\Omega = \omega$ and that the phase difference $\phi = \theta - \Theta \neq 0$. If we look then at how the phase difference changes with time we see that $\frac{d\phi}{dt} = (\omega - \Omega) + \epsilon P(\theta)$ and for our special case of $\Omega = \omega$ we see that ϕ grows to 2π (or shrinks to 0 with negative ϵ) as $\frac{d\phi}{dt} = \epsilon P(\theta)$. By our setting up of the problem we've said that $P(0) = P(2\pi) = 0$ and thus once $\phi = 0$ the system becomes phase locked. Thus applying an external manual entrainment of frequency $\Omega = \omega$ and amplitude ϵ will entrain the system to a phase of $\theta = \Theta$. An entrainment frequency of $\Omega \neq \omega$ may or may not entrain the system dependent on the relative magnitudes of $|\omega - \Omega|$ and $|\epsilon|$. The further the driving frequency is from the native frequency the stronger the entrainment has to be. See Figure 2.4d.

Consider now two nearly identical oscillators with frequencies ω_1, ω_2 and phases θ_1, θ_2 that are coupled such that some portion ϵ of the outflow of each flush goes into the tank of the other oscillator. The phase difference then would be $\phi = \theta_1 - \theta_2$ and would change with time as $\frac{d\phi}{dt} = \frac{d\theta_1}{dt} - \frac{d\theta_2}{dt} = (\omega_1 - \omega_2) + \epsilon(P(\theta_1) - P(\theta_2))$. The system then will become phase locked when $\frac{d\phi}{dt} = (\omega_1 - \omega_2) + \epsilon(P(\theta_1) - P(\theta_2)) = 0$. However at this point the problem becomes quite intractable without some more information about $P(\theta)$.

2.2.3 The Kuramoto Model

A common mechanism-free phase oscillator model is the Kuramoto Model (Equation 2.1). The Kuramoto model is very powerful in its ability to predict the synchronization of os-

cillators with excitatory coupling (such as fireflies) and some of the attractor patterns of oscillators with inhibitory coupling (such as the $2\pi/3$ state of BZ emulsions) but is fundamentally unable to predict amplitude fluctuations (such as the s0π state of BZ emulsions, see Section 4.5.5 for more on the s0π state).

$$\frac{\partial\theta_i}{\partial t} = \omega_i + \frac{K}{N}\sum_{j=1}^{N}\sin(\theta_j - \theta_i), i = 1...N \tag{2.1}$$

The Kuramoto model assumes a specific form for the phase response curve as $P(\theta_i) = \sin(\theta_j - \theta_i)$ which is the leading term for any Fourier expansion of a periodic odd function.

Applying the Kuramoto model to our example above would predict phase locking when

$$\frac{d\phi}{dt} = (\omega_1 - \omega_2) + \frac{\epsilon}{2}(\sin(\theta_2 - \theta_1) - \sin(\theta_1 - \theta_2)) = (\omega_1 - \omega_2) + \epsilon\sin(\theta_2 - \theta_1) = 0$$

which for a frequency difference (dispersion) of $\Delta\omega = \omega_1 - \omega_2$ would have a phase difference $\phi = \theta_1 - \theta_2$ of $\Delta\omega = -\epsilon\sin(\phi)$ and when $\Delta\omega = 0$ the system will have a phase difference of $\phi = 0$ or π. Thus the Kuramoto model predicts that with our two coupled oscillators they can synchronize either in phase or out of phase.

From here it is easy to consider adding a third oscillator so that each oscillator is connected to both of the others. This configuration mimics that of the upright triangle basis for hexagonally close-packed spheres. The phase differences then ϕ_{12}, ϕ_{23}, ϕ_{31} would be described as $\phi_{ij} = \theta_i - \theta_j$ where each individual phase would evolve as

$$\frac{d\theta_i}{dt} = \omega_i + \frac{\epsilon}{3}\left(\sin(\theta_j - \theta_i) + \sin(\theta_k - \theta_i)\right)$$

such that the phase differences evolve as

$$\frac{d\phi_{ij}}{dt} = (\omega_i - \omega_j) + \frac{\epsilon}{3}\left(\sin(\theta_j - \theta_i) + \sin(\theta_k - \theta_i) - \sin(\theta_k - \theta_j) - \sin(\theta_i - \theta_j)\right)$$

which can be simplified to $\frac{d\phi_{ij}}{dt} = (\Delta\omega_{ij}) + \frac{\epsilon}{3}\left(\sin(\phi_{ki}) + \sin(\phi_{jk}) - 2\sin(\phi_{ij})\right)$. Thus one solution of the Kuramoto model is that phase locking would occur for $\Delta\omega = 0$ at $\phi_{ij} = \phi_{jk} = \phi_{ki} = 2\pi/3$.

2.2.4 Manual Entrainment of Coupled Oscillators

We can now consider a more general situation of an oscillator that is both coupled to other oscillators and subjected to external perturbation. There is no particular reason to assume that the coupling and external perturbation will have the same strength or phase response curve so the general situation for the evolution of the phase for such an oscillator would be described as

$$\frac{d\theta_i}{dt} = \omega_i + \frac{K}{N}\sum_{j=1}^{N} F(\theta_j - \theta_i) + \epsilon P(\theta_i)$$

where F is the phase response curve due to the coupling, P is the phase response curve due to the external perturbation, K and ϵ are the corresponding coupling strengths, and N is the number of coupled oscillators. If we consider now just two of these oscillators and look at their phase difference ϕ we see that

$$\frac{d\phi_{12}}{dt} = \Delta\omega + \frac{K}{2}F(-\phi_{12}) + \epsilon P(\theta_1)$$

which if we assume the form of F from the Kuramoto model and $P = \cos(2\theta)$ we see phase locking at $\frac{K}{2}\sin(\phi_{12}) = \epsilon\cos(2\theta_1)$ at which point the requisite entrainment phase $\Theta = \theta_1$ can be solved for from the desired phase difference ϕ_{12}. Expanding this to 2D square or hexagonal

lattices adds complication to the computation but adds nothing new to the mathematical theory.

An approach to experimental manual entrainment of coupled oscillators would start with measuring the phase response curves F, P and coupling strengths K, ϵ for some experimental system where $\Delta\omega \approx 0$. With this information the desired phase difference would be

$$\phi_{ij} = \int_0^\tau \left(\frac{K}{N} \sum_{i \neq j}^{N} F(\theta_j - \theta_i) + \epsilon P(\theta_i) \right) dt$$

which is numerically calculable for the τ and ϵ to be applied.

2.2.5 Amplitude Perturbations and BZ

In the previous few sections we've discussed perturbations to the phase of the oscillator. Such perturbations are applicable in situations such as the toilet analogy but in many other situations both the phase and amplitude are perturbable. In most cases a phase perturbation and amplitude perturbation are very closely related. For example a simple oscillating spring's phase is defined by its current displacement much as its amplitude is defined by its maximum displacement. The biggest difference between a phase perturbation and an amplitude perturbation comes from where the perturbation leaves the system in phase space. A phase perturbation moves the system to a different point on the limit cycle while an amplitude perturbation moves the state to a different point in phase space. In general this new location in phase space (y_0) will not be on the limit cycle and the system will have to relax back onto the attractor (passing through some point on the limit cycle x_0). All paths that pass through x_0 at the same time are called *isochrons*. Thus an amplitude perturbation to a point y_0 is similar to a phase perturbation to the point x_0 after a relaxation period. See Figure 2.5 for more information.

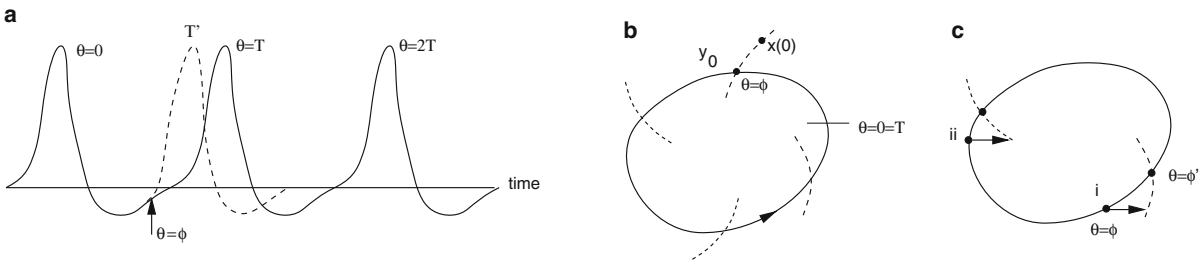

Figure 2.5: Illustrations of the isochrons for an oscillator. Image (a) shows the time series for the oscillator. Image (b) shows the limit cycle for the oscillator with isochrons (dashed lines). A system in phase space off the limit cycle along an isochron will relax onto the limit cycle with the same phase as a system at any point along the isochron. Image (c) demonstrates amplitude perturbations along a single dimension and the phase change they will elicit. A perturbation given at point i will have a positive phase change while the same perturbation at point ii will have a negative phase change. Image adapted from [23].

In BZ the state of a single oscillator is described by the concentrations of each constituent chemical at a given point in time and not by a simple phase variable. In vector notation the current state of the system is usually given as $\mathbf{X}$ where the concentration of a particular species then would be X_j. For multiple coupled oscillators each oscillator would be described by $\mathbf{X}_i$ with each particular species as X_{ij}. As in BZ arbitrary amplitude perturbations may not be allowed and only a single species X_p may be perturbable. Thus in phase space perturbation vectors may exist along only a single dimension. If we consider the case that amplitude perturbations are only allowed along X_p then the evolution of the system could be described as

$$\frac{d\mathbf{X}}{dt} = \boldsymbol{\omega}(\mathbf{X}) + \epsilon X_p \mathbf{P}(\mathbf{X})$$

where $\boldsymbol{\omega}(\mathbf{X})$ is a vector function describing the chemistry of the system and $\mathbf{P}(\mathbf{X})$ is the vector phase response curve for that particular perturbation. If there are multiple attractors within the phase space it is entirely possible that the new state $\mathbf{X}'$ may relax to the other attractor. Thus amplitude perturbations can cause the system to move from one attractor

basin to another while phase perturbations could never do that. In the case of coupled oscillators the system would be described by

$$\frac{d\mathbf{X}_i}{dt} = \boldsymbol{\omega}(\mathbf{X}_i) + \frac{K}{N}\sum_{i\neq j}^{N}\mathbf{F}(\mathbf{X}_j, \mathbf{X}_i) + \epsilon X_{ip}\mathbf{P}(\mathbf{X}_i)$$

where $\mathbf{F}(\mathbf{X}_j, \mathbf{X}_i)$ is some vector function describing the vector phase response curve due to coupling. In the language of linear algebra this could be described as a matrix equation where $\boldsymbol{\omega}$, $\mathbf{F}$, and $\mathbf{P}$ are matrix operators acting on the vector $\mathbf{X}$. A simplified version of the above then could read $\dot{\mathbf{X}} = \boldsymbol{\omega}\mathbf{X} + \mathbf{F}\mathbf{X} + \epsilon\mathbf{P}\mathbf{X}$ which when intergrated over some time period τ would yield $\mathbf{X}_f = \int^{\tau}(\boldsymbol{\omega}\mathbf{X}_i + \mathbf{F}\mathbf{X}_i + \epsilon\mathbf{P}\mathbf{X}_i)\,dt$ thus for any desired state $\mathbf{X}_f$ with measurements of $\boldsymbol{\omega}$, $\mathbf{F}$, $\mathbf{P}$, and $\mathbf{X}_i$ the system would be calculable for the τ and ϵ required to make the desired perturbation. A brief caveat is that this perturbation is not guaranteed to be possible.

2.3 Experimental Background

The use of BZ as an experimental system to study coupled oscillators started in 1975 with the study of synchronization in two coupled BZ tank reactors [65]. This was followed by observations of chaos in BZ tank reactors [99] and the appropriate mathematical analysis [101, 95]. In 1983 the photo-inhibition of BZ was studied [31] which would become a cornerstone for work in BZ [121]. The study of how coupled BZ tank reactors respond to perturbations followed in 1988 [16]. In 1989 the catalyst was identified as the dominant control species with mass transfer coupling and both in and out of phase attractors were observed [11]. (See [11] also for a review of coupled tank reactor experiments of the time.) This work was followed by a study of diffusion-induced instabilities in coupled BZ reactors [57]. Frequency

locking of light activated BZ was observed in 1997 [90] and patterns of photosensitive BZ were simulated in 2000 [140]. Also in 2000 phase portrait analysis techniques were applied to experimental gels of photosensitive BZ [60]. The use of BZ for studies of synchronization began to come to the front with the introduction of the BZ water-in-oil microemulsion (BZ-AOT system) [126, 127]. Then in 2002 the Kuramoto model was verified for the nickel electrode sulfuric acid system [47]. Later experiments described "twinkling eye" hexagonal phase patterns in BZ [141], the entrainment of BZ gels by periodic illumination [61], theoretical work on coupling via one diffusive species [128], and on the periodic driving of coupled BZ oscillators [130]. Our work itself builds from a 2008 study [117] where a microfluidic assembly was used to study diffusively coupled chemical oscillators and identified Br_2 as the dominant control species for diffusively coupled reactors.

2.3.1 Other Experimental Systems

Oscillatory experimental systems fall into two broad categories: continuous and discrete oscillators. Continuous systems include cardiac tissue, the classic petri dish, continuous-flow stirred-tank reactors (CSTRs), and the AOT system. Discrete systems include fireflies, coupled CSTRs, nickel electrodes, stable emulsions, and catalyst beads in catalyst free solution. Each system has different coupling mechanisms for different types of coupling. For example the continuous systems tend to have mass transfer coupling with the AOT system introducing a separation of time scales between the diffusion rates of the activator and inhibitor. The discrete systems can have mass transfer, electrical, or even optical coupling.

Other experimental systems similar to the BZ emulsion consider coupled BZ reactors where the catalyst is bound to beads or polymer posts in a solution containing the rest of the reactants. These experiments have been done with fixed 1D arrays [29], fixed 2D square

arrays [85], and with the beads free to move in the solution [112, 115]. These are all open systems that can oscillate indefinitely as long as the supply of fresh reagents continues. The fixed array systems consider nearest neighbor coupling with both inhibitory and excitatory coupling. The beads in solution systems considers all to all coupling with both inhibitory and excitatory coupling. For comparison the emulsion system considers nearest neighbor coupling with primarily inhibitory coupling and a hypothetical stirred dish of emulsion would consider all to all coupling with primarily inhibitory coupling.

2.3.2 Other Applications

The BZ system can be used for a number of applications including neuroscience as inhibitory coupling of oscillators is integral to the study of neural networks [103]. The earliest application was to use BZ for photo processing [51]. Later examples are to use coupled BZ tank reactors to study the "binding problem" in neuroscience [12] and using BZ to study the theory of spiral waves [27] and probe for the existence of chimera states [1]. More recent examples are to use microfluidic BZ drops as logical devices [20], to use BZ to study aspects of cell biology [43], to use BZ as the driving force of polymer gels [8], and to study the locomotion of different cellular organisms [113].

2.4 Instrumentation and Materials

Our particular experimental method draws from the chemistry experiments involving BZ mentioned above as well as flow focusing microfluidics and the programmable illumination microscope [119]. Flow focusing microfluidics is the use of microdevices to create streams of fluids and emulsions on the nanoliter scale. Our technique is similar to that described by [4] except with two aqueous phase inlets to mix the BZ reactants on chip. See Figure 2.6

for more details. A key consideration for BZ emulsions is the choice of oil and surfactant to use. Hydrocarbon oils are less than ideal for use in PDMS as they cause swelling [56] so we use a fluorocarbon oil (HFE 7500) which does not have that problem [15]. The surfactant then must stabilize the emulsion while being compatible with fluorocarbon oils and not reacting or otherwise interfering with Br_2 diffusion. Such a surfactant (REA) was created by [35]. A Programmable Illumination Microscope (PIM) is a microscope with two different illumination sources, one general and the other programmable. The PIM is described in much more detail in Chapter 3. The first light source is a typical Köhler Illumination for viewing of the sample. Our PIMs use green LEDs for observation due to the advantages with ferroin/ferriin outlined earlier. The second light source is a modified commercial projector augmented so as to focus on the sample through the microscope objective. This illumination source allows for very specific exposure of different parts of the field of view to different colors and intensities of light. The PIM can also be constructed from a DLP mirror based projector to make use of the increased contrast ratio and depth of black compared to a PIM constructed using a LCD projector. See Figure 2.7 for more details. The PIMs we made are based on the maskless photolithography device of [41, 40] following the principles of [75]. The PIM is also capable of making three-dimensional microdevices [63].

2.5 Preliminary Experiments

Preliminary experiments using the same BZ emulsion system described here have studied in detail the attractor patterns of 1D arrangements of BZ emulsions [13] (Figure 2.8) and the native attractor states of 2D close packed spheres [116] (Figure 2.9). For 1D systems it is found that the system has two attractor states, an unstable completely synchronized state and a stable nearest neighbor out of phase state. Small systems with specific boundary

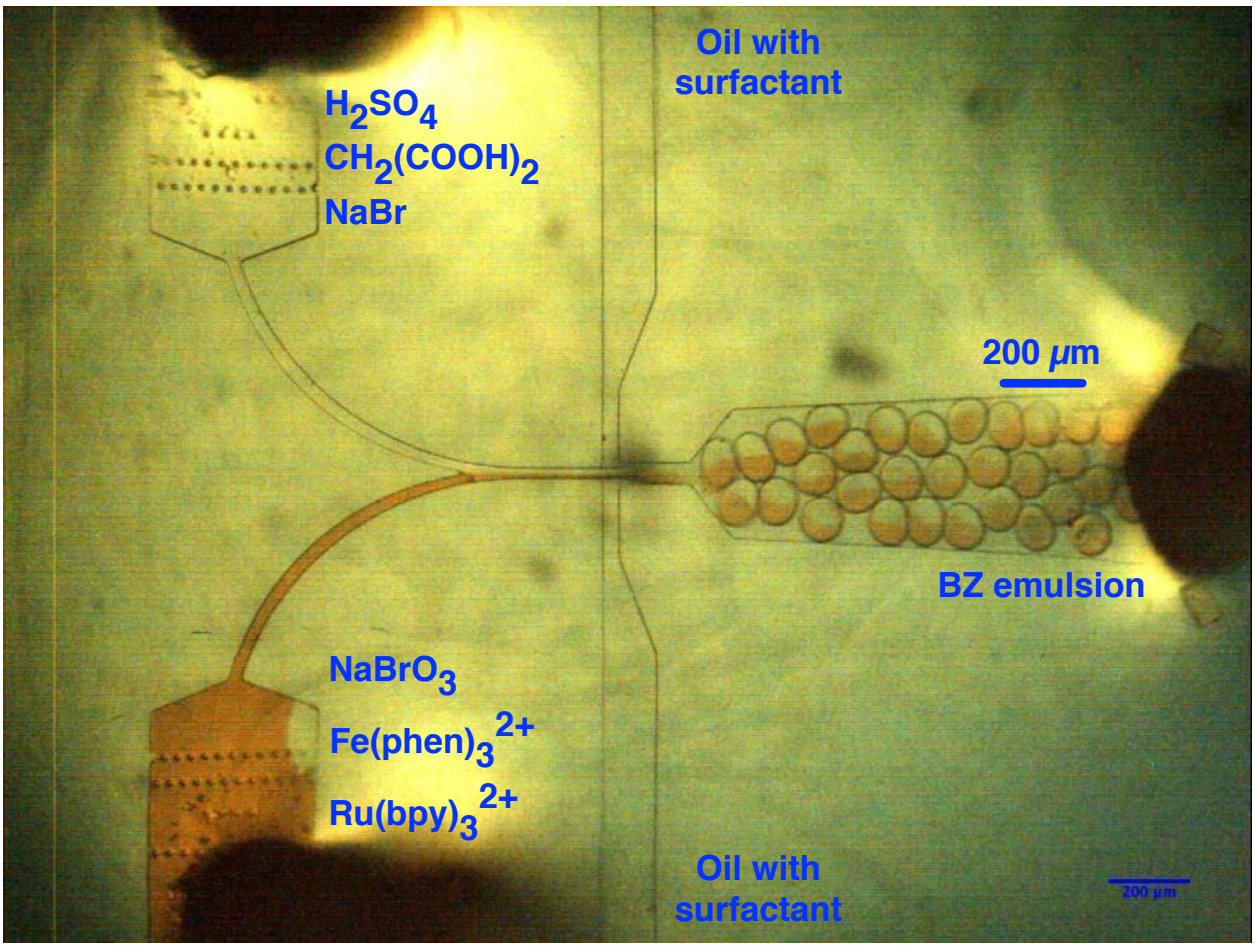

Figure 2.6: An example of the emulsion chip used to create BZ emulsions. There are many variants of the chip design but the above demonstrates all of the key features. The key features are the aqueous phase inputs for the BZ reactants, the oil phase inputs for the emulsion oil, the drop making nozzle (not labelled), and the collection arm for BZ droplets. From left above on this particular device are the aqueous inputs (on this particular device there are two in order to mix the BZ reactants at the latest time possible to delay the start of the reaction), the oil inputs (most devices will have two in order to "pinch" off droplets but some older devices have only one), the nozzle where the aqueous and oil phases meet (the dimensions of the nozzle play a large part in the selection of drop size), and finally the collection arm for created BZ droplets. This collection arm can be tapped in a variety of ways for creating 1D or 2D arrays of droplets.

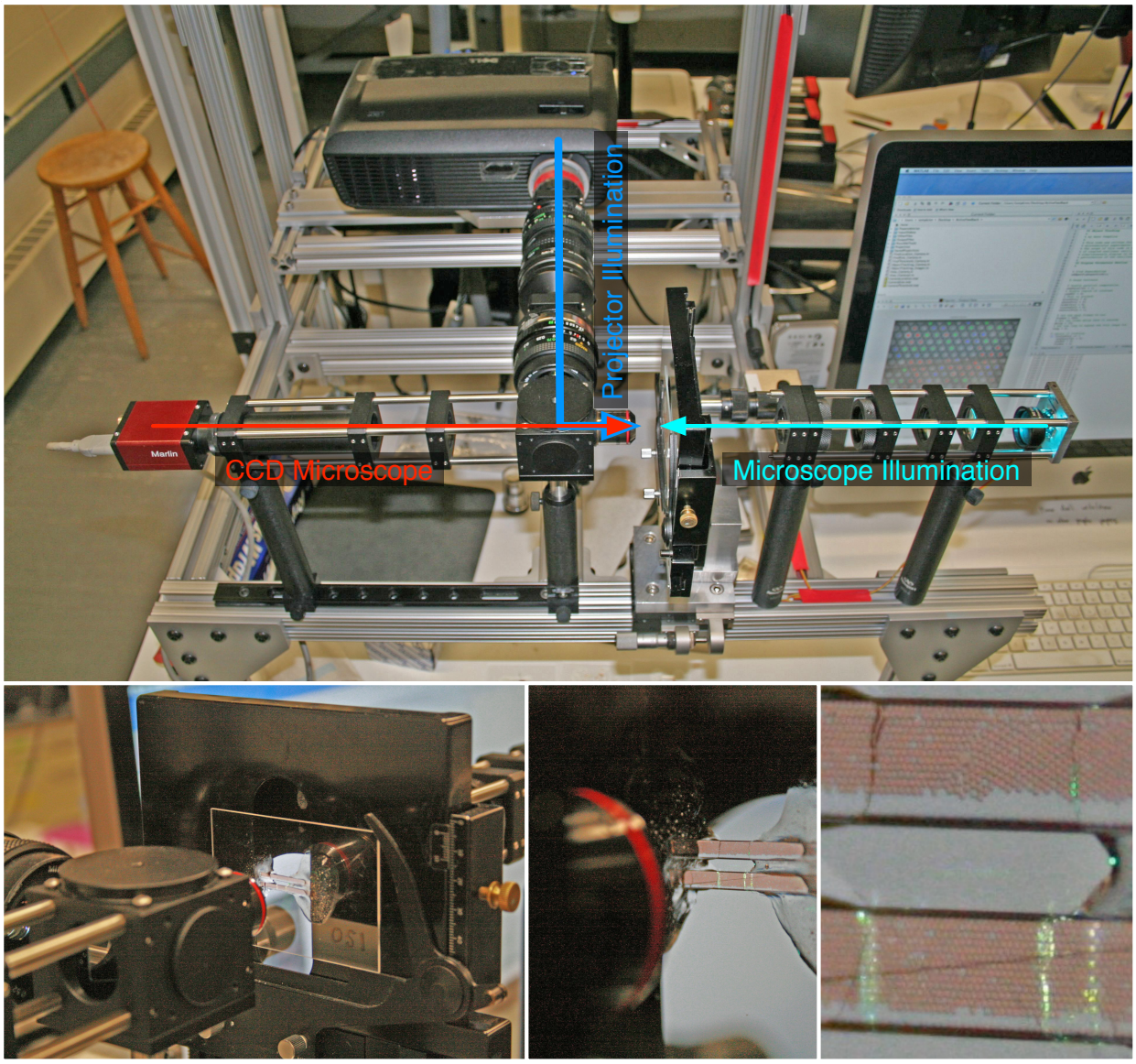

Figure 2.7: A montage of the PIM and sample. Shown are labelled light paths for the DLP based PIM and closeup images of the sample stage, a sample being imaged, and the sample itself. Individual drops within the BZ emulsion are visible in the lower right image. The only significant difference between a DLP based PIM and a LCD based PIM is the contrast ratio of the projected illumination. The design, construction, and specifications of the PIM are described in much more detail in Chapter 3.

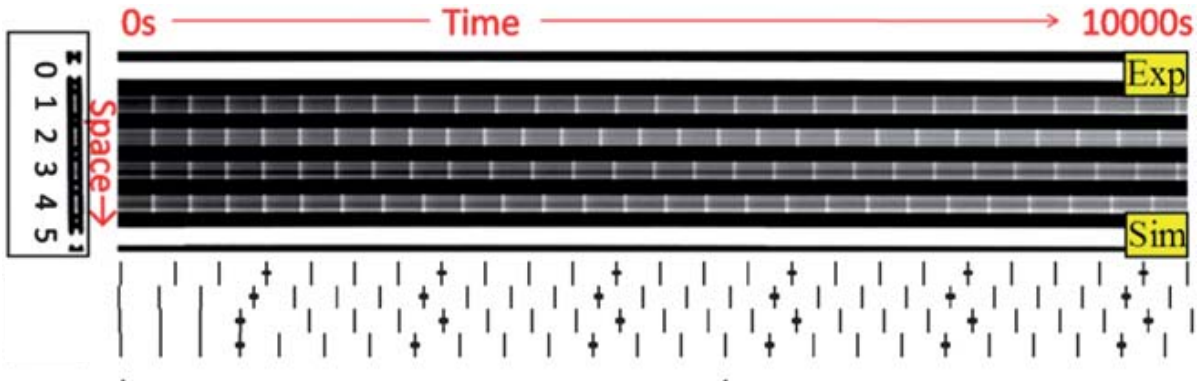

Figure 2.8: A typical 1D experiment and corresponding simulation. Initially all of the drops are synchronized to flash simultaneously and over the course of a few oscillations slight imperfections cause the system to deviate from this unstable fixed point and eventually settle into the out of phase stable fixed point. The drops on the ends labelled "0" and "5" are held off continuously to isolate the central four drops. The simulation below reproduces the observed phenomena. Image adapted from [13].

conditions have been found to have other more sophisticated patterns. Larger 2D systems have been found to have three attractor states based on drop size or coupling strength. For low coupling the drops all oscillate out of phase with their nearest neighbors similar to the stable state for 1D except with a $2\pi/3$ phase difference. For middling coupling the system silences one-third of the drops and adopts a nearest neighbor out of phase pattern very similar to the stable state for 1D named the "s0π" state. At large coupling the system ceases oscillations entirely and assumes a Turing like pattern of "on" and "off" drops. A completely synchronized state in 2D has not been observed beyond temporary transient states. See Figure 2.10 for time series data demonstrating these attractor states.

Other preliminary experiments involved the study, perturbation, and control of attractor patterns of 2D sheets of a hexagonally close-packed BZ emulsion. Data from these experiments is inconclusive as to what effect the photo entrainment has on the system (Figure 2.11). Here the photo entrainment mimicked that of the desired pattern, pulses of light were

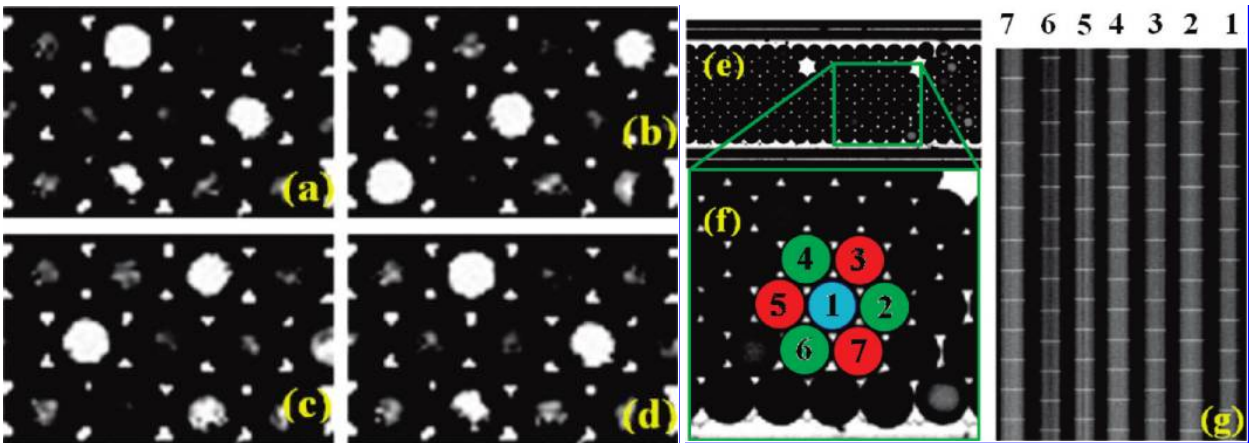

Figure 2.9: The typical attractor state for a 2D array of BZ drops. Every drop oscillates $2\pi/3$ out of phase with respect to their neighbors. This attractor pattern comes in both right and let handed variants based on the chirality assumed by each region of drops. Panels (a-d) show the same region at T/3 intervals. Panels (e-g) show a space-time plot of a similar region. Image adapted from [116].

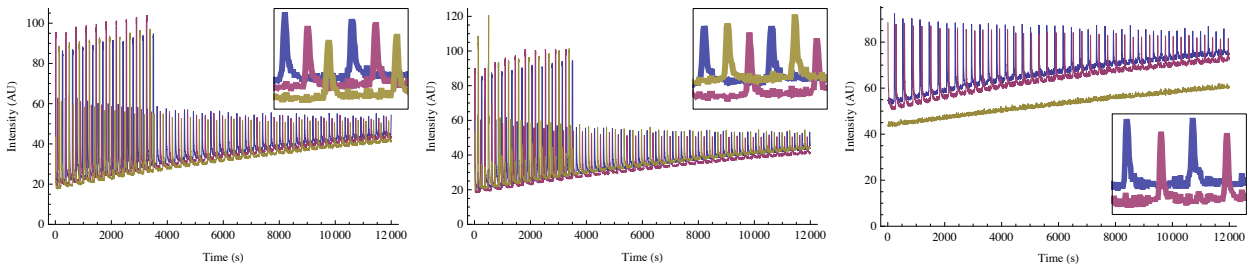

Figure 2.10: Time series data from three different triangles of drops demonstrating the $2\pi/3$ and s0π attractor patterns. The image on the left is initially perturbed and then oscillates in a right handed $2\pi/3$ state. The image in the middle is initially perturbed and then oscillates in a left handed $2\pi/3$ state. The image on the right is unperturbed and settles in the s0π state.

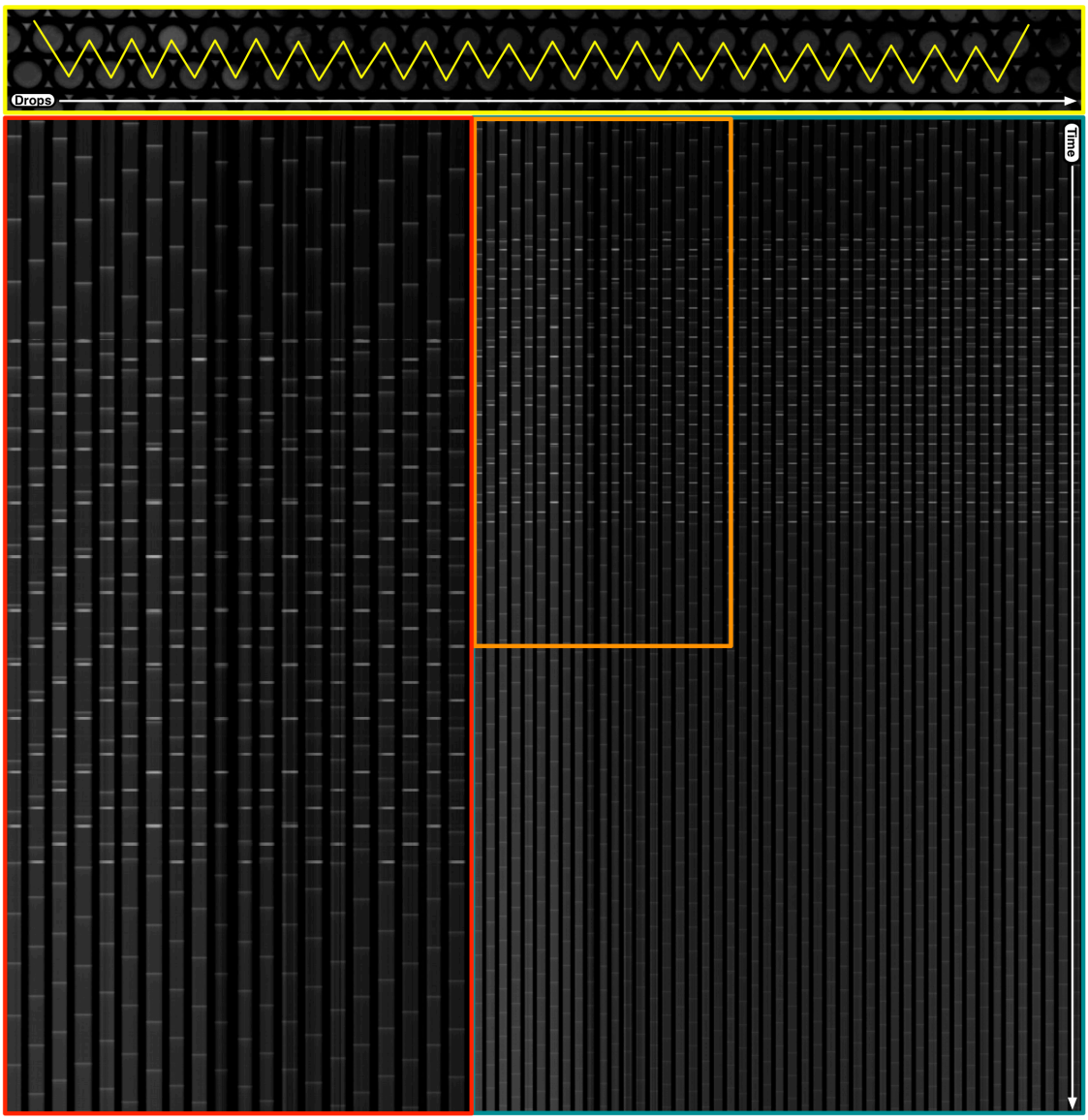

Figure 2.11: Space-time plots demonstrating the $2\pi/3$ state and photo-entrainment. The images on the bottom are space-time plots from the original sequence of images along a jagged line as shown in the top image. This jagged line is used so that every three drops in the spacetime plot are actual triangles of neighbors. The image on the left is a magnified portion of the image on the right. In the spacetime images the brighter pulses are the photo-entrainment while the dimmer pulses are the oxidation spikes. The oscillations post entrainment are very neatly aligned along diagonal lines relating to $2\pi/3$ phase differences while the oscillations prior to entrainment are far more jagged.

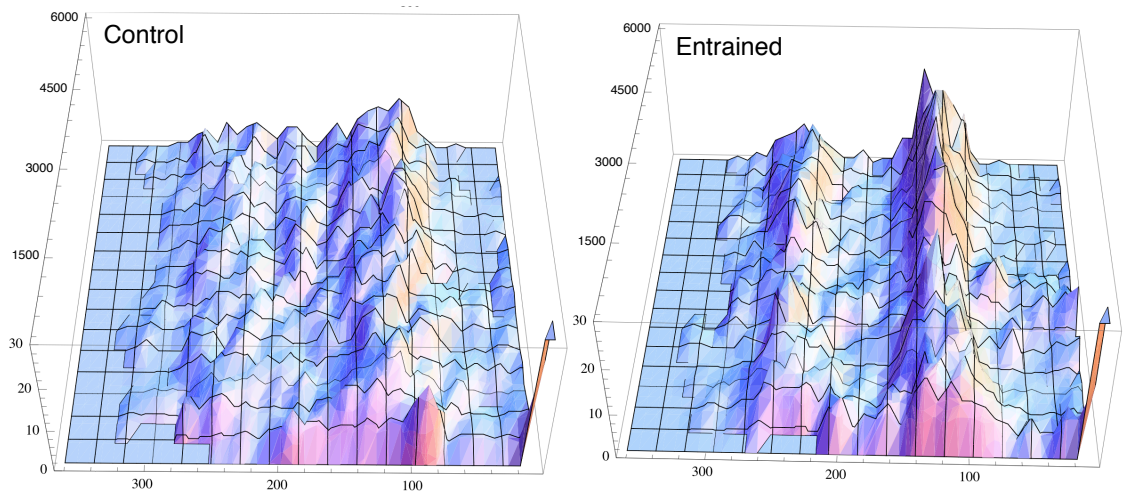

Figure 2.12: The phase differences for nearest neighbors in a 2D capillary with and without photo-entrainment. In the plots above the axis from 0-360 displays the phase difference between nearest neighbors (in units of degrees) while the other two axes are time (in units of seconds) and a histogram of the number of pairs at that phase difference. The plots above show a different phase difference profile for the control versus entrained data sets and that the phase differences are quite stable.

applied to drops at the timing and duration of the desired oxidation spikes. To quantify the effectiveness of the entrainment the nearest neighbor phase differences were measured across the sample. The nearest neighbor phase difference is a pairwise histogram of every nearest neighbor drop pairing with the absolute value of their phase differences. Thus plots of the phase differences are indicative of the underlying attractor pattern. A sharp peak at 180 or a pair of peaks at 120 and 240 are indicative of an underlying s0π or $2\pi/3$ attractor. A flat or muddled histogram is indicative of a mixed or disordered state. Observations of the phase differences between nearest neighbor oscillators (Figure 2.12) indicates that the entrained systems have a much sharper $2\pi/3$ phase difference.

Chapter 3

Design and Construction of the Programmable Illumination Microscope

This chapter is adapted from [119] which is under review for publication at the *The American Journal of Physics*.

Abstract

Targeted and patterned illumination systems are becoming an important tool for experimentalists in numerous fields including neuroscience, genetics, biophysics, microfabrication, and dynamical systems due to their ability to selectively illuminate and perturb a small specified region of interest within a sample. Perhaps the most well known usages of targeted illumination are in the fields of optogenetics, where a single specimen is kept in the center of the field of view using a movable stage and illumination is selectively applied to

control neural behaviors, and in maskless photolithography, where patterned illumination is used to cure patterns into photoresist materials without the need of a photomask. We have developed a programmable illumination system capable of tracking and illuminating numerous objects simultaneously using only low-cost and reused optical components. The active feedback control software allows for a closed loop system that tracks and perturbs objects of interest automatically. Our system uses a static stage where the objects of interests are tracked computationally as they move across the field of view allowing for a large number of simultaneous experiments. An algorithmically determined illumination pattern can be applied to anywhere in the field of view with simultaneous imaging and perturbation using different colors of light to enable spatially and temporally structured illumination. Our system consists of a consumer projector, camera, 35mm camera lens, and minimal other optical/scaffolding components. The entire apparatus can be assembled for under $4000. Supplemental Matlab code is included with [119] to assist in the setup of the active feedback software.

3.1 Introduction

Targeted, customizable, and programmable illumination techniques are an emerging tool in experimental disciplines. Targeted illumination has been used in the field of optogenetics for the tracking and manipulation of organisms such as *C. elegans* [105] while customizable illumination has been used in semiconductor manufacturing as a maskless photolithography technique [102] and programmable illumination has been used in the study of coupled chemical oscillators [124].

All of these targeted illumination techniques make use of the ability to illuminate the field of view customisably and controllably in different regions. The Programmable Illumination

Microscope (PIM), however, is more customizable and diverse in its potential applications due to its modular design, inexpensive components, and active feedback control software. Further, the principles behind its design are readily accessible to undergraduate students allowing for the construction of a PIM to be an undergraduate student project. Similar systems have been constructed and used previously at primarily undergraduate institutions [75] however these setups require the repurposing of an existing trinocular microscope and are limited to ultralight projectors that can be mounted directly on the camera port. The system described here is more versatile in functionality due to its open modular design, can accommodate higher quality projectors with more powerful illumination, and provides an engaging educational opportunity for a project in optics. In addition to the hardware advantages the system described here isn't limited to passive illumination as the adaptive feedback software allows for programmable illumination that can respond to the objects being imaged based on a predefined response algorithm.

Optical scanning systems using galvanometers or acousto-optic deflectors (AOD) are commonly used in various laser microscopy techniques and in entertaining laser light shows. In theory a system similar to ours could be constructed using either of these methods and achieve comparable results; however, these scanning systems illuminate point-by-point so that the illumination is time-shared over the field of view while a projector illuminates the entire field of view simultaneously. For our system we chose to use a standard consumer projector due to both price considerations and ease of use. Used consumer projectors are readily available inexpensively and require little technical knowledge to use or implement whereas galvanometer or AOD based systems are only inexpensive as salvaged or "kit" pieces that require significant time and expertise to assemble. Consumer projectors have a standardized software interface which makes software development significantly easier. For the purposes of an efficient and inexpensive laboratory tool a consumer projector is a robust

and approachable option.

The following sections detail the hardware and software used in our system to aid in the creation of similar microscopes. In all cases the hardware is inexpensive and the software accessible. Nothing cost prohibitive or overly sophisticated is used in creating the microscope detailed here. No specialized training or tools are required. A critical step in the construction of the PIM is aligning the field of projection with the field of view. Once the alignment has been complete the software can illuminate any object within the field of view automatically allowing for a closed loop experimental design. See Appendix A and Figure A.1 for more information on aligning the PIM.

3.2 Technical Details

The PIM described here can be considered the result of two separate projects, both of which are interesting and approachable endeavors accessible to advanced undergraduate students. First is the construction of the microscope itself from a minimally modified consumer projector, camera lens, assorted optical components, and scaffolding framework which together form a challenging and open-ended optics project. This project can range from a short assembly process to an involved study of advanced optics depending on the desired resolution and evenness of illumination of the final product. The second project is the writing of the control software that acquires data from the camera, sends output to the projector, and tracks the objects within the field of view. This project is also challenging and open-ended depending on the desired speed and functionality of the control software. All of the required functions are readily available in Matlab though a faster implementation could make use of a standalone programming language such as C or Python.

3.2.1 Hardware

Our system uses the light from a consumer projector for both illumination and perturbation of a chemical system. The exact projector used is not critical and we have created systems using both three-color liquid crystal display (LCD) and color-wheel digital light processing (DLP) projectors. A DLP projector typically has a higher contrast ratio than a comparable LCD projector (the DLP Dell 1210S has an advertised 2200:1 contrast ratio [14] while the LCD NEC VT800 has an advertised 500:1 contrast ratio [80] and the high-end LCD NEC NP1150 has an advertised 600:1 contrast ratio [79]) but a three-color projector provides continuous illumination while a single source projector uses a color-wheel that provides discontinuous illumination (the Dell 1210S has a 2X color wheel [14] that flashes each color at twice the refresh rate with a net duty cycle of just under 1/3). The DLP projector used (Dell 1210S) has off-axis optics due to the alignment of the mirror plane which requires further optical corrections and yields a less uniform image with poorer focal quality. LCD projectors are also often off-axis but the NEC VT800 and NEC NP1150 are on-axis. The primary consideration for choosing a projector is finding one where the lens is centered on the projector engine (LCD or DLP). One way to guarantee that the projector is on-axis is to select ones with geometric lens shift (as opposed to electronic lens shift). The PIM described here uses a NEC VT800 projector with a resolution of 1024×768 (purchased factory refurbished off of eBay). See Appendix B for a complete list of the components used and their prices at the time of purchasing.

For assembly into the apparatus we removed and reversed the focusing lens from the NEC VT800 projector in order to create a reduced image of the LCD outside of the projector. We note that depending on the projector it may be necessary to open the projector enclosure to remove the lens. Additionally, it is sometimes necessary to modify the projector enclosure

in order to position the reversed lens close enough to the LCD unit. Next, a camera lens (manual focus SLR lens from eBay) was used as a reduction lens to defocus the reduced image of the LCD to an infinity plane. The parallel light was then transmitted into the central beam cube and reflected off of a beamsplitter to an infinity corrected microscope objective attached to the beam cube which focuses the image onto the sample stage [13]. See Figure 3.1 for a schematic and photograph and Figure 3.2 for an exact layout of the optics. This setup allows the projector to illuminate the sample in reflection while a LED Köhler setup illuminates the sample in transmission. On the side of the beam cube opposite the sample stage a lens focuses the image onto the camera (Allied Vision Marlin F131-B with 1280×1024 resolution). In Figure 3.1 the computer input shown is an image of a 100μm semi-transparent "checkerboard" alignment grid and the computer output shown is illustrative of the software detecting and illuminating the white squares.

The full optical layout of the PIM with distances is shown in Figure 3.2. The optics path of the projected image is shown in pink from the source image within the projector to the focused image on the sample. Another projection image plane exists within the body of the reduction lens. The optics path for imaging the sample is shown in purple. The Köhler illumination optics path is shown in cyan with an intermediate image plane on the aperture diaphragm. An additional conjugate optics path for the Köhler field is shown in orange where the field diaphragm is imaged onto the sample. The field diaphragm controls the field of illumination and the aperture diaphragm controls the intensity of illumination. Also included are two neutral density filters to attenuate the intensity of the illumination from the projector and the LED. An additional 510 ± 10nm bandpass "green" filter is used to image the oxidation state of ferroin in chemical studies. The locations of the filters isn't critical as long as imaging planes are avoided. The camera is focused on a subset of the projected image to prevent regions of the field of view being inaccessible to the projected illumination. The

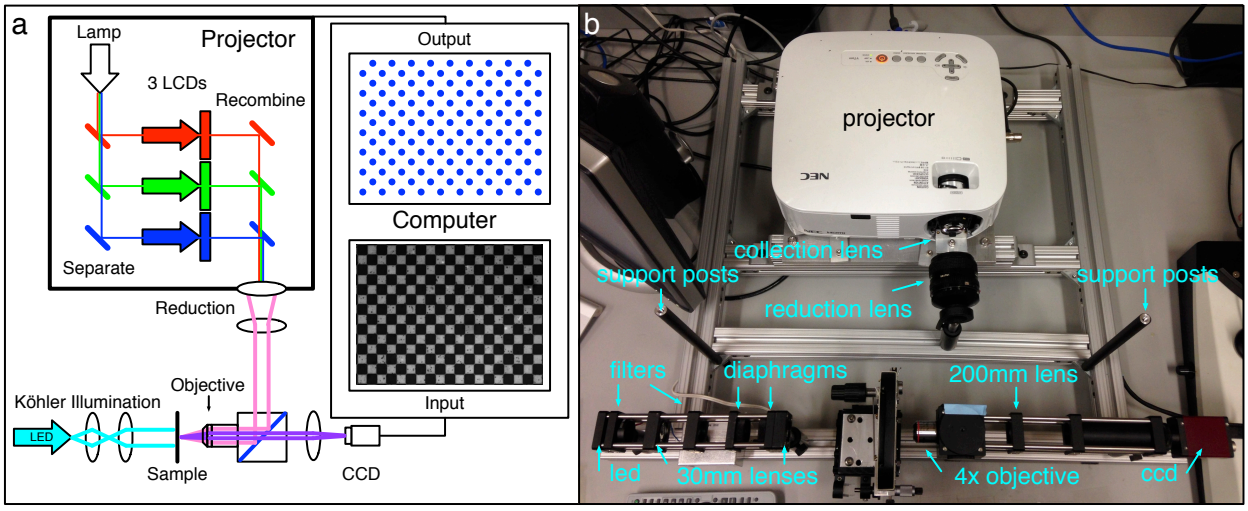

Figure 3.1: The optics of the Programmable Illumination Microscope. a) A schematic illustration. b) A photograph. Light from the projector exits the projector through the stock lens in reverse and is defocused to infinity using the lens from a 35mm camera. The parallel light is transmitted into the beam cube, reflected off of a beamsplitter, and focused through the 4x microscope objective to illuminate in reflection. The sample is imaged with a 200mm lens onto a CCD camera. An optional Köhler illumination setup is in place to illuminate the sample in transmission (a cyan LED in conjunction with a neutral density filter and 510nm bandpass filter focused using two 30mm lenses with ring-activated iris field and aperture diaphragms). Additionally a neutral density filter is taped to the beam cube to attenuate the intensity of light from the projector and support posts for the blackout cage are mounted to the supporting frame. The computer (not shown) calculates a dot for every white square in the 100μm checkerboard alignment grid. See Figure 3.2 for an exact layout of the optics. Image adapted from [119].

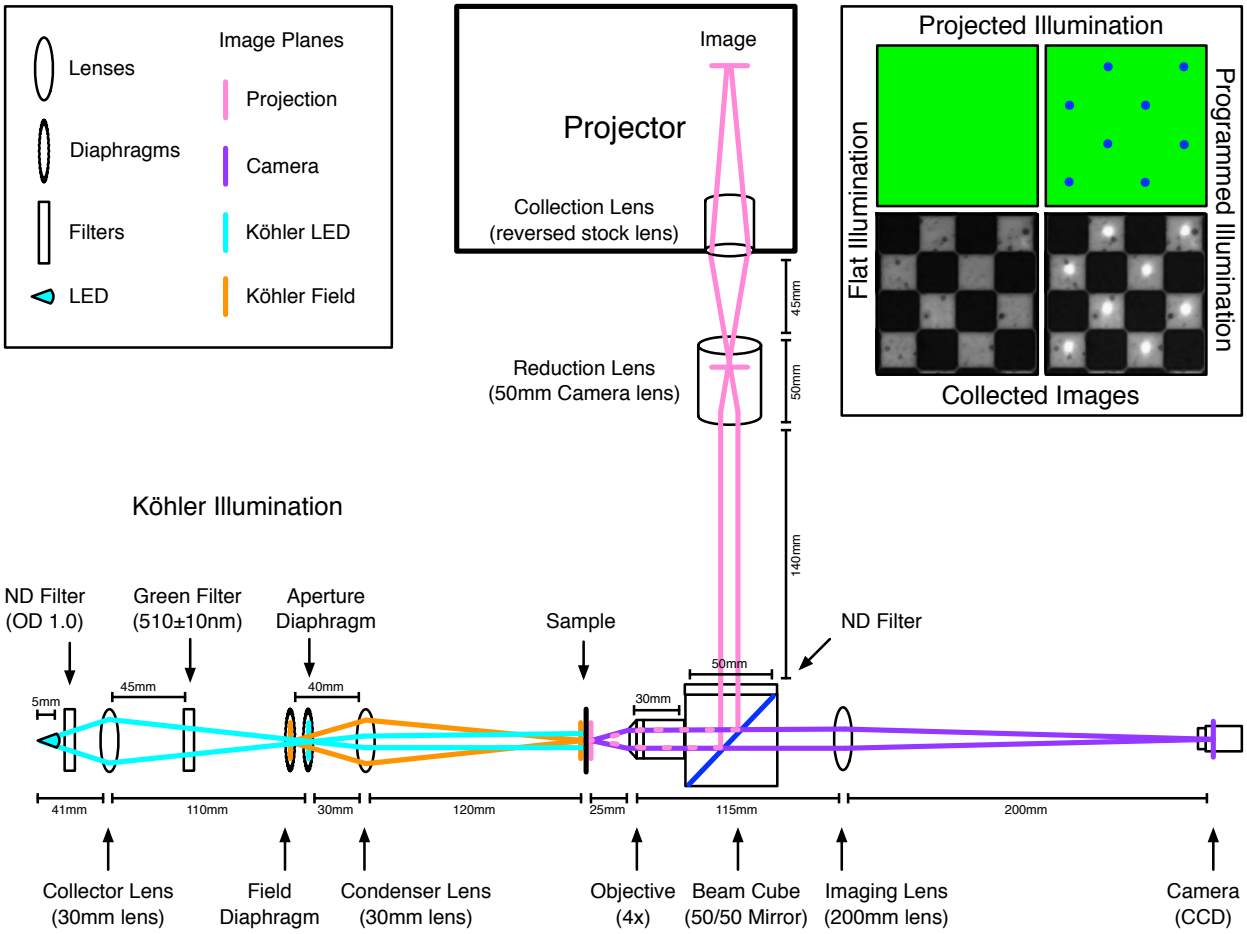

Figure 3.2: The optical layout of the PIM with distances between elements. The different optical paths are shown in pink, purple, and cyan with an additional conjugate path in orange. The original projection image from within the projector is focused onto the sample via the pink path with an intermediate image plane within the body of the reduction lens. The sample is imaged onto the camera via the purple path. The Köhler illumination is created via the cyan path with an intermediate image plane on the aperture diaphragm and the conjugate field path is shown in orange. The field diaphragm controls the field of illumination and the aperture diaphragm controls the intensity of illumination. The neutral density filters attenuate the intensity of the projector and LED while the 510±10nm bandpass "green" filter is used to select illumination wavelength. The locations of the filters aren't critical as long as imaging planes are avoided. Shown in the corner are examples of flat illumination and programmed illumination illuminating the 100μm checkerboard alignment grid. Image adapted from [119].

field of view can be further restricted within the field of projection to enhance uniformity of illumination by changing the focal length of the reduction lens. See Figure 3.3 for different overlaps of the field of projection and the field of view by varying the focal length of the reduction lens. Our system uses an overlap region of $\sim 564 \times 451$ pixels of the field of projection within the field of view. This overlap was chosen to balance the evenness of illumination while maintaining sufficient resolution for indexing individual elements within the field of view. When using the microscope a blackout cage is placed over the assembly to block ambient light. In Figure 3.1 the blackout cage has been removed but the support posts are exposed in the image. The microscope is further customizable by using the projector to illuminate in transmission or even using two projectors to have programmable illumination in both reflection and transmission. To reduce costs the Köhler illumination setup could be excluded and a lower resolution projector and camera could easily be used with minimal loss in functionality. It should be noted that the decision to reverse the stock lens is a compromise and not necessarily the best option for maintaining optical quality. It is very likely that the stock lens contains corrective optics and that reversing its direction could result in a greatly degraded image. This could be avoided by maintaining the projector in its factory condition and using a large collection lens to create the reduced intermediary image; however, such a large collection lens may be cost prohibitive. For several projectors we found that reversing the lens was a surprisingly good solution providing adequate image clarity while requiring minimal effort and zero additional cost.

The size of the projected image is customizable based on the magnification of microscope objective used. See Figure 3.4 for examples of the Brandeis seal projected through several different objectives. In each case the logo was projected onto a clean glass slide for imaging and onto a 100μm grid for measurement. The image is formed by projected light reflected backwards from the glass. As can be seen the image is recorded on the camera with high

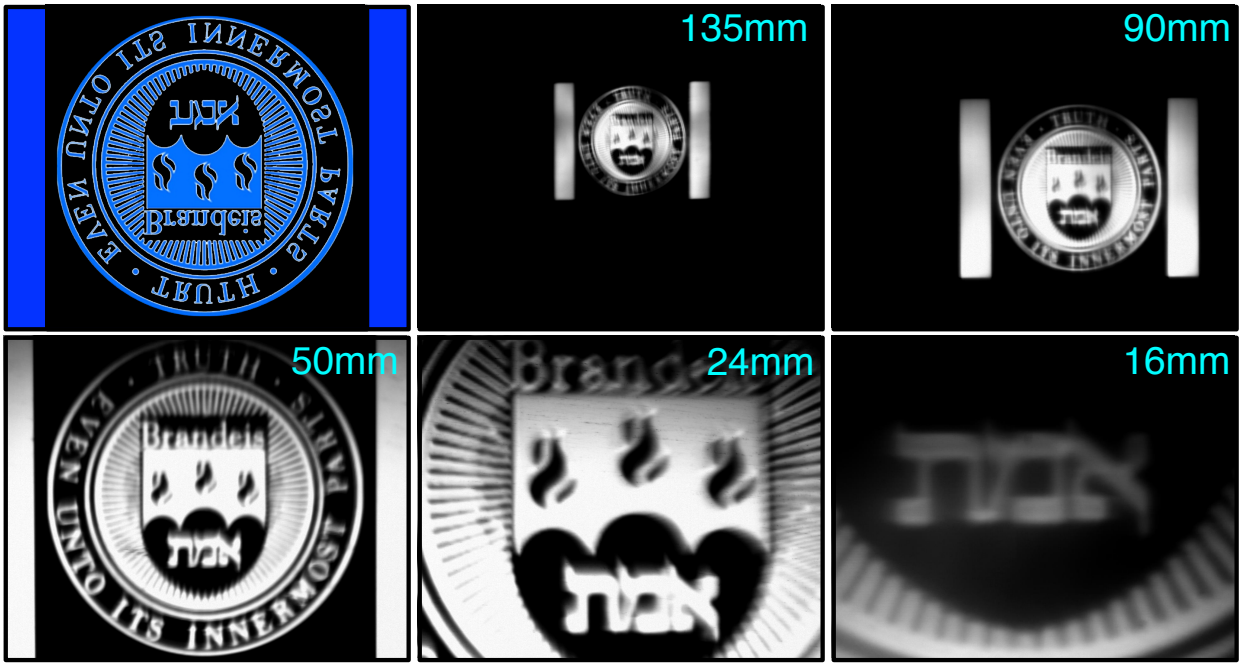

Figure 3.3: The overlap of the field of projection with the field of view of the PIM. The overlap is controllable by changing the focal length of the reduction lens (see Figure 3.1b) used in the PIM. Shown here are examples of the overlap using reduction lenses of different focal lengths. Note the exact overlap will also depend on the focusing lens used and the sensor size of the CCD. Top left: The image being projected onto a clean silicon wafer. Note that the Brandeis logo is upside down in the projection. Using a 135mm or 90mm lens results in the field of projection being smaller than the field of view. Using a 24mm or 16mm lens results in the field of view being smaller than the field of projection. Using a 50mm lens results in a nearly perfect overlap of the fields of view and projection. Image adapted from [119].

fidelity. The dot of the "i" in Brandeis is easily discernible even with a 40x objective. With a 20x objective (or lower) the "i" maintains a steep profile from the background level to the peak. The size and quality of the final image depends on the optics used and the care of their alignment.

The spectral output of the projector was unaltered from the manufacturer. The LED used for transmission illumination was a high intensity cyan LED filtered through a 510 ± 10nm filter. See Figure 3.5 for the illumination spectrum as measured on the sample stage. Finer selection of the spectra of each channel is possible by modifying the projector further with the addition of optical filters within each pathway.

The illumination from the projector is natively a Gaussian distribution with a peak in the center of the illumination. The distribution can be flattened via corrective optics or using software to adjust the spatial structure of the illumination. Although a physical optical correction is often preferable to use the optical techniques needed can be expensive and time intensive while a software correction can be less expensive and quicker to implement. Depending on the width of the distribution compared to the field of view the evenness of illumination may be acceptable uncorrected. Figure 3.6 shows the field of view before and after software flattening where the variation in intensity of the field of view was reduced from 8.6% to 1.1%. In this case the evenness of illumination is often acceptable uncorrected and is used as such for some experiments. The illumination was flattened using the formula $C_{light} = (f\,(1 - N_{image}) + n) \circ U_{light}$ where C_{light} is the corrected illumination, U_{light} is the uncorrected illumination, N_{image} is the normalized image in which the brightest pixel is set to 1 and taken with uncorrected illumination, f is a scaling factor to prevent overcorrecting the darker regions, n is an offset to scale the average intensity, and $\circ$ indicates the Hadamard product (an element by element multiplication of the matrices implemented as .* in Matlab). Other correction algorithms could be used as well.

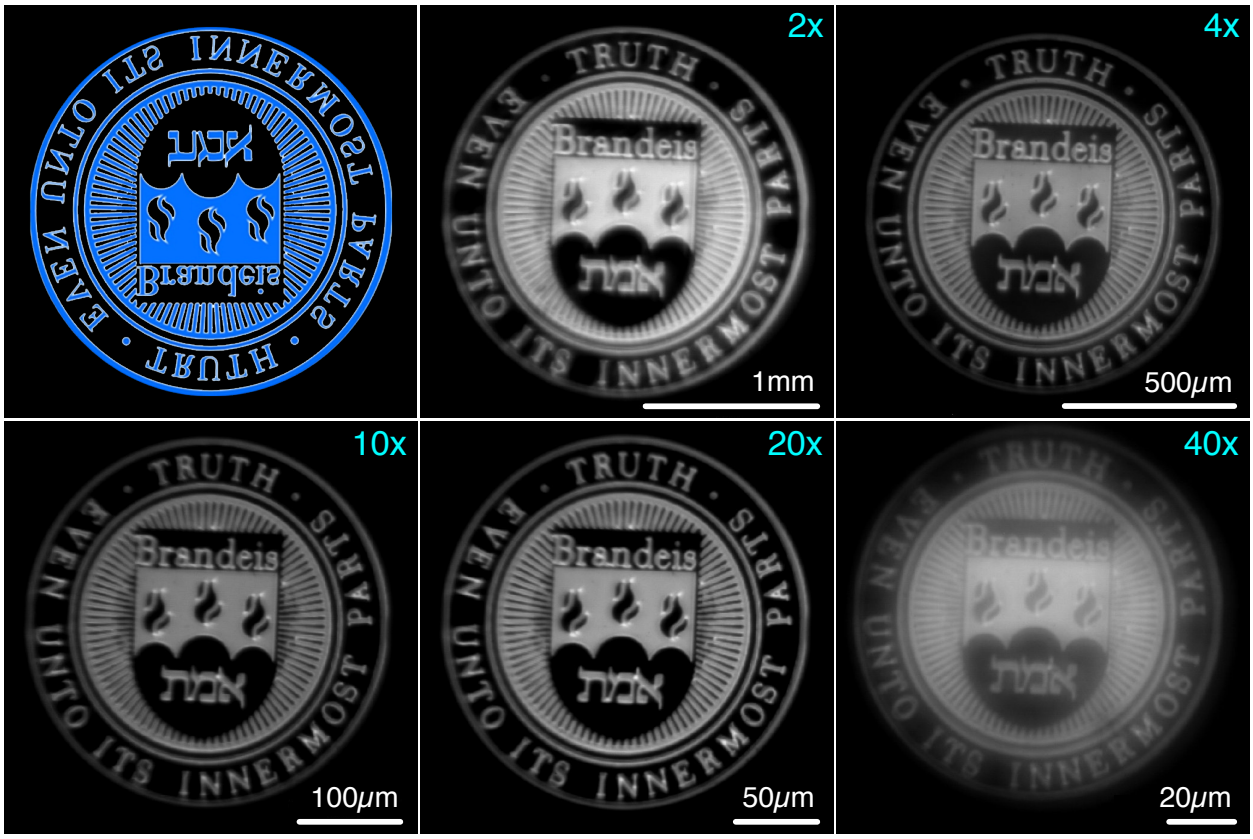

Figure 3.4: The Brandeis seal as imaged when projected onto a glass slide through various microscope objectives. In each case the image was taken twice, once onto a clean glass slide (shown here) and once onto a 100μm grid for measurement (not shown). Top left: The image being projected. The scale bars in the images above are: 2x objective, 1mm scale bar; 4x objective, 500μm scale bar; 10x objective, 100μm scale bar; 20x objective, 50μm scale bar; and 40x objective, 20μm scale bar. Image adapted from [119].

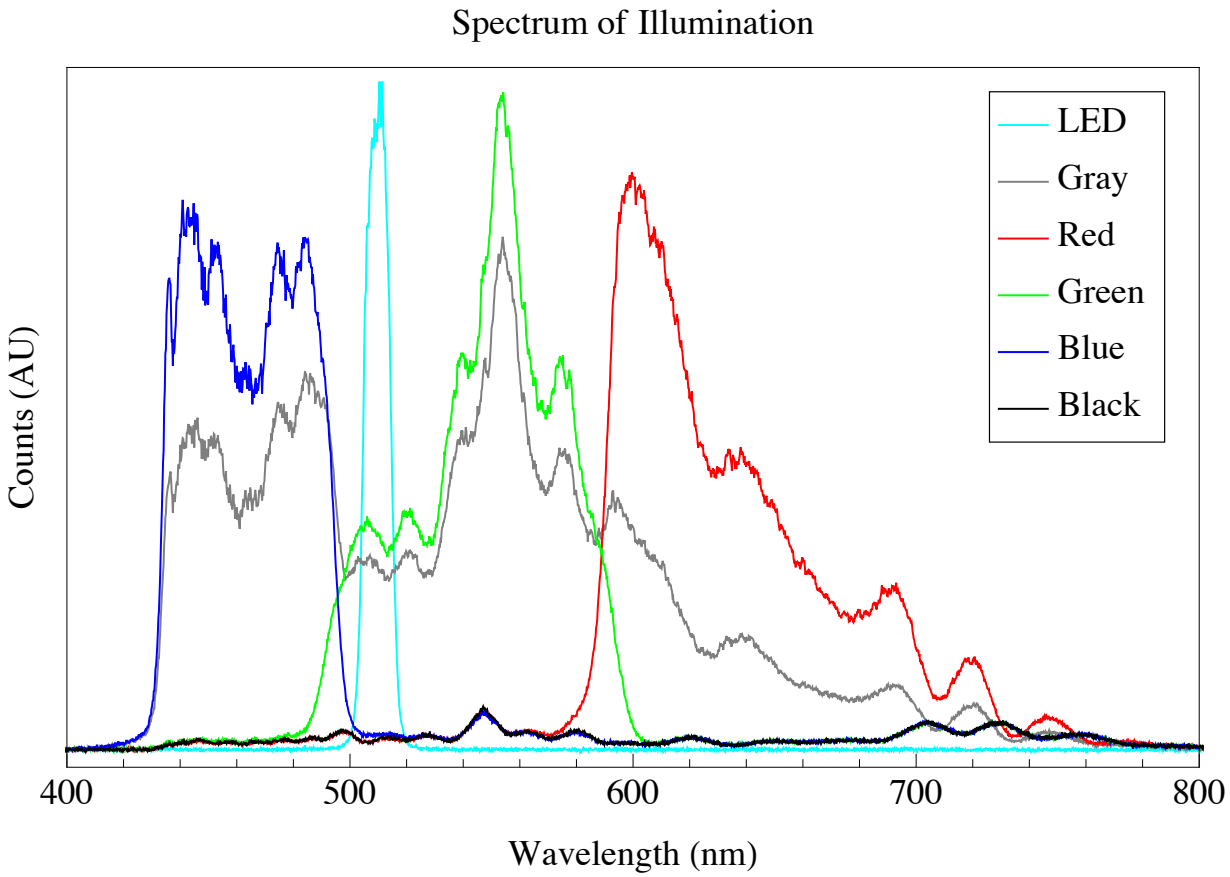

Figure 3.5: The illumination spectrum of the PIM as measured on the sample stage. The LED is a high power cyan LED through a 510 ± 10nm filter, the projector was set to project a solid screen of Red (RGB[50,0,0]), Green (RGB[0,50,0]), Blue (RGB[0,0,50]), Black (RGB[0,0,0]), or Gray (RGB[50,50,50]). Image adapted from [119].

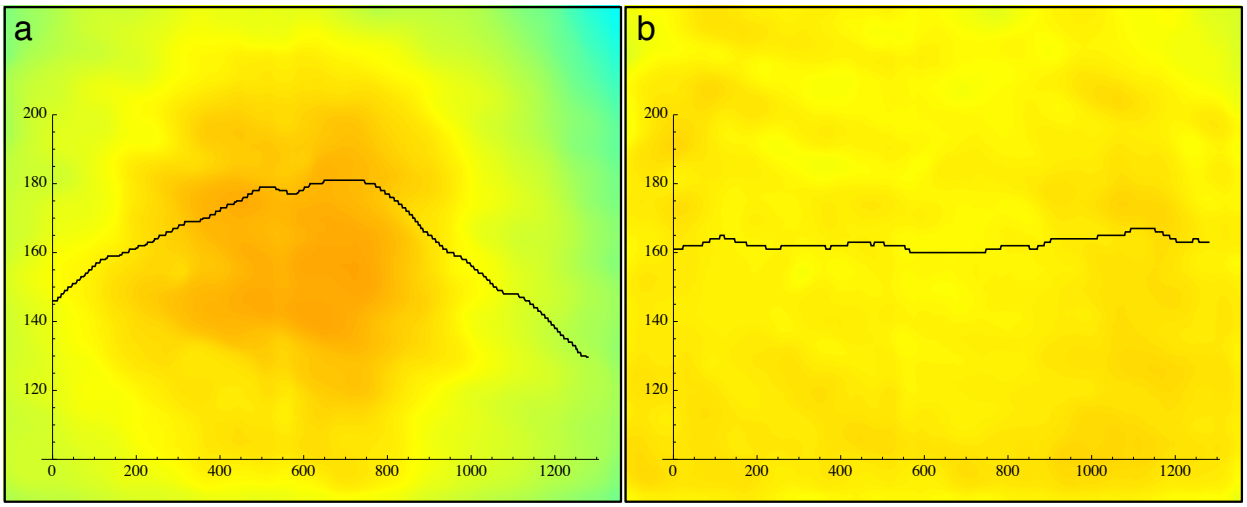

Figure 3.6: The illumination of the sample before and after software flattening of the PIM. Shown are pseudocolor images of a clean sheet of glass with a representative intensity trace superimposed (pixel value vs pixel position). In both cases the image was median filtered to remove noise. a) An image where a spatially uniform illumination of RGB[0,0,125] is projected. Superimposed is a horizontal trace across the center of the field of view with a variation of 8.6%. b) An image where the illumination has been flattened using the formula in the text with $f = 0.25$ and $n = 0.95$. Superimposed is a horizontal trace across the center of the field of view with a variation of 1.1%. The corrected and uncorrected illumination are both scaled to align with the field of view. Regions of the field of projection outside the field of view were not illuminated. Image adapted from [119].

3.2.2 Software

Our systems are controlled by software written in Matlab (2011a) and running on an iMac (Mid-2010 dual-core i3), equipment readily available inexpensively to most institutions. A less expensive computer running the open-source GNU Octave software package in place of Matlab could also be used with minimal loss of functionality. Each iteration of the software cycle can be broadly separated into three steps; image acquisition, analysis, and image projection. The steps run sequentially within a simple `for` loop after an initialization process which preallocates all of the required variables. The image acquisition process collects an image from the camera for use in the object analysis step, the object analysis step runs all of the required code to determine what image is to be projected onto the sample, and the image projection step then projects the calculated image onto the sample for a prescribed duration. During each iteration five items are saved to the computer; the raw image from the first step, a tracking image where all of the tracked objects are labeled, the calculated projection, an image from the camera during projection, and the internal variables. Examples of the three images collected can be seen in Figure 3.7 and an illustration of the software flow can be seen in Figure 3.8.

A critical step in setting up a new PIM is the alignment of the field of projection with the field of view. This step allows for the active feedback control software to illuminate any object within the field of view automatically. See Appendix A and Figure A.1 for more details on aligning the PIM. It is recommended that the alignment be checked before each use of the PIM as depending on the materials used and the rigidity of the physical apparatus the alignment may drift slightly from day to day.

The image acquisition step of the control software will depend entirely on the software system/coding language being used. Our system within Matlab makes use of the Image

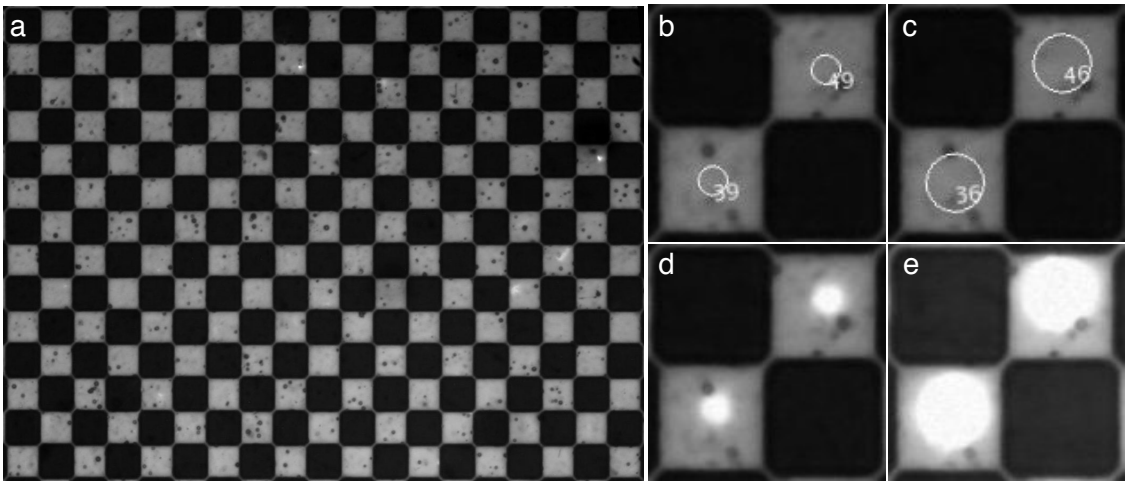

Figure 3.7: Examples of images saved during each iteration of the control software of the PIM. a) The raw image collected imaging the checkerboard alignment grid at 4x magnification. The squares are $100\mu m$ per side. b-c) Labels and opening shapes superimposed over a small region of the raw image. b) Disk of radius 8 pixels. c) Disk of radius 16 pixels. d-e) A small region of the image taken while projecting a dot matching the opening object. d) Disk of radius 8 pixels. e) Disk of radius 16 pixels. Image adapted from [119].

Acquisition Toolbox and the `getdata` command.

The analysis step runs through a few subprocesses to track the objects within the field of view and calculate the image the be projected. These processes can be described as image analysis, object tracking, object analysis, and image calculation.

Image Analysis: The image analysis consists of thresholding the image to black and white (`im2bw`), morphological opening (`imopen`), and object labeling (`bwlabel`). Morphological opening is a standard image processing technique used to find objects of a predetermined shape and size [98, 67]. Object labeling is another standard image processing technique where isolated blocks of ones are identified and given unique labels. The labels are applied as colors to demonstrate the output of morphological opening in Figure 3.8. These labeled objects can also have data such as their area, centroid, or average pixel value extracted for further analysis. The centroids of these objects and size of the disk used in their opening

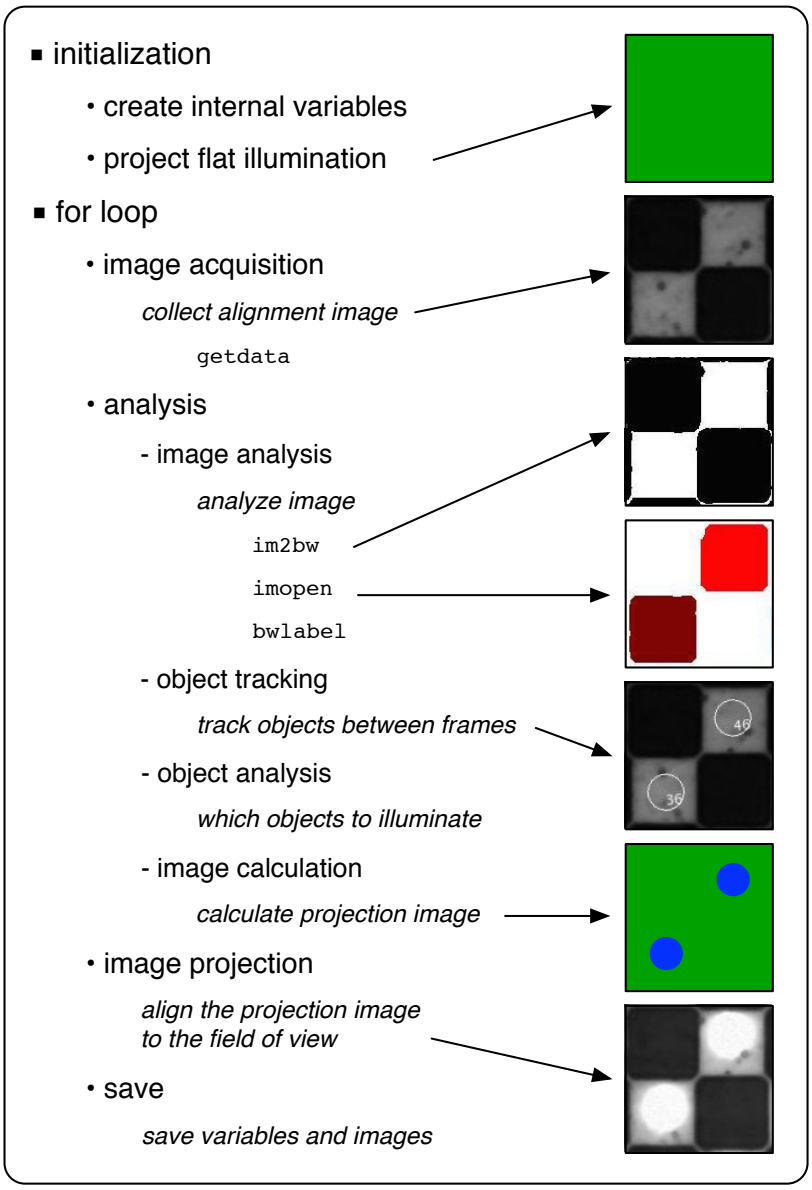

Figure 3.8: An illustration of the software flow for the PIM. After an initialization sequence a `for` loop runs for each frame to be collected. Within each iteration of the `for` loop the process can be separated into image acquisition, analysis, and image projection steps. The bulk of the process is within the analysis step which can be further separated into image analysis, object tracking, object analysis, and image calculation subprocesses. The images at right illustrate the flat illumination, an image of the checkerboard alignment grid with flat illumination, thresholded image, opened image, tracked image, programmed illumination, and an image with programmed illumination. Image adapted from [119].

is used to demonstrated the output of labeling in Figure 3.8. Tuning the thresholding and opening parameters within this process are critical for successful operation of the control software. Standalone routines were created to predetermine these values.

Object Tracking: The preallocation process runs the above image analysis subprocess and creates an "Objects" matrix which is the heart of the object tracking process. This matrix stores the size, position, velocity, and activity of every identified object within the field of view. The labeling process of the image analysis subroutine returns an integer list of objects that is based solely on their position within the current image and is often not comparable between frames. The object tracking subprocess fixes this problem by identifying the object label within the current frame to the object number being tracked between frames. For each iteration the objects detected in the image analysis subprocess are compared with the matrix of objects being tracked using a weighting algorithm that compares the size and position of the current object with the predicted size and positions of the previously tracked objects. Whichever preexisting object has the lowest weight is associated with the current labeled object. If no preexisting object has a weight below a certain threshold then the current object is considered new and the "Objects" matrix has a new entry added with its information. If a preexisting object is not associated with any object in the current frame it is marked as inactive to indicate it is not currently present. This process allows for objects to be tracked as they enter and leave the field of view while maintaining a memory of their previous activity. See Figure 3.9 for an illustration of objects being tracked in time.

Object Analysis: The object analysis process will depend strongly on the desired application of the microscope. For our purposes the mean intensity of each object is sampled and compared to that same object's intensity in previous frames. This allows us to determine the oxidation state of the chemical oscillators within the field of view. The object tracking subprocess above allows for objects to be compared against themselves from previous frames

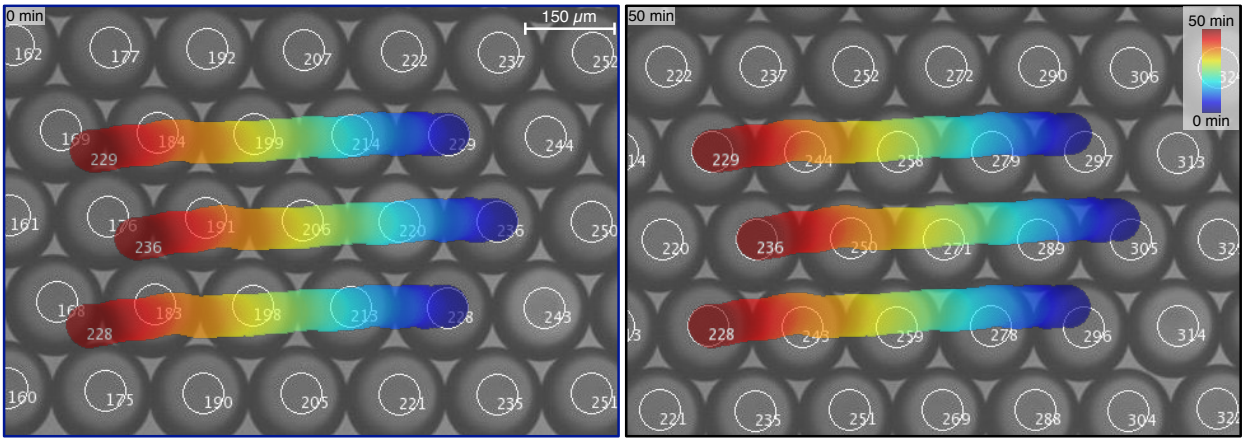

Figure 3.9: Droplets of a water-in-oil emulsion being tracked by the PIM as the drops move in a glass capillary. The images are a small section of a larger field of view taken 50 minutes apart. The superimposed traces indicate the locations of three objects tracked over time. Objects moving in from the right are assigned new numbers. Image adapted from [119].

even if they move within the field of view.

Image Calculation: The image calculation process will depend strongly on the desired application of the microscope. For our purposes various metrics are calculated from the oxidation states of the chemical oscillators and those satisfying certain criteria are illuminated with a circle of light while those that don't satisfy the criteria are not. The object tracking and object analysis subprocesses allow for the flexibility of illuminating specific locations at specifics times with specific colors and intensities without any user intervention.

Image Projection: After the analysis processes have finished the calculated image is projected onto the sample for a prescribed duration. Projection is carried out by displaying the image fullscreen on a second display attached to the computer. This second display is connected to the projector so that the second display shows exactly what is being projected at all times. To align the projector and sample the calculated image is shifted in position, size, and orientation to align with the field of view based on the optics of the hardware. This software alignment of the projected image is key to the successful operation of the

microscope. The parameters of alignment will depend entirely on the implementation of the microscope being used. For example, two systems we have created vary in that one flips the image vertically while the other flips the image horizontally and both have different alignments of the field of view with the field of projection. In both cases the field of view is a subset of the field of projection allowing for the projected illumination to access the entire field of view. These parameters should be checked and fine-tuned before every usage of the microscope.

Finally, at the end of every iteration the projector is returned to a blank screen in preparation for the next frame, the collected images are saved, the calculated projection is saved, and the internal variables are saved. Saving the variables with each iteration and recording the saved images as a series of stills rather than frames within a movie prevents loss of data if the control software is terminated prematurely. For our purposes images are typically collected one image every ten seconds while tracking up to 300 objects to create a time-lapse video of the chemical processes being observed. A stripped down version of our software has been used to collect images at three frames per second while tracking twenty objects. The limiting factors for the frame rate are the number of objects being simultaneously tracked, the complexity of the calculations being performed on the tracked objects, the desired duration of projection for each frame, and of course the specifications of the computer running the code. More sophisticated software running in a more fundamental programming language such as Python or C could also increase the maximal frame rate.

3.3 Applications

The PIM described here can be used as an inexpensive programmable illumination microscope for uses in a variety of experimental fields including optogenetics, microfabrication,

biophysics, chemistry, nonlinear dynamics, and computer science. Any technique that requires (or could benefit from) spatially or temporally structured illumination could potentially be implemented on a PIM. The active feedback control software introduces a new and innovative approach for targeted and patterned illumination.

In optogenetics the PIM at low magnification could potentially be used to track entire organisms such as *C. elegans* and manipulate the illumination at different macroscopic portions of the organisms anatomy [105]. At higher magnification the PIM could localize illumination on specific microscopic anatomical substructures with a programmable temporal sequence which can include responding to cues from within the field of view.

In microfabrication the PIM can serve as a maskless photolithography system for "g-line" ($436nm$) photoresists such as Shipley-1813 [75] and OFPR-800 [40]. With significant modifications DLP projectors can even be used with more typical "i-line" (365nm) SU-8 photoresists [77]. The scale of the structures to be manufactured can easily be adjusted by changing the magnification of the objective.

In biophysics the PIM could be a valuable tool in the study of the phototactic motility of *Chlamydomonas reinhardtii* [138]. The entire organism could be tracked with targeted optical perturbation for demonstrations and measurements of the phototactic response.

In chemistry the PIM can be used to study and demonstrate the emergence of stationary Turing patterns in the Chlorine Dioxide–Iodine–Malonic Acid (CDIMA) and related reactions [76].

In nonlinear dynamics the PIM has been used to control the boundary conditions and initial conditions on systems of diffusively chemical oscillators [124]. Here the PIM allowed for the first direct experimental testing of Turing's 60 year old mathematical theory.

In computer science the PIM can be used to create and demonstrate chemical Boolean logic gates in oscillatory chemical media [106] and to find the optimal solution to modifiable

labyrinths and mazes [104].

The above are only a small sampling of what the PIM could potentially be used for. The modular design and inexpensive components allow for rapid construction and modification for a variety of purposes. The active feedback control software allows for realtime algorithmic illumination that can be targeted and patterned both spatially and temporally. Combining the powerful capability with the accessibility of the concepts required for assembly of the hardware and writing of the software the PIM is an ideal tool for a teaching laboratory.

Chapter 4

Testing Turing's Theory of Morphogenesis in Chemical Cells

This chapter is adapted from [120] which has been published by the *Proceedings of the National Academy of Sciences of the United States of America*.

Abstract

Alan Turing, in *The Chemical Basis of Morphogenesis*, described how, in circular arrays of identical biological cells, diffusion can interact with chemical reactions to generate up to six periodic spatio-temporal chemical structures. Turing proposed that one of these structures, a stationary pattern with a chemically determined wavelength, is responsible for differentiation. We quantitatively test Turing's ideas in a cellular chemical system consisting of an emulsion of aqueous droplets containing the Belousov-Zhabotinsky oscillatory chemical reactants, dispersed in oil, and demonstrate that reaction-diffusion processes lead to chemical differentiation, which drives physical morphogenesis in chemical cells. We observe five of the

six structures predicted by Turing. In two-dimensional hexagonal arrays, a seventh structure emerges, incompatible with Turing's original model, which we explain by modifying the theory to include heterogeneity.

4.1 Introduction

The Turing model of morphogenesis offers an explanation for how identical biological cells differentiate and change shape [124]. It is difficult to overstate the impact Turing's model has had on developmental biology and the broad field of reaction-diffusion systems [43, 48, 69, 74, 68, 92, 73, 100]. The Turing model consists of two cases; the first, applicable for a ring of continuous material, has been experimentally confirmed in chemical systems [83, 7, 88, 19, 36]. The second case, relevant to biology, consists of a ring of discrete cells, each of which contains interacting chemical species that can diffuse to neighboring cells through a chemical selective membrane. However, as the two theories for the cases are different, establishing the Turing model for continuous systems does not prove that the model holds when the chemistry is compartmentalized. Due to challenges in microfabrication, the case of a ring of cells has not previously been experimentally tested in chemical systems. In biology, where networks of cells arise naturally, the Turing model remains controversial because comparison of experiment and theory is hampered by incomplete knowledge of the morphogens involved in development, the rate constants of the reactions, the mechanisms of intercellular coupling and the role of elasticity [74, 92, 38, 58].

We report an experimental reaction-diffusion system ideally suited for testing Turing's ideas in synthetic "cells" consisting of microfluidically produced surfactant-stabilized emulsions [116, 13] in which aqueous droplets containing the Belousov-Zhabotinsky oscillatory chemical reactants [143] are dispersed in oil. In contrast to biology, here the chemistry is

understood, rate constants are known and interdrop coupling is purely diffusive. We explore a large set of parameters through control of concentrations, drop size, spacing, and spatial arrangement of the drops in lines and rings in one dimension and hexagonal arrays in two dimensions. Quantitative comparison of theory and experiment reveals two surprises; a new structure is observed and we measure coupling strengths orders of magnitude weaker than predicted. Nevertheless, in the majority of cases, we find Turing's model to be exceedingly accurate. Most significantly, we experimentally establish Turing's prediction that interacting identical cells differentiate into chemically distinct populations, which subsequently transform physically in size, thereby demonstrating that these synthetic cells are pluripotent and that abiotic materials can undergo morphogenesis via the Turing mechanism. For one-dimensional arrays of drops, we observe six distinct spatio-temporal patterns, all of which are predicted by the Turing model. In closed-packed two-dimensional arrays, we observe an additional pattern, of a mixed spatial-temporal nature that is incompatible with Turing's original model. We develop a theory, capable of describing this novel pattern, which posits that the pattern arises from nonlinearity coupled with slight heterogeneity in cellular chemistry and/or coupling strength. As our theory is generic, and heterogeneity is ubiquitous in nature, we expect this pattern to occur in a wide range of reaction-diffusion systems.

The Belousov-Zhabotinsky (BZ) reaction [143], the metal ion-catalyzed oscillatory oxidation of an organic substrate, typically malonic acid (MA), by acidic bromate, has become the prototype of nonlinear dynamics in chemistry [24] and a preferred system for exploring the behavior of coupled nonlinear oscillators [28]. Our system consists of a monodisperse emulsion of drops of aqueous BZ solution, whose diameter ranges from 20 μm to 200 μm dispersed in a continuous phase of oil [116, 13]. The drops are surfactant-stabilized to prevent coalescence [35]. Chemical coupling between drops is mediated through a small subset of less polar intermediates; primarily an inhibitory component, bromine (Br_2), and to a lesser

degree, two excitatory components, bromine dioxide ($BrO_2^\bullet$) and bromous acid ($HBrO_2$), which diffuse from drop to drop through the intervening oil. Here, because the inhibitory bromine strongly partitions into the oil, whereas the excitatory bromous acid does so only weakly, it is possible to satisfy the long-range inhibition and short-range excitation condition needed for the stationary Turing instability [68]. Since the system is closed and the BZ reactants are not replenished, the reaction lasts no more than about 100 oscillations until the final uniform equilibrium state is approached. However, the system evolves sufficiently slowly that it can adiabatically exhibit the dynamical instabilities predicted by Turing for open systems [117, 116, 13].

Stationary Turing patterns have been notoriously difficult to produce experimentally, primarily because, for the activator-inhibitor dynamics that typically provides the necessary feedback, the inhibitor must diffuse significantly more rapidly than the activator [68]. This condition, which cannot be satisfied with small molecules in homogeneous solution, was first fulfilled, 40 years after Turing's paper, in the chlorite-iodide-malonic acid (CIMA) system, with the activator being complexed to starch, which slows activator transport [7, 88]. Stationary Turing states were also observed in a BZ microemulsion consisting of reverse micelles [127, 21]. The activator, polar $HBrO_2$, resides in the aqueous interior of the micelle. The inhibitor, nonpolar Br_2, permeates into the oil phase. The transport of the micelles is much slower than the transport of bromine; hence the criterion for the stationary Turing instability is met. The distinction between the micelles employed previously [127, 21] and the emulsions we study here [116, 13] is that the micelles are in dynamic equilibrium; they merge and split on a time scale much shorter than the period of a BZ oscillation and a length scale much shorter than the wavelength of the chemical wave. Therefore, on the time and length scales appropriate for a continuum description of the reaction-diffusion system, the BZ microemulsion can be considered to be homogeneous in composition. In this sense, the

BZ microemulsion and the CIMA-starch system share a continuum description. The BZ emulsions studied here are fundamentally different, in that they consist of discrete immobile chemical compartments that never merge. The microfluidic emulsion system presented here is spatially heterogeneous, while the micelle and CIMA-starch systems are spatially homogeneous on the relevant time scales.

4.2 Methods

We generate our drops using flow focusing microfluidic PDMS chips designed and manufactured by the group using standard methods. The BZ reactants are introduced in two separate streams to prevent the reaction from starting prior to on-chip mixing. One stream contains the catalysts and bromate, while the other stream contains the acids and bromide. The exact dimensions and flow rates vary based on the desired drop size. The oil used is a commercially available fluorocarbon oil (3M, HFE 7500) stabilized by a surfactant designed by the Weitz Group at Harvard (obtained from RainDance Technologies, the Weitz Lab, and RAN Biotechnologies). The drops typically have a coefficient of size variation of about 1%. When loaded into a rectangular capillary of height slightly less than the drop diameter, the drops self-assemble into a closed-packed two dimensional hexagonal lattice. See Table 4.1 for the chemical and physical parameters used for the experimental data presented here.

We add the photosensitive catalyst ruthenium-*tris*(2,2-bipyridyl) (Rubpy) to the BZ mix, which has the effect that, as long as blue light is shone on the drops, they are held in the reduced steady state. Therefore, light can be used to create constant chemical boundary conditions for networks of non-illuminated drops. The emulsion is illuminated by two sources, a 510 nm filtered Köhler illumination setup for imaging and a modified commercial data projector for photoinhibition [119]. Imaging is done at 510 nm, as this wavelength

Table 4.1: Experimental conditions for each observed state. In all experiments 80 mM sulfuric acid, 300 mM sodium bromate, and 3 mM ferroin were used. The addition of sodium bromide (up to 10 mM) has been seen to only change the initial conditions. The concentration of Rubpy (up to 2 mM) has been seen to only change the optical isolation capabilities.

State	MA	Drop	Oil	NaBr	Rubpy	Capillary
Turing a	10mM	130μm	20μm	-	0.4mM	100μm Round
Turing b	2.4M	230μm	100μm	10mM	0.4mM	100μm Round
Turing c	20mM	98μm	0/47μm	-	0.4mM	100μm Round
Turing d	40mM	95μm	0μm	-	0.4mM	100μm Round
Turing e	640mM	117μm	3μm	10mM	0.4mM	100μm Round
Turing f	380mM	106μm	25μm	10mM	0.4mM	100μm Round
Rings	640mM	150μm	0μm	10mM	1.2mM	100μm Flat
$s0\pi$	640mM	70μm	0μm	10mM	0.4mM	100μm Flat
Morpho	200mM	66μm	0μm	-	0.4mM	50μm Flat

does not interact with the Rubpy, is opaque to ferroin, and transparent to ferriin. Thus 510 nm is passive imaging where the oxidation state of each drop is immediately viewable by its transmission intensity. The commercial projector is only modified to focus through the microscope objective; the light source and color functionality are unaltered, as Rubpy is sensitive to 450 nm light, which is within the the projector's RGB "blue" output. Optical isolation is achieved by Matlab code written by the group, which tracks each drop for movement and places a dot of blue light over the center of every drop that is to be inhibited. In experiments a duty cycle of 3 s on / 7 s off is used for optical inhibition. As the BZ oscillation frequency is at least an order of magnitude less than the inhibition frequency, the temporal variation in the light is effectively averaged. Data are collected while the inhibitory light is off. The size, intensity, and duty cycle of the illumination are determined by empirically establishing the minimum inhibitory exposure for each experimental condition. An isolated ring of active drops from a 2D array is shown in Figure 4.1.

This method can also be used to probe the range of interaction between drops. If all

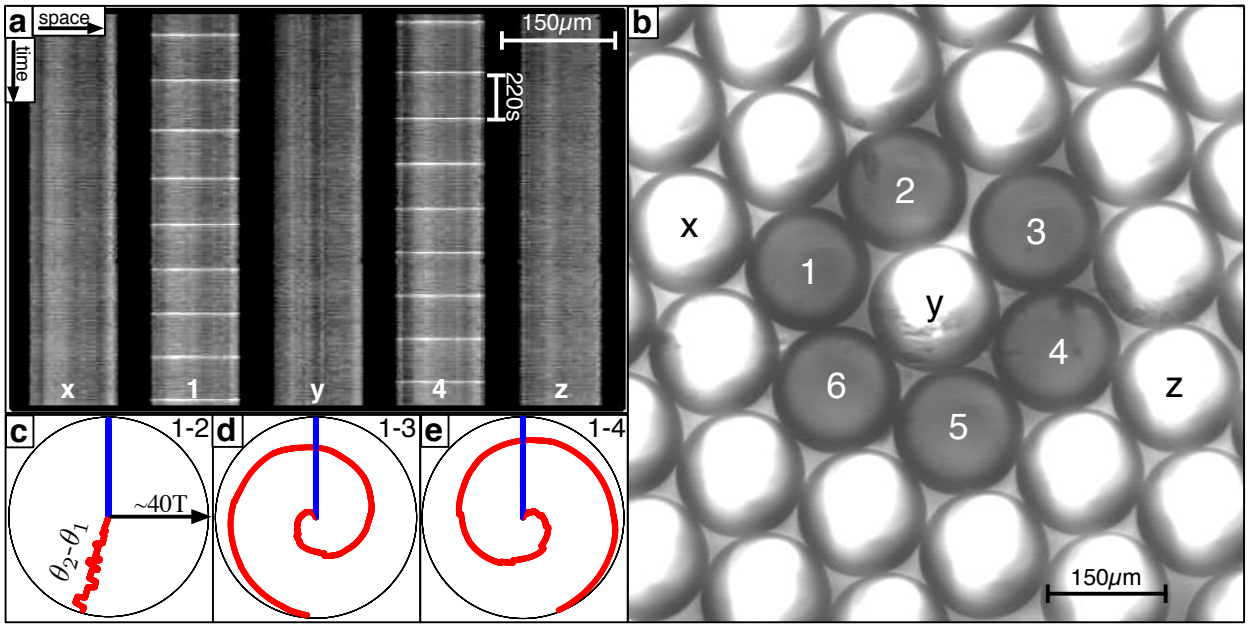

Figure 4.1: Optical isolation is achieved by utilizing the fact that illuminated drops have constant chemical conditions corresponding to the reduced state. **a)** A space time plot of the drops x-1-y-4-z shown in (b). For this space-time plot, all but drops 1 and 4 were illuminated. Drops 1 and 4 oscillate; the rest were held constant in the reduced state. **b)** An image illustrating the selective illumination of droplets to create a ring of six drops. **c-e)** Radial phase-time plots of optically isolated drops (time is the radial dimension, zero in the center, and phase is relative to drop 1). In each plot only two drops are allowed to oscillate; all others are optically inhibited. These experiments last ∼40 drop periods. **c)** Drops 1-2 are phase locked with a phase difference of ∼170 degrees. **d-e)** Drops 1-3 and drops 1-4 are asynchronous and drift $\sim 2\pi$ out of phase after ∼40 periods. All drops contain 300 mM bromate, 3 mM ferroin, 1.2 mM Rubpy, 80 mM acid, 400 mM MA, and 10 mM NaBr. Drop size is $\sim 150\mu$m. Image adapted from [120].

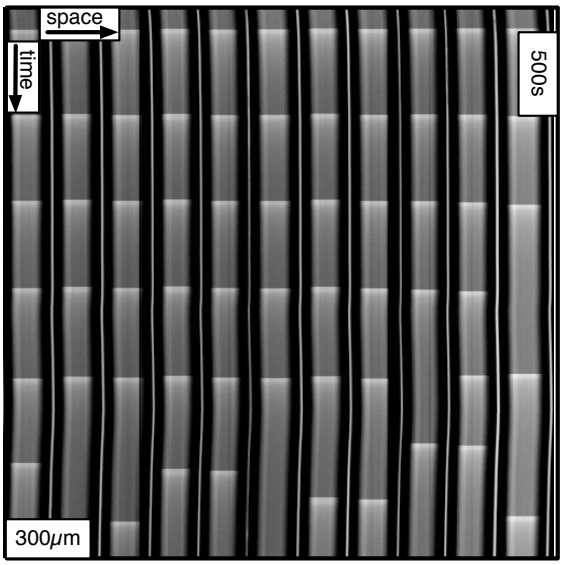

Figure 4.2: Space-time plot illustrating transient behavior. Drops, in conditions corresponding to Turing case (e) were initiated all in phase by application of a long pulse of light. After two oscillations the system adjusts to Turing instability (e), (q, ω). Chemical conditions: 20 mM MA, 80 mM H_2SO_4, 300 mM $NaBrO_3$, 3 mM ferroin, no NaBr, 0.4 mM Rubpy, drop size $\sim$140μm, and oil gap $\sim$10μm. Image adapted from [120].

but drops 1 and 2 in Figure 4.1 are illuminated, these two adjacent drops synchronize, but if all but drops 1 and 3, or all but drops 1 and 4 are illuminated, then the phase difference between these drops increases linearly in time, demonstrating that nearest neighbor drops are coupled, while next nearest neighbors are uncoupled. Single drops, optically isolated from all others, differ in frequency by less than 3%, as illustrated by the fact that about 40 cycles are required for a phase difference of 2π to develop between nonadjacent drops.

Another feature of adding the photosensitive catalyst Rubpy to the BZ mix beyond the ability to set boundary conditions is the ability to set the initial conditions. By exposing the entire system to a bright pulse of light we can "reset" the phase of all of the oscillators to create an initial in-phase state as seen experimentally in Figure 4.2. Depending on the chemical conditions of the system, this state may or may not be stable.

Data are analyzed in real time during data acquisition using Matlab code written by the group, which algorithmically detects each drop and calculates the average pixel value for each drop in each frame. For each drop a time series of pixel values is used to determine the periodic peaks, which correspond to the oxidation spikes of the BZ reaction. These spikes are defined as phase zero, and the interspike interval is used to define the period for that oscillation and to linearly define the phases between each spike. The period and phase information can then be used by the data acquisition code in determining which drops are to be inhibited and when. Further post-acquisition data analysis is possible by calculating an order parameter for each upright triangle of drops using the phases or phase differences.

4.3 Model

To quantitatively test the Turing model in discrete cells, it is necessary to control the boundary and initial conditions for all of the cells. We employ mixed boundary conditions; part of the surface enclosing the cells under study consists of other cells in which the chemical concentrations are held constant, and part is a glass wall impenetrable to all chemicals and thereby imposes a no-flux condition. Constant chemical boundaries were created by exploiting the photosensitivity of the BZ catalyst, Rubpy. We produced 1D linear and 2D hexagonal arrays of drops by filling cylindrical and rectangular capillaries, respectively, and used a computer projector coupled to a light microscope to generate patterned illumination [13] in which each drop could be independently illuminated. This flexible illumination system allowed us to isolate either pairs of drops, or a ring of active drops from a 2D array, as shown in Figure 4.1, with experimental conditions specified in Table 4.1. Initial conditions were set by inhibiting all drops with light and then disinhibiting individual selected cells by extinguishing their illumination at prescribed times, thereby allowing the chemical dynamics

to proceed.

To construct a tractable model, Turing assumed cells were chemically uniform, small objects and considered the membranes separating cells as chemically specific barriers to diffusion, ignoring any chemical reaction or accumulation of chemicals in the membrane. Turing's resulting reaction-diffusion model consists of a ring of point cells diffusively connected directly to nearest neighbors, expressed as a set of equations each of the form [124]

$$\frac{d\boldsymbol{c}_i}{dt} = \boldsymbol{F_c}(\boldsymbol{c}_i) + \boldsymbol{M_c}\left(\boldsymbol{c}_{i-1} + \boldsymbol{c}_{i+1} - 2\boldsymbol{c}_i\right) \tag{4.1}$$

where $\boldsymbol{c}_i$ is a vector containing the concentrations of the species in the i^{th} cell, $\boldsymbol{F_c}$ is a vector function describing the kinetics of the c-species, and $\boldsymbol{M_c}$ is a diagonal matrix containing the coefficients of diffusive transport (μ_c) of the c-species between drops. We describe the chemical kinetics, $\boldsymbol{F_c}$, of the BZ chemistry with a model developed by Vanag and Epstein [129, 131] (VE model, Equations D.1) that considers four concentrations to vary in time: the inhibitory components bromine (Br_2) and bromide (Br^-), the oxidized form of the catalyst (ferriin), and the activator bromous acid ($HBrO_2$). The four VE reaction rates, $\boldsymbol{F_c}$, contain the aforementioned 4 variable chemical species, 4 more chemicals, whose concentrations are approximated as constants in the model, and 9 known rate constants; $\boldsymbol{F_c}$ has zero adjustable parameters. Turing did not specify how the coupling strength μ_c varies with the physical-chemical parameters. In order to compare theory with experiment, we supplement the Turing model by explicitly calculating the coupling strength between drops in a capillary using Turing's assumptions noted above, with the caveat that different results arise depending on the assumptions used to produce a geometric point model [128, 131].

$$\mu_c = \frac{2D_cP_c\left(b+d\right)}{d^2\left(a+b\right)}\left(\ln\left(\frac{b+d}{b}\right) + \frac{a-d}{b+d}\ln\left(\frac{a-d}{a}\right)\right) \tag{4.2}$$

See Appendix C and Figure 4.3 for details of the calculation. D_c and P_c are the diffusion and partition coefficients of the c-species in the oil, a is the length of the BZ drop, b is the length of the oil gap separating drops, d is the diameter of the capillary. The only parameter not measured in Equation 4.2 is the partition coefficient of $HBrO_2$, P_x.

To elucidate this model, Turing [124] used linear stability analysis (LSA) and identified six possible chemical structures in rings of diffusively coupled identical cells. In LSA, one characterizes how the steady state concentrations, i.e., those for which $dc_i/dt = 0$, respond to small perturbations. If all perturbations decay, then the system is in a stable steady state. However, if any perturbations grow with time, the steady state is unstable, and the fastest growing perturbation is labeled a Turing instability. See Appendix D for a LSA of a ring of drops using the VE model. For a ring of N cells the requirement of periodicity restricts dimensionless wavevectors of the perturbations to take on one of three possible values; $q_{\min} = 0$, $q_{\max} = 2\pi s_{\max}/N$, where for even numbered rings $s_{\max} = N/2$ and for odd rings $s_{\max} = (N-1)/2$, and $q = 2\pi s/N$ where the integer s ranges from $0 < s < s_{\max}$. For each possible q, the perturbation growth can be either oscillatory with frequency $\omega > 0$, or non-oscillatory with $\omega = 0$, giving a total of six possible instabilities. Following Turing's nomenclature, the six instabilities (a-f) are each characterized by a wavevector and frequency, (q,ω), as follows: Turing case (a)-($q_{\min}$, 0), (b)-($q_{\min}$, ω), (c)-($q_{\max}$, 0), (d)-(q, 0), (e)-(q, ω), and (f)-($q_{\max}$, ω).

The simulations were conducted using the VE model, Equations 4.1 and D.1, with the same parameters as used in the LSA (Table 4.2). The nonlinear simulations (NLS) consisted of 40 identical BZ drops diffusively coupled through chemical species u (inhibitor) and x (excitator) with periodic boundary conditions. Different initial conditions were used for each drop and each trial. The initial conditions for the 40 drops were generated from a normal distribution (with coefficient of variation of 20% in each chemical species) around the steady

Table 4.2: Simulation parameters and their experimental counterparts. In the VE model, the inclusion of sodium bromide, only changes the initial value of y and Rubpy is not differentiated from Ferroin as z is the sum of both catalysts. The physical parameters a, b, d, D, and P are included in the diffusion term μ as described in Appendix C. Other rate constants used are: k_1=2×10^6, k_2=$2h^2A$, k_3=3000, k_4=$42hA$, k_7=$29m$, k_{10}=$0.05m$, k_r=2×10^8, k_{red}=5×10^6, and c_{min}=$\sqrt{2k_rc_0(k_9+k_{10})/k_{red}^2}$. The value of k_9 depends on m such that k_9=$0.12m$ for $m > 0.1$ and k_9=$0.07m$ for $m \leq 0.1$.

Parameter	Counterpart	Value	Type
A	Sodium Bromate	0.3	Constant
c_0	Total Catalyst	0.003/0.0042	Constant
h	Hydrogen Ions	0.16	Constant
m	Malonic Acid	varies	Constant
μ	Coupling Strength	varies	Constant
x	Activator $HBrO_2$	variable	Intermediary
y	Inhibitor Br^-	variable	Intermediary
z	Oxidized Catalyst	variable	Intermediary
u	Communicator Br_2	variable	Intermediary

state of the system. When the system oscillates, the reduced state of the oscillation has concentrations close to the steady state. For most of the state diagram, the steady state was unstable; only for extremely low values of malonic acid was the steady state stable.

Numerical investigation of the NLS model revealed that malonic acid concentration (m) and coupling strength (μ) are the two parameters that most greatly affect the state diagram of the system (Figure 4.5). To generate the NLS state diagram, we systematically varied the parameters μ and m and integrated Equations 4.1 long enough for the system to settle on a stable attractor. From the space-time plot we could identify whether or not the attractor was a Turing state and to which case the attractor belonged. Similar to the LSA, *there are no adjustable parameters in calculating the nonlinear state diagram.*

The Turing model, by which we mean the nonlinear rate and coupling Equations 4.1, incorporates two significant and untested approximations; considering each cell as a point and simplification of chemical transport by elimination of explicit consideration of the in-

tracellular medium (the oil in our experiments). Furthermore, the use of linear stability analysis introduces an additional, severe approximation. The power of the Turing model is that it provides unambiguous physical mechanisms to explain chemical dynamics and morphogenesis. However, as noted by Turing [124], "This model will be a simplification and an idealization, and consequently a falsification." This raises the question to what degree do the Turing model and its linear stability analysis describe experiment? The answer to this question is of importance to the broad field of reaction-diffusion systems, as over a thousand papers have been published that have built upon the Turing model, which, prior to this work, has not been experimentally tested for networks of diffusively coupled cells [69]. Here, we address six fundamental questions facing reaction-diffusion systems in general: (*i*) How well does the simplified coupling term, μ_c, agree with experiment? (*ii*) Are there more or fewer than the six predicted Turing linear instabilities? (*iii*) How are the linear instabilities modified by nonlinearities? (*iv*) Does the Turing model provide quantitative and predictive understanding of experiment? (*v*) How do chemical patterns depend on the dimensionality? (*vi*) Do cells sequentially undergo chemical and then physical morphogenesis?

4.4 Results

As a first experimental test of the Turing model, Equation 4.1, for cells, we measured the synchronization dynamics of two weakly inhibitory coupled drops at moderate malonic acid concentrations, where uncoupled drops oscillate and bromine can be considered as the sole intercell transporter [13], i.e. $P_x = 0$. We filled cylindrical capillaries with drops, used light both to chemically isolate a pair of adjacent drops and to set the initial phase difference between the isolated drops, and measured the phase difference between the two drops as a function of time, as shown in Figure 4.3. Viewed in transmission, the oxidized state appears

bright, while the reduced state appears dark. Ultimately, the drops synchronize with a phase difference of π radians [52, 13]. Figure 4.3 presents experimental synchronization rates as a function of drop sizes (50-200 μm) and oil gaps (10-200 μm) for $\sim$ 100 drop pairs; for these conditions, rates varied by a factor of 30. Excellent fits were obtained between the experimentally measured synchronization rates and the full nonlinear solution of Equation 4.1 if we treated μ_c as a fitting parameter, which varied for each drop size and oil gap. We also fit synchronization rates using the explicitly calculated coupling strength, Equation 4.2. While the functional form of the coupling strength (Equation 4.2) fit the time-dependent synchronization data well for a wide range of oil gaps and drop diameters, the combination of the Turing model (Equation 4.1) with our explicit calculation of the interdrop coupling (Equation 4.2), overestimates the coupling strength by nearly two orders of magnitude. That is, we replaced μ_c of Equation 4.2 with $f\mu_c$, and while theory predicts $f = 1$, experimentally we find $f = 0.0152$. In spite of this discrepancy, the fact that only one phenomenological parameter, f, is needed to reconcile theory and experiment over a wide range of coupling strengths is an improvement over the original Turing model, where a different phenomenological parameter, μ_c, is fitted for each drop diameter and oil gap. As a guide to theorists motivated to improve our calculation of the coupling strength, we note that the Turing model assumes a vanishing thin membrane, while our experimental system has a finite sized oil gap. Our model of coupling strength, based on the assumptions of the Turing model, neglects four factors, each of which reduces coupling: non-uniformity in chemical gradients in the drop and the oil, accumulation of chemicals in the oil, time taken to diffuse across the oil, and chemical reactions within the oil.

Having established the Turing model is quantitatively valid for a wide range of synchronization conditions with a single experimentally determined constant in the coupling term, $f = 0.0152$, we prepared a series of one-dimensional arrays of drops in rings and lines and

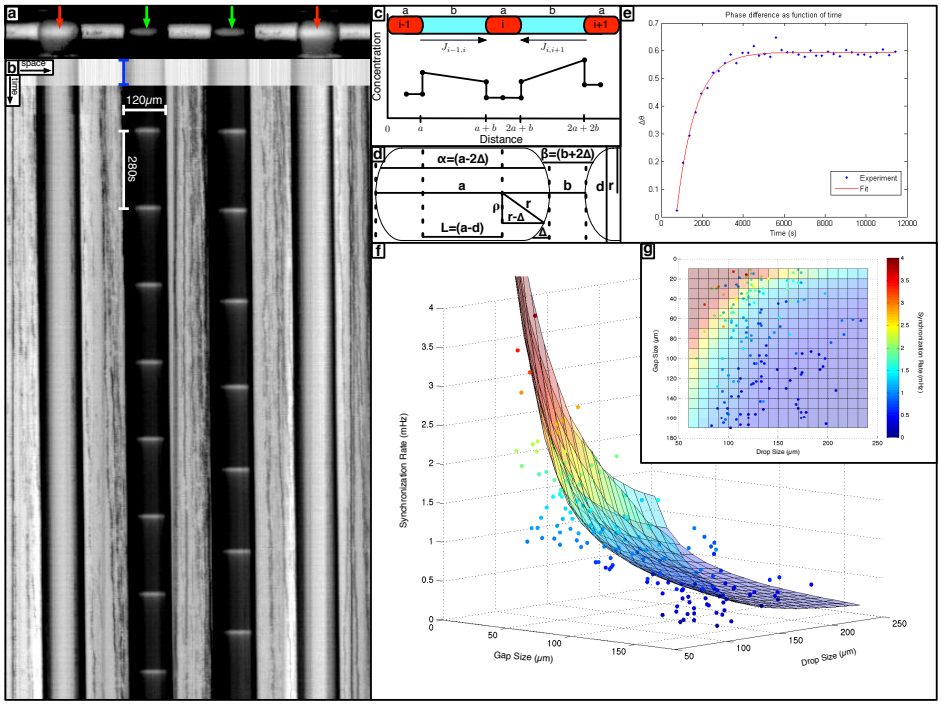

Figure 4.3: Comparison between theory and experiment for the rate of synchronization between two isolated oscillating drops as a function of oil gap and drop size. **a)** An image of four drops in a capillary where red arrows indicate drops inhibited with light and green arrows indicate drops allowed to oscillate. **b)** A space-time plot demonstrating the initial bright pulse synchronizing the drops in phase (blue bar), the constant light holding the outer two drops in the oxidized state, and the phase evolution of the center two drops. Space-time plots were generated by plotting the intensity of a single line of pixels connecting the centers of adjacent drops as a function of time. **c)** A cartoon illustrating the assumptions in deriving Equation 4.2, μ_c. **d)** A schematic illustrating the geometry behind the Derjaguin approximation [39]. The Latin characters (a, b, d, L, r) represent the experimental parameters including the measurements of end-to-end drop width a, end-to-end gap width b, capillary diameter d, and calculated parameters of the linear portion L and radius of curvature r of the spherocylinder. The Greek characters (α, β, Δ, ρ) represent the internal variables of drop width α, gap width β, gap augment Δ, and radial position ρ. **e)** A plot of the phase difference between the center drops from inset (a) fit with an exponential curve from which the measured synchronization rate is extracted. **f)** A 3D plot of the experimental rates plotted against the theoretical synchronization rates calculated for the coupling function μ_c of Equation 4.2 with the drop size and oil gap as independent variables. **g)** A plan-view of the same data as inset (f). Obtaining agreement between the experimentally measured rates (e) and theoretically calculated rates (f,g) requires a scaling factor, $f = 0.0152$ in μ_c. Experimental conditions: 300 mM bromate, 3 mM ferroin, 1.2 mM Rubpy, 80 mM acid, 400 mM MA, 10 mM NaBr, 100μm round capillary, $\sim$100μm drops, and $\sim$105μm gaps. Image adapted from [120].

determined the long term emergent chemical states as a function of the two variables that most strongly control interdrop behavior: malonic acid concentration and coupling strength. Coupling strength, μ_c, is conveniently tuned experimentally by varying the drop size a and oil gap b using microfluidics. In Figure 4.4(a-f) we illustrate examples of six distinct patterns with the symmetry corresponding to Turing cases (*a-f*). Five of the six patterns, Figures 4.4(a,c,d,e,f), appear where predicted by theory in Figure 4.5(b). Four of the six patterns are identified with Turing cases (*c,d,e,f*). The fifth pattern has the same symmetry as Turing case (*a*). However, this pattern is predicted be a stationary, stable state for malonic acid concentrations below 1 mM and therefore does not arise from a Turing instability, underscoring the point that observation of a chemical state with a pattern corresponding to a Turing instability is insufficient evidence to prove the state arises from a Turing mechanism [48, 64, 68, 73]. Notably, the pattern with the symmetry of Turing case (*b*) is observed in a region of parameter space not predicted by theory. This is the sole discrepancy between theory and experiment, and we suspect that it reflects a shortcoming of the VE model. See the Discussion for expanded analysis of each case and of the spatial-temporal patterns.

The behavior of finite rings depends on the number of drops, N, in the ring as seen in Figures 4.4(g, h) for two rings with identical chemical composition, drop size and spacing, but with 5 and 6 drops, respectively. For these particular chemical conditions and for N even, LSA predicts anti-phase oscillations, corresponding to Turing instability (*f*) characterized by the wavevector-frequency pair $(q_{\max}, \omega)$, as defined previously. Turing's prediction is that for N odd, no two drops will undergo an oxidation transition simultaneously; there will be N beats per measure, while for N even there will be two beats per measure. For a ring of five drops, LSA predicts a waveform $C_5(r,t) \propto \exp(i(4\pi r/5 - \omega t))$, with $r \in (0,1,2,3,4)$ the drop number. In this expression, the phase is chosen such that a drop is oxidized when $4\pi r/5 - \omega t$ is equal to a multiple of 2π. As time advances in increments of one fifth of a

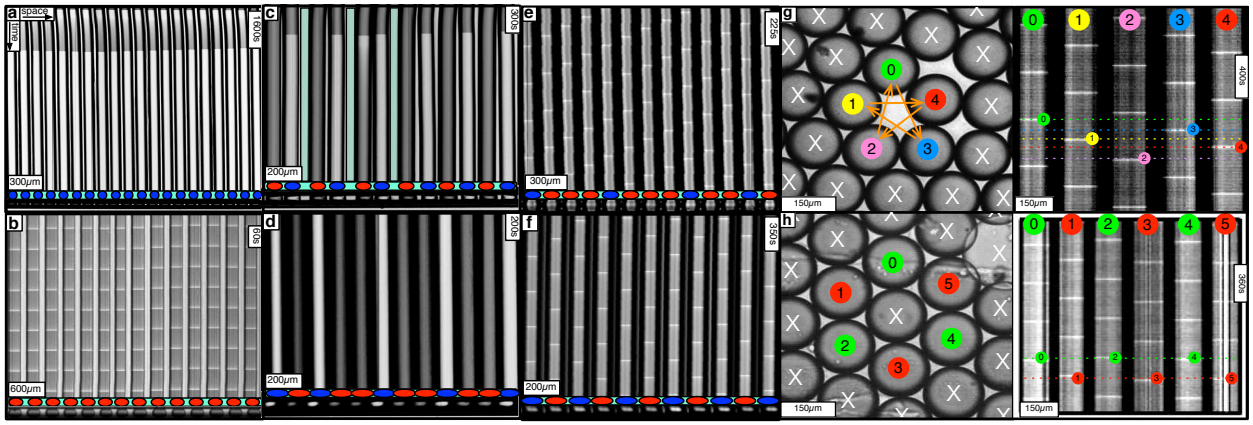

Figure 4.4: Chemical states of linear and circular arrays of BZ drops. (a-f) Cylindrical capillaries of 100 μm inner diameter filled with a linear array of closely spaced droplets. Top: space-time plots demonstrating the corresponding Turing case (*a-f*) were generated by plotting the intensity of a single line of pixels connecting the centers of adjacent drops as a function of time. Bottom: cartoon above corresponding photograph of droplets. Cartoon colors: Blue, BZ drops in oxidized state; Red, reduced state; Cyan, oil. Chemical conditions: 300 mM bromate, 3 mM ferroin, 0.4 mM Rubpy, and 80 mM sulfuric acid. Malonic acid (MA), NaBr, drop size and spacing specified in each case. Five of the six Turing solutions *b-f* are observed. (a) Stationary stable oxidized state after initial transient; 10 mM MA, no NaBr, drop size 130μm, and oil gap 20μm. (b) Turing case *b*, (long-wavelength, oscillatory), ($q_{\min}$, ω); 2.4M MA, 10 mM NaBr, drop size ~230μm, and oil gap ~100μm. (c) Turing case *c*, (short-wavelength, stationary), ($q_{\max}$, 0); 20 mM MA, no NaBr, drop size ~98μm, and variable oil gap between 0μm and 47μm. (d) Turing case *d*, (intermediate-wavelength, stationary), (q, 0); 40 mM MA, no NaBr, drop size 95μm, and oil gap ~0μm (touching drops). (e) Turing case *e*, (intermediate-wavelength, oscillatory), (q, ω); 640 mM MA, 10 mM NaBr, drop size 117μm, and oil gap 3μm. (f) Turing case *f*, (short-wavelength, oscillatory), ($q_{\max}$, ω); 380 mM MA, 10 mM NaBr, drop size 106μm, and oil gap 25μm. (g-h) Odd and even circular arrays. Turing case *f*. Rectangular capillaries with cross-section 0.1 mm x 2 mm filled with a two-dimensional array of close packed droplets from which rings are created with optical isolation. Left: oscillatory drops are labelled; all other drops are illuminated with light (cross) and held non-oscillatory in the reduced state, Right: space-time plot. Chemical conditions: 300 mM bromate, 3 mM ferroin, 80 mM sulfuric acid, 10 mM NaBr, 0.4 mM Rubpy, 640 mM MA, and drop size is ~150μm. (g) Five membered ring. Drops oscillate in a pentagramal pattern. (h) Six membered ring. Neighboring drops are π radians out-of-phase. Image adapted from [120].

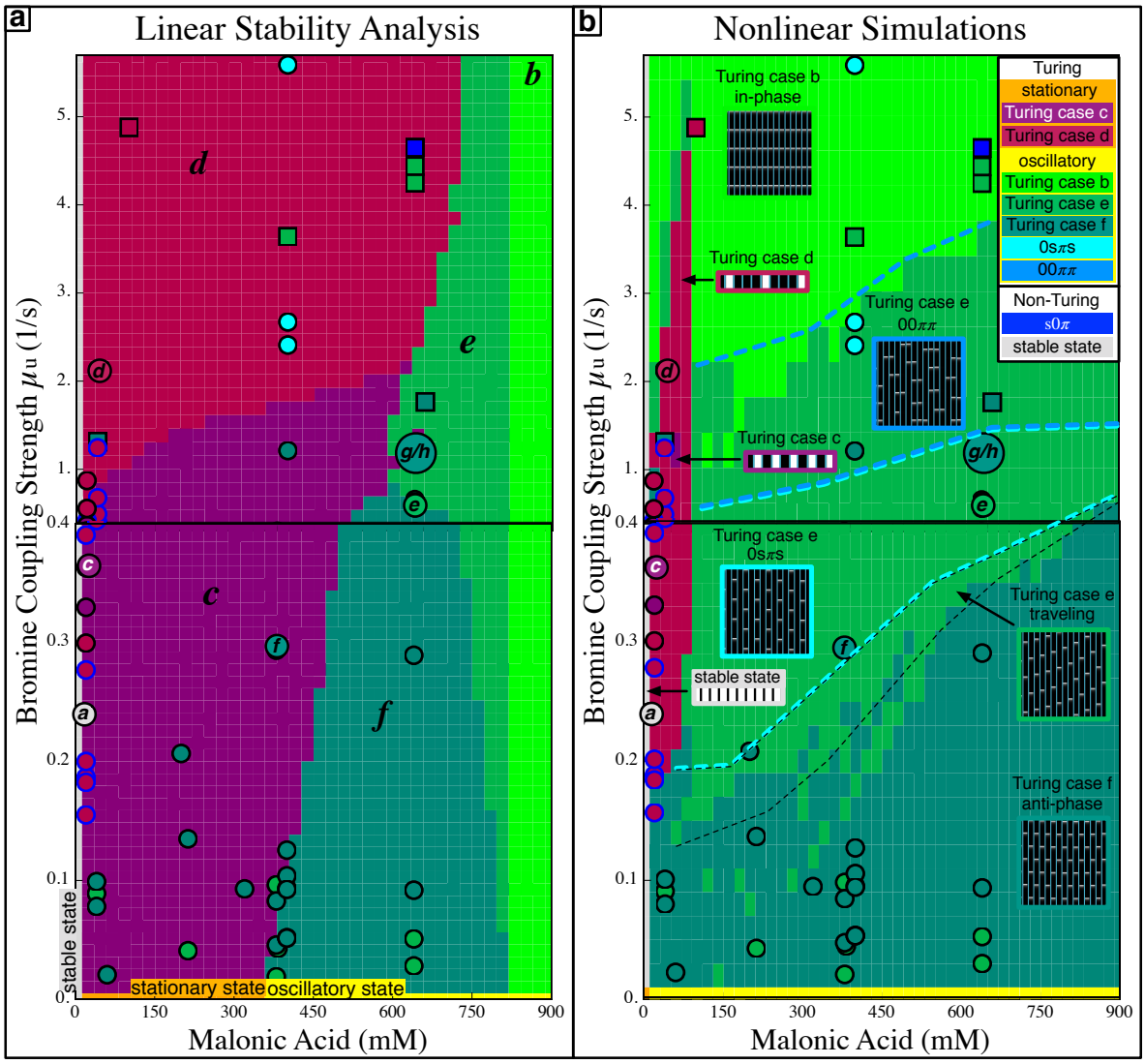

Figure 4.5: Linear stability analysis (LSA) and nonlinear simulations (NLS) of the Vanag-Epstein BZ model, as a function of bromine coupling strength, μ_u, and malonic acid concentration. Note the scale change on the vertical axis at $\mu_u = 0.4$. In both figures red hues represent stationary states and green hues oscillatory states. The data are plotted with circles for 1D experiments and squares for 2D experiments. Red disks outlined in blue indicate a transient initial cluster state settling into a stationary Turing instability. The data points with a letter in the center are included in Figure 4.4. Space-time plots of oscillatory states are inset in square areas; stationary states are inset in rectangular areas. The dashed boundaries within the region of Turing case (e) of the NLS diagram indicates location of traveling waves, the 0sπs state (Figure 4.10), and the 00ππ cluster state. All experimental data points are plotted according to the definitions of μ given in the text with $f = 0.14$. Image adapted from [120].

period, the oxidized state in Figure 4.4g moves along the ring in a pentagramal sequence from drops $0 \rightarrow 3 \rightarrow 1 \rightarrow 4 \rightarrow 2$. For the ring of 6 drops, $C_6(r,t) \propto \exp(i(\pi r - \omega t))$, with $r \in (0,1,2,3,4,5)$. As shown in Figure 4.4h, all even numbered drops oxidize simultaneously at the beginning of a period, and half a period later all odd numbered drops oxidize. In Figure 4.9 we present the LSA predictions for rings with three, four, five, and six drops and the corresponding experiments. For rings of drops, Turing's LSA theory and our experiments are in complete agreement.

Using published chemical rate constants of the VE model [129] (Equation D.1 and Table 4.2) we calculate two state diagrams, one using Turing's linear stability analysis (LSA) and the other the full nonlinear simulation (NLS) of Equations 4.1 in one dimension, shown in Figure 4.5. These theory plots have no adjustable parameters, as the Turing model treats the coupling strength, μ_c, as an independent variable. However, in order to assign coupling strengths to experiment, we explicitly calculate coupling strength using Equation 4.2 to which we introduce a fitting parameter by replacing μ_c of Equation 4.2 with $f\mu_c$. We also fit the partition coefficient of the activator, P_x. The best agreement between the NLS and experiment was obtained for $P_x = 0.05$ and $f = 0.14$. With respect to the experimental state diagram, the NLS overestimates coupling strength 8-fold, which is the same trend as in the case of the synchronization experiments. In experiments and in the NLS at low malonic acid, we find a stable stationary state in which all the drops are in-phase. This has the same pattern as Turing state (a), but as noted previously, LSA reveals this state is stable and it cannot be considered a Turing state, which arises from a homogeneous unstable state. Both state diagrams predict that as coupling strength increases above zero the same five Turing instabilities (b-f) appear with three oscillatory (green hues) and two non-oscillatory (red hues). Theory correctly predicted that for low malonic acid concentration, arrays of large drops would oscillate and that arrays of smaller, chemically identical drops, would be

stationary. For 1D arrays of drops in capillaries, the linear and non-linear theories predict the same basic features, with two notable distinctions. First, non-linearity strongly suppresses the stationary states. Second, "cluster" states, distinctive oscillating patterns consistent with Turing case (e) were experimentally sought and observed only after calculations of the nonlinear state diagram indicated their existence; thus the Turing model is predictive. Further specific comparisons are included in the Discussion and Figures 4.8 and 4.10.

To investigate the effect of dimensionality on Turing instabilities, we performed experiments on close-packed hexagonal arrays of drops, reported as squares in Figure 4.5. For conditions intermediate between stationary and oscillatory Turing instabilities, we observed a state, shown in Figure 4.6, that consists of a lattice composed of triangles of drops in which one drop is stationary and the other two oscillate with a phase difference of π, referred to as the $s0\pi$ state [116]. Linear stability analysis requires all drops to share the same temporal behavior, i.e., all stationary, or all oscillatory; thus the $s0\pi$ state cannot arise from a linear instability. However, it could be a nonlinear effect, but extensive numerical exploration of the full nonlinear chemistry using both the Turing and finite element models on ordered hexagonal arrays failed to produce the $s0\pi$ state. The qualitative discrepancy between theory and experiment suggests that a critical element is missing from the Turing model. Therefore, we developed a theoretical model for the $s0\pi$ state, valid in general for systems undergoing a Hopf bifurcation, which requires additional conditions to the Turing model; the drops must be physically or chemically heterogeneous, with two drops that oscillate at a higher frequency than the third and that synchronize out-of-phase when isolated. Our analysis, elaborated in Figure 4.11 and in the Discussion, predicts that as the coupling strength between the two higher frequency oscillating drops and the third is increased, there is a transition to a state in which the third drop is stabilized in the non-oscillatory state, while the other two drops continue to oscillate out-of-phase. We numerically confirmed our theory by introduc-

ing heterogeneity into the Turing and finite element models, which then produced the $s0\pi$ state. Experimentally, heterogeneity in drop frequency is about 5%, which is less than the 20% required by our simplified analytic theory; therefore the $s0\pi$ state bears more scrutiny. Only recently has heterogeneity been considered theoretically in reaction-diffusion networks [9, 69, 78, 139]; ours is the first experimental work to demonstrate the emergence of a new dynamical state caused by a remarkably small amount of heterogeneity. As the mechanism is generic, we expect it to apply to a large class of reaction-diffusion systems. Furthermore, we note that in general, the experimental state diagram for two-dimensional arrays of drops does not map well onto the one-dimensional nonlinear calculation, indicating that dimensionality plays a significant role in pattern selection.

Turing, in *The Chemical Basis of Morphogenesis* argued that in case (d) (Figure 4.4d), identical biological cells chemically differentiate into active and inactive stationary states. He further speculated that an activated gene could catalyze an increase in the concentration of intracellular molecules, thereby driving physical differentiation by increasing the osmotic pressure in that cell, causing it to swell [124]. In Figure 4.7 we demonstrate precisely this sequence of chemical differentiation followed by physical morphogenesis in a hexagonal packing of identical drops prepared in the chemical state of Turing case (d). The drops, produced microfluidically as spheres, are stored in a rectangular capillary and are deformed into cylindrical disks with the same height as the capillary. The intensity of each drop is a monotonic function of the fraction of oxidized BZ catalyst it contains. As shown in Figure 4.7a, the drops are initially homogeneous in chemistry and drop size. After an initial induction time, the drops undergo a transition from this unstable steady state to Turing case (d), in which one out of three drops is in the reduced (dark) state and two out of three are oxidized (bright), shown in Figure 4.7c. This chemical differentiation occurs with the drop size remaining constant. The oxidized drops consume reagents faster than the reduced drops. This

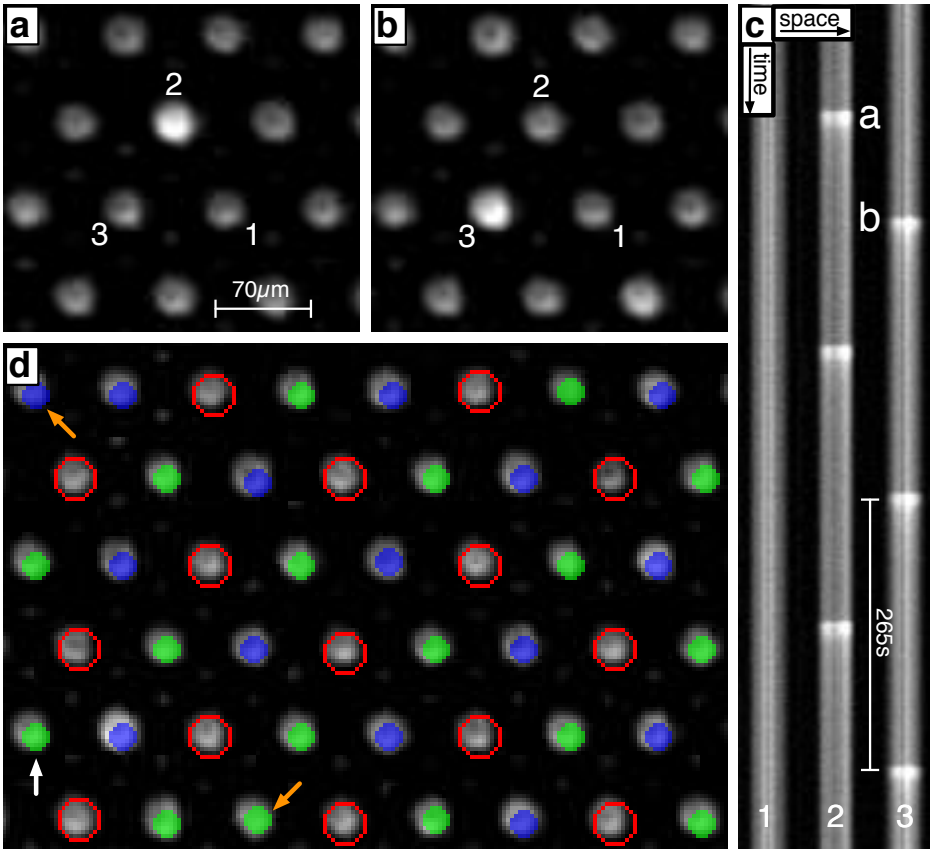

Figure 4.6: Observations of 2D arrays of $s0\pi$ states. a-b) Single frames demonstrating the $s0\pi$ state. The frames correspond to the first two oxidation transitions, labeled a and b in c). c) Space-time plot of drops 1-2-3 shown in a) and b). Drop 1 is stationary, while drops 2-3 remain oscillatory with a phase difference of π. d) A combined image where the stationary drops are outlined in red and the oscillatory drops are color coded by their phase difference, $\phi_i = \theta_i - \theta_{\text{ref}}$, where $0 \leq \phi \leq \pi$ and θ_{ref} is the phase of the drop indicated with the white vertical arrow. Drops where $\phi_i < \pi/2$ are green and $\phi_i > \pi/2$ are blue. Notice that every third drop is stationary and every oscillatory drop is out of phase with its immediate neighbors; two exceptions are noted with orange arrows. Chemical conditions: 300 mM bromate, 3 mM ferroin, 0.4 mM Rubpy, 80 mM acid, 640 mM MA, and 10 mM NaBr. Drop size is $\sim 70\mu$m. Image adapted from [120].

creates an osmotic pressure imbalance, causing water to flow from the oxidized to reduced drops, creating a morphological transformation in which the initially homogeneous cells differentiate into two populations with distinct chemical redox states and physical sizes, as shown in Figure 4.7e. Quantitative measurements of the volume changes are in agreement with theory, as elaborated in the Discussion.

4.5 Discussion

When directly comparing the data from the synchronization rates of two drops and the state diagram measurements with the theoretical predictions, we found that an additional fitting parameter needed to be added for quantitative agreement between theory and experiment. As noted in the caption to Figure 4.3 the coupling strength, μ, must be multiplied by a fitting factor of $f = 0.0152$ for the calculated and measured synchronization rates to match. The LSA and NLS are calculated in an abstract space where we vary the coupling strength μ_c over a range of values, whereas for experiments this is a function of many physical parameters (Equation 4.2) as derived in Appendix C. Similarly to the case of synchronization rates, in order for the state diagram data to match theory (Figure 4.5) the coupling strength μ_c must be multiplied by a fitting factor of $f = 0.14$. Possible physical explanations for this fitting factor are mentioned in the main text. Furthermore, when plotting the data in Figure 4.5 of the main text the drop spacing is augmented such that $b = b + 10$ nm to account for the fact that drops don't coalesce, as they are always separated by a surfactant layer. Finally, when plotting 2D data in Figure 4.5 of the main text, the coupling term μ is multiplied by 3 as a result of the normal mode analysis for closely packed spheres in 2D.

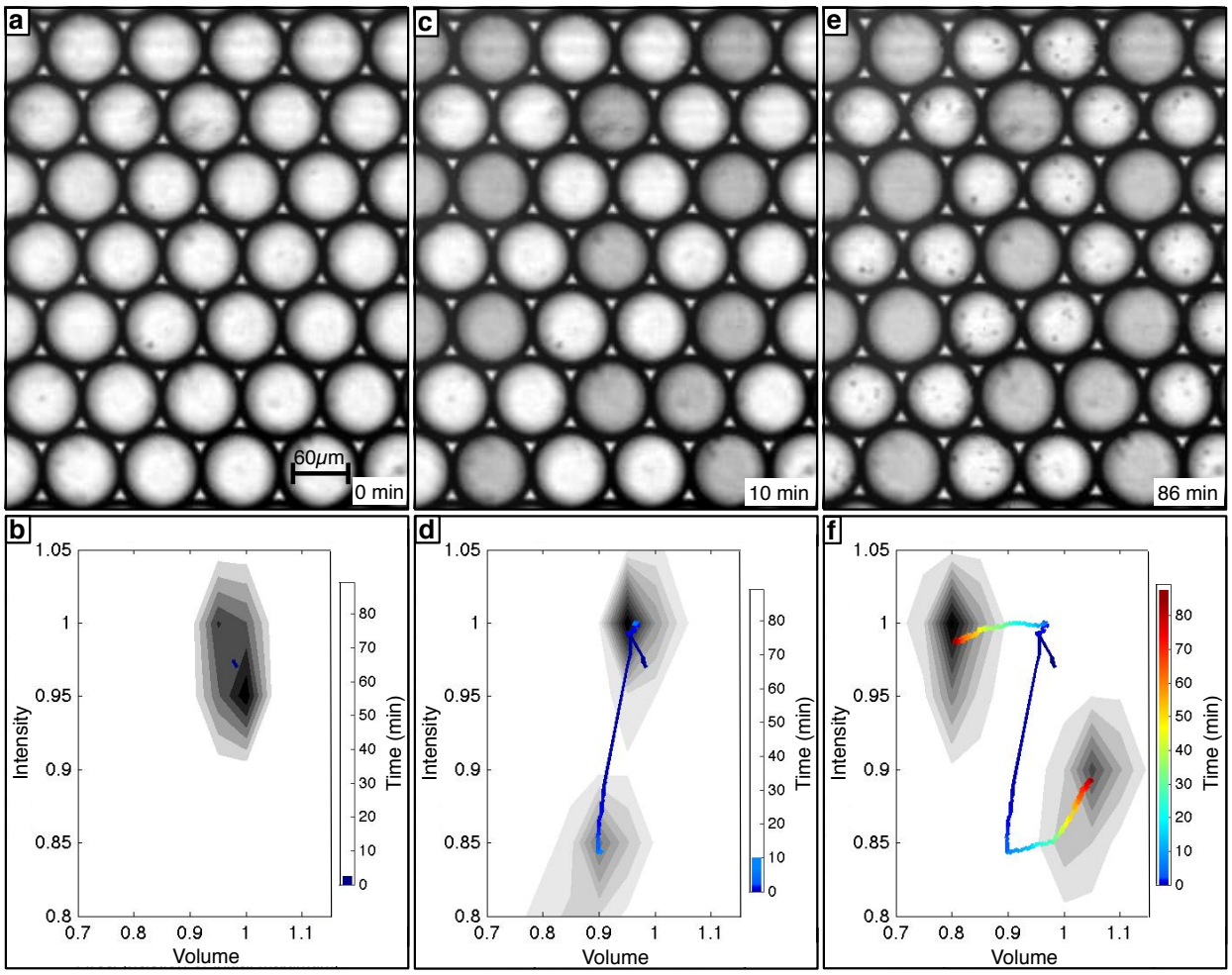

Figure 4.7: Images and histograms of drops demonstrating morphogenesis plotted as fraction of original drop intensity and fraction of original drop volume. Intensity is a function of the chemical state of the BZ catalyst; bright drops are oxidized, dark drops reduced. The color coded line tracks the center of each peak as a function of time. a-b) Initially, drops are homogenous in both intensity, or chemical state, and physical volume. c-d) At intermediate times the drops undergo a Turing bifurcation, becoming heterogeneous in oxidation state, but remaining homogenous in volume, as seen by the differentiation into lighter and darker drops of equal size. e-f) At later times drops are heterogeneous in both oxidation state and volume. The oxidized (bright) drops shrink and reduced (dark) drops swell. Chemical conditions: 200 mM MA, 0.4 mM Rubipy, 0 mM NaBr, 80 mM H_2SO_4, 300 mM $NaBrO_3$, 3 mM Ferroin, 0.05 x 1mm rectangular capillary, initial drop size $\sim 66\mu$m. Image adapted from [120].

4.5.1 Observed States

We observe spatial-temporal patterns in drops arranged in linear rows, which are classified by their dimensionless wavevector, q, and oscillation frequency, ω, using the same nomenclature as Turing. The wavevector, q, has units of phase. Turing classified patterns by arranging the possible values of q into 3 categories; $q = 0$, $0 < q < \pi$, and $q = \pi$. Furthermore, Turing divided the frequency, ω, into 2 categories, $\omega = 0$ and $\omega > 0$. This scheme gives 6 cases in total and we observe patterns with the symmetry of each of these cases, shown in Figure 4.4. However, more than one distinct physical-chemical mechanism can lead to the same pattern; therefore observation of a pattern with the same spatial-temporal structure as a Turing instability does not prove that the pattern arises from the Turing mechanism. In order to identify a pattern as a Turing instability we additionally require that the observed pattern be located in the state diagram of Figure 4.5b as predicted by the full Turing model. Our philosophy is that if two predictions of the model agree with experiment, then the chances of the model being wrong are small. The ideal experiment would be to prepare the system in conditions corresponding to the unstable steady state and measure the chemical concentrations as a function of time. However, we do not have the ability to do this ideal experiment; the best we can do is observe the space-time pattern (Figure 4.4) of the catalyst and the chemical state diagram (Figure 4.5). Additionally, using a light sensitive catalyst, for some set of parameters, we are able to control initial and boundary conditions, which permits careful experimental study of the coupling of two drops (Figure 4.3).

The LSA and NLS calculations predict that at very low malonic acid concentrations there is one steady state, corresponding to the oxidized state, and the steady state is stable. For a 1D array of drops, if all the drops are stationary and in the same state (oxidized) then the wavevector ($q = 0$) and frequency ($\omega = 0$) correspond to the symmetry of Turing case

(a). However, by definition, the state at low malonic acid is not Turing state (a), because all Turing states must arise as an instability from an unstable steady state. Thus, for our system, only 5 of the 6 Turing states are predicted to exist. In experiment, we do observe a stationary, uniform state at low malonic acid, exactly where theory predicts a stable steady-state solution. As experiment and theory agree, we assign this low malonic acid to be the steady-state solution and not Turing state (a). However, for catalyst concentrations of 42 mM, which is ten times the amount used in our experiments, the LSA predicts that instead of the single, stable steady oxidized state found for MA $<$ 1 mM, there are two steady states. One, the oxidized stable steady state and a second unstable steady reduced state with an instability to a non-oscillatory Turing instability corresponding to Turing case (a). Experimentally, when we prepared samples with catalyst concentrations exceeding 24 mM, in 20 mM MA, the samples did not oscillate, even though the VE model predicted they would oscillate. This discrepancy between theory and experiment is unresolved.

Of the remaining five Turing cases (b,c,d,e,f), four of the experimental Turing cases are observed to occur in the regions of the state diagram predicted by the NLS. Turing case (b) is an exception. At the experimental conditions for state (b) shown in Figure 4.4 of the main text (2.4M malonic acid) the nonlinear simulations generate an initial transient state that corresponds to state (b), but that evolves with time into a stable attractor corresponding to Turing case (e). Notably, this evolution from an initial in-phase transient to Turing case (e) is also seen experimentally, but for much lower malonic acid (20 mM) concentration, as shown in Figure 4.2.

In summary, patterns with the same appearance as the six Turing cases (a-f) are observed as illustrated in Figure 4.4. Five of the six patterns, Figures 4.4(a,c,d,e,f), appear where predicted by theory. Four of the six patterns are identified with Turing cases (c,d,e,f). Turing case (a) does not occur for the parameters accessible to our experimental system.

However, at low malonic acid, we do observe a pattern with the same symmetry as Turing state (a), which the Turing model predicts to be a stable steady state. Only the pattern with the symmetry of Turing case (b), shown in Figure 4.4(b) is observed in a region of parameter space not predicted by theory.

The linear stability analysis unambiguously reveals the stability of the steady state and the eigenvalue of the instability for each chemical condition. The nonlinear simulations and experiments are more difficult to analyze, as the initial, linear response of the experimental system produces too small a signal to be detected with our instrumentation. In experiment, we observe dynamics when the chemical amplitudes are large and therefore nonlinear. Identification of the Turing state is done using space-time data, which creates several difficulties. First, the drops are a closed chemical system. With time the malonic acid is consumed, but the coupling strength remains the same. In terms of the state diagram shown in Figure 4.5, this means that conditions initiate from a starting point on the right of the figure, and with time evolve horizontally to the left. Second, the Turing states are dynamical attractors, but, in general, initial conditions of the NLS and experiments are different from the attractor, so that there is an initial transient period before the system settles in on an attractor. Third, wavelength selection is broad. This means that more than one wavelength will be selected, which leads to creation of defects in the patterns, complicating identification of states.

Four of the Turing states are straightforward to recognize and categorize, as they have finite wavelengths; these correspond to Turing states (c) and (d) (stationary with wavelengths of $\lambda = 2$ drops or $2 < \lambda < \infty$) and Turing states (e) and (f) (oscillatory with wavelengths of 2 drops $< \lambda < \infty$ or $\lambda = 2$ drops). The remaining two states ((a) and (b)) are more difficult to identify due to ambiguities and possible secondary mechanisms. In simulations, oscillations with nearest neighbors in-phase with each other are seen both as a final state (Turing state (b)) and as a transient response evolving to a finite-phase oscillatory state with nearest

neighbors not in-phase (Turing state (e)). This makes it difficult to classify in experiments whether what is seen is an adiabatic transition from a quasi-stable in-phase attractor to the finite-phase attractor due to decaying malonic acid concentration, or an in-phase transient transforming to the finite-phase attractor. Experiments from high malonic acid concentrations (2.4M, Figure 4.4b in the main text) demonstrate long periods of in-phase oscillations, lending support for transitions due to malonic acid decay rather than initial transients. In general, if a system stays in one state for 10 periods, we consider this to be a stable attractor and not transient behavior resulting from initial conditions. Similarly, in simulations and experiments the in-phase stationary state is seen, but it is impossible to determine by the space-time data alone if this is due to the Turing mechanism or an underlying stability of the steady state. In Figure 4.8 we observe a transition from the finite-phase stationary state to the in-phase stationary state. Because the theory predicts a stable steady state at low malonic acid, we conclude that experiment is consistent with theory and that what we observe is a steady state and not Turing state (a). Thus, while we present data and simulations that demonstrate the phenomenology of Turing state (a), it is the one state that we can not classify as due to the Turing mechanism.

We repeated the experiments many times to average over transients. We also made samples with slightly different droplet diameters and spacings at constant chemical concentrations, and conversely, samples with the same droplet dimensions, but with slightly different chemical concentrations. In this way we traversed the state diagram in Figure 4.5b along vertical and horizontal trajectories. We compared the initial behavior of samples with slightly different malonic acid concentrations, say 40 mM, 30 mM and 20 mM, with a single sample of 40 mM malonic as a function of time. The hypothesis is that the sample that initially started at 40 mM malonic acid would over long times lower its concentration from 40 mM to 30 mM and 20 mM and thus over time generate the states exhibited by fresh

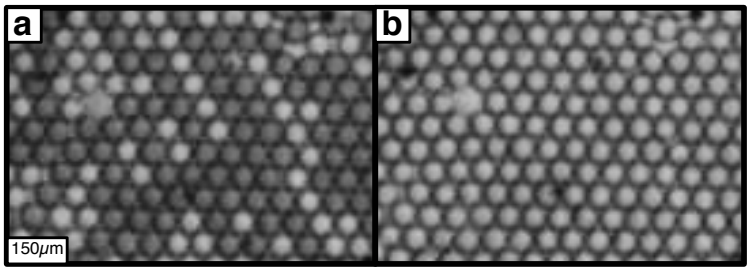

Figure 4.8: Transitions between states due to the consumption of malonic acid. The malonic acid concentration of a closed reaction decreases with time such that the system evolves along horizontal trajectories proceeding from right to left in Figure 4.5 and can undergo a transition from one Turing instability to another. The initial chemical conditions are 80 mM H_2SO_4, 300 mM $NaBrO_3$, 40 mM MA, 3 mM ferroin, no Rubpy, and no NaBr. Drop size $\sim$50μm and oil gap $\sim$0μm (touching) corresponding to $\mu = 1$ in a wide flat 2D capillary. **a)** Image of the system at an early time, which corresponds to Turing case (d), or (finite wavevector, stationary) denoted as $(q, 0)$. With MA $\sim$40 mM and $\mu = 1$ the numerical simulations of Figure 4.5 also predicts Turing case (d). **b)** Image of the system two hours after (a), which corresponds to a uniform state (or Turing case (a), or (zero wavevector, stationary) denoted as (0,0). The numerical simulations of Figure 4.5 in the main text predict a *stable* stationary (0,0) state at $\mu = 1$ for MA<10 mM. Image adapted from [120].

samples that initially had different malonic acid concentrations. Only after a series of such experiments produced consistent results did we ascribe a Turing state to a particular region of the parameter space in Figure 4.5b.

4.5.2 Finite Rings

An important facet to note is that the behavior of finite rings with a small number of oscillators depends on both the chemical conditions and the number of drops in the ring, as seen in Figure 4.4 of the main text and Figure 4.9. In a ring with an infinite number of drops, Linear Stability Analysis allows continuous values of q and associated wavelength ($\lambda = 2\pi/q$); thus the dominant mode is simply the q at which the real component of the eigenvalue is maximal. However, for finite rings the wavelength is limited by the requirement of periodicity

such that $q = 2\pi s/N$ for $s = [0, s_{\max}]$ where for even numbered rings $s_{\max} = N/2$ and for odd rings $s_{\max} = (N-1)/2$, as the phase differences between nearest neighbors around the ring must add up to an integer multiple of 2π. This yields the result that for chemical conditions where the real component of the eigenvalue is maximal at $q = \pi$ there will be a different state for rings where N is even or odd, as $q = \pi$ is not an available solution when N is odd. In Figure 4.9 we can see the predicted behaviour for rings with three, four, five, and six drops and the corresponding experiments. In these situations the linear stability predictions of the Turing theory and experiments are in complete agreement.

4.5.3 0sπs and 00$\pi\pi$ States

Another two states observed in simulations and experiments are what we refer to as the "0sπs" state and "00$\pi\pi$" cluster state (as seen in Figure 4.5). The 0sπs state is a 1D state with a wavelength of four drops, of which the first and third drops are anti-phase, while the second and fourth drops are stationary. The name 0sπs is simply a sequential observational naming scheme of zero phase, stationary, π phase, stationary. Examples of this state are shown in Figure 4.10. From a linear stability point of view this state would correspond to an oscillatory state with a wavelength of four drops, the same as a traveling wave; therefore this state satisfies the normal mode solutions from Turing with nodes of zero amplitude located on the second and fourth drops, Turing state (e). Similarly, the 00$\pi\pi$ state has a period of four drops. However, all drops oscillate; the first two drops are in-phase and the next two drops are anti-phase. These two states were seen in simulations before any experiments were done at the conditions at which the simulations identified the states. Subsequently, experiments found the state as predicted.

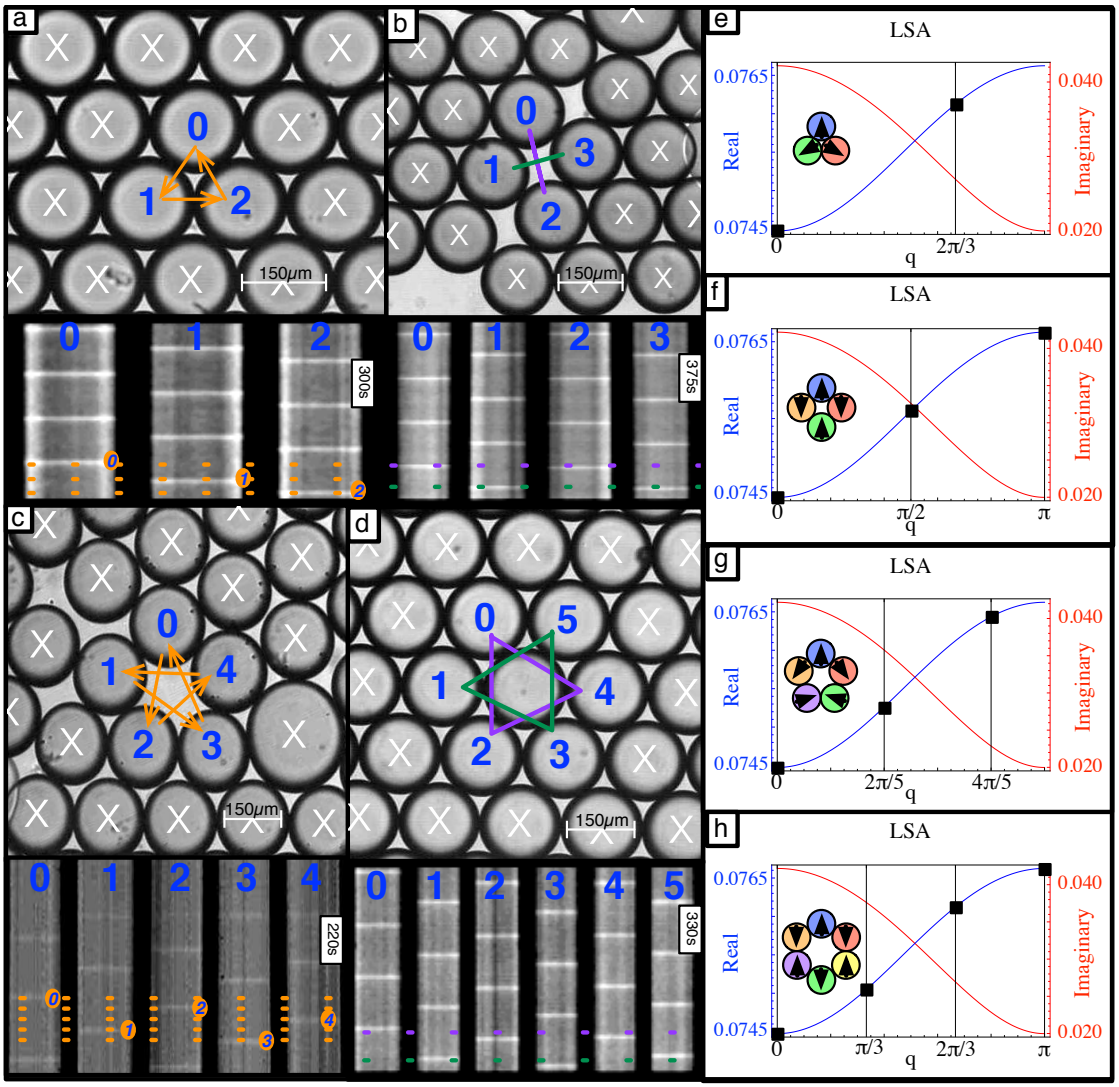

Figure 4.9: Comparison between theory and experiment for rings of 3, 4, 5 and 6 drops. **a-d)** Photo isolated rings of BZ drops with space-time plots to indicate order of oscillation. **e-h)** LSA predictions for finite rings with allowable states indicated with squares. Allowable wavenumbers correspond to $q{=}2\pi s/N$ where the integer s ranges from 0 to $s_{\max}$, where for even numbered rings $s_{\max} = N/2$ and for odd rings $s_{\max} = (N-1)/2$. The wavevector with the largest real value grows the fastest. All the wave vectors are imaginary and therefore oscillate. Conditions as shown in Table 4.1 for Turing instability *f*. See the Discussion for details on the LSA plots. Image adapted from [120].

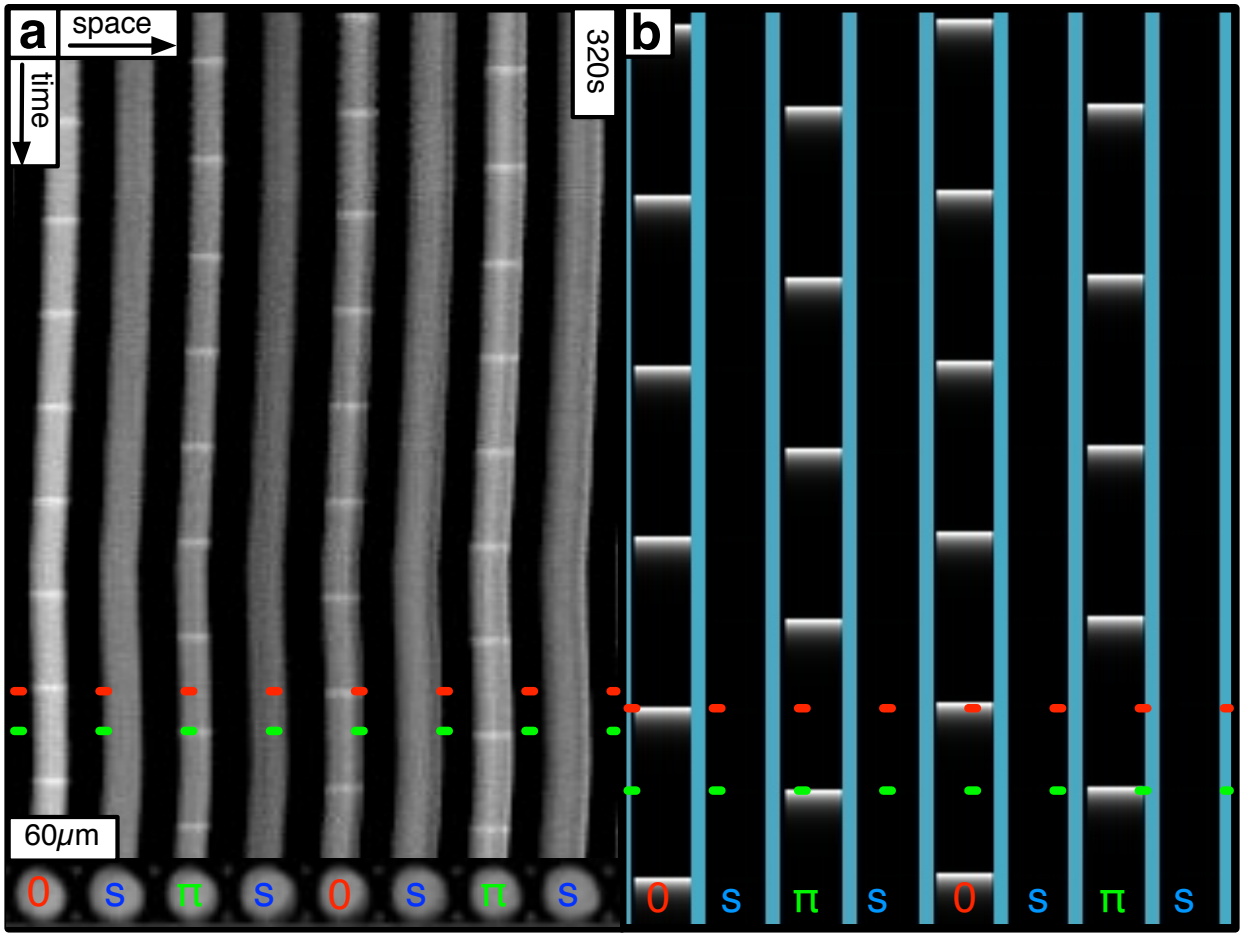

Figure 4.10: Example of the 0sπs state in experiment and simulation. Red and green dashed lines are meant to guide the eye for the phase differences between oscillatory drops. **a)** Experimental data demonstrating the 0sπs state. Experimental conditions: 400 mM malonic acid, 80 mM sulfuric acid, 300 mM bromate, 10 mM bromide, 3 mM ferroin, 1.2 mM rubpy, ∼50μm drop size, and ∼3μm spacing. **b)** Numerical simulations demonstrating the 0sπs state. Simulation conditions: m = 400 mM MA, h = 160 mM H^+, A = 300 mM bromate, c_0 = 4.2 mM catalyst, a = 50μm drops, b = 50μm gap, P_u = 2.5, and P_x = 0.05. Image adapted from [120].

4.5.4 Malonic Acid Decay

A key difference between the VE model and experiments is malonic acid decay. The VE model is based on an open BZ reaction system where the reactors are continuously fed new reactants and products are continuously removed the feed chemicals can be treated as constant. The experimental emulsion system is a closed BZ reaction where the reactants are consumed and thus the chemical parameters change with time. Consequently, the malonic acid concentration will decay with time. This allows for a single experiment to probe the state transitions that occur when the malonic acid concentration crosses the border between two predicted patterns as seen in Figure 4.8. The transitions observed are in agreement with the simulations based on the VE model as seen in Figure 4.5 of the main text and are thus seen as additional confirmation that the underlying mechanism is indeed that described by Turing. We note that the bromate also decays in time, but since it's larger than the malonic acid concentration (and the state behavior is less sensitive to it), this effect can be neglected.

4.5.5 Stabilization of the $s0\pi$ State

The $s0\pi$ state is observed in 2D hexagonal closed-packed lattices of BZ drops in the part of the state diagram shown in Figure 4.5 intermediate between the Turing state (d) of stationary drops and Turing state (e) of oscillatory drops. It consists of a mixed oscillatory and stationary state in which 3 drops, arranged in a triangle, exhibited the following behavior; one drop was stationary, s, in a reduced, near stable steady state and the other two oscillated π radians out of phase.

Considerable effort was spent trying to find parameters in numerical simulations in ordered, hexagonal arrays of drops that demonstrated the $s0\pi$ state without the addition of heterogeneity, using both point models in Matlab and full finite element simulations in

COMSOL. All of these efforts proved futile, even with the inclusion of the ∼5% chemical and physical heterogeneity measured in experiments. For example, when we simulated a ring of three identical drops we observed three different states as a function of coupling strength. At low coupling strength, all three drops oscillated with a relative phase shift of $2\pi/3$. At higher coupling strength, all drops continued to oscillate, but 2 drops had a relative phase shift of 0 and the third drop had a phase shift of π. At still higher coupling strength, the three drops stopped oscillating simultaneously. Only with the inclusion of exaggerated heterogeneity of ∼20% in either chemistry or geometry is the $s0\pi$ state realized in simulations. In simulations, we have not yet explored the effect of lattice disorder on the state behavior, and at this point our understanding of the state is incomplete. For our current best understanding of the state from a purely mathematical perspective see [120].

4.5.6 Morphogenesis

The experiments for this section are illustrated in Figure 4.7. Consider the net reaction in the FKN [84] model of the BZ reaction:

$$3BrO_3^- + 5CH_2(COOH)_2 + 3H^+ \rightarrow 3BrCH(COOH)_2 + 2HCOOH + 4CO_2 + 5H_2O \quad (4.3)$$

We assume that this is the major reaction that takes place in going from the reduced to the oxidized state. With the initial concentrations used, we have to take into account the counterions (every BrO_3^- comes with an Na^+, H^+ comes from H_2SO_4) and assuming the sulfuric acid starts off as $H^+ + HSO_4^-$, but HSO_4^- dissociates to $H^+ + SO_4^{2-}$ when the reaction consumes H^+. The limiting reactant is the MA. If the reaction goes to completion in the oxidized state, all the MA is consumed. We assume that essentially all the CO_2 partitions out of the drops. The initial and final concentrations are shown in Table 4.3.

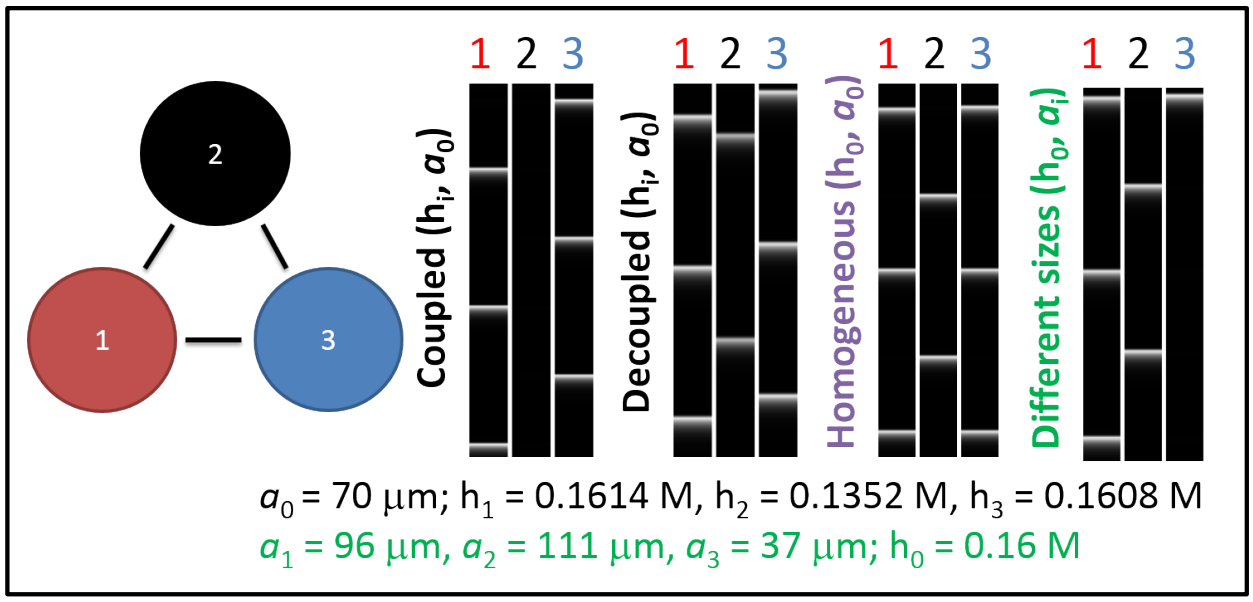

Figure 4.11: In simulation the $s0\pi$ state is only seen in the presence of small chemical or physical heterogeneities. A point oscillator VE model simulation for three BZ drops using periodic boundary conditions and random initial conditions close to the steady state. Parameters: P_x=0.05, P_u=2.5, a=70μm, b=0μm, h_i=$\left[H^+\right]_i$ for i=1,2,3, m=640 mM, A=300 mM, c_0=3 mM. The simulated space time plots indicate that when coupled the system with small chemical heterogeneity forms the $s0\pi$ state, when decoupled (P_x=P_u=0) all three drops are oscillatory, and without chemical heterogeneity forms an anti-phase pattern. The $s0\pi$ state was also observed in systems with physical heterogeneity. Image adapted from [120].

Table 4.3: Chemical concentrations for morphogenesis experiments. The initial and final concentrations of the chemical species are indicated along with the net molarity within the drops.

Species	Initial conc. [mM]	Final conc. [mM]
Na^+	300	300
BrO_3^-	300	180
MA	200	0
H^+	80	40
HSO_4^-	80	0
SO_4^{2-}	0	80
BrMA	0	120
HCOOH	0	80
Total	960	800

If we further assume that the drops in the reduced state consume no malonic acid and the drops in the oxidized state go to completion, then this calculation shows that the maximum difference in molarity is 17% between a reduced and oxidized drop. This difference in molarity will drive a flux of water between the drops until the molarity of the drops is equal. In the experiment, roughly two-thirds of the drops are oxidized and one-third reduced. This leads to the prediction that the oxidized drops shrink by 6% in volume and the reduced drops swell by 12% in volume. The drops have a measured diameter of $\sim$ 60 μm and they are confined in a rectangular capillary of 50 μm height. Assuming the drops are spheres leads to the prediction that the ratio of the radii of the swollen (reduced) to shrunken (oxidized) drops is 1.06, while assuming the drops are highly confined in height to be approximated as disks, the ratio of radii becomes 1.09. The measured ratio is 1.1, consistent with the crude estimates given above. Additionally, we can think of no other plausible mechanism to account for the change in size of the drops besides osmotic pressure. The combination of the reasonable physical mechanism and agreement between quantitative prediction and measurement leads us to conclude that osmosis drives the shape change, as speculated by Turing.

4.6 Conclusion

Turing's model predicts the circumstances under which initially homogeneous diffusively coupled cells will spontaneously evolve spatio-temporal chemical structures. However, only a small subset of chemical reactions lead to the Turing instabilities; most reactions remain stably homogeneous. In emulsions of the oscillatory Belousov-Zhabotinsky chemical reaction, tuning coupling strength and chemical dynamics by changing drop size and malonic acid concentration, respectively, reveals seven distinct chemical structures, six of which were

predicted by theory. Turing's model eliminates the oil phase separating cells and treats the coupling strength as a free parameter. We extended Turing's model to explicitly calculate the coupling strength. Experiments revealed that the extended model overestimated intercellular coupling by nearly two orders of magnitude. One experimentally determined parameter was introduced to reconcile theory and experiment for a wide range of conditions; eliminating this one phenomenological parameter remains a theoretical challenge. Linear stability analysis of the Turing model captures most of the qualitative features of the observed chemical pattern formation; thereby providing a mechanistic explanation of pattern selection. However, the full nonlinear model must be solved in order to achieve quantitative agreement between experiment and theory. We observe one chemical pattern inconsistent with the original Turing model and propose a generic mechanism whereby slight heterogeneity in the cells leads to a new state of mixed dynamical and stationary character. The Turing model is regarded as a metaphor for morphogenesis in biology; useful for a conceptual framework and to guide modeling, but not for prediction [92]. In contrast, in this chemical system, we demonstrated that the Turing model quantitatively explains "materials morphogenesis" in which cellular compartments first chemically and then physically differentiate, raising the possibility of exploiting this form of reaction-diffusion chemistry for materials science applications.

Chapter 5

Development of Methods for the Creation of Custom Planar Networks

This chapter is adapted from [118] which is under review for publication at the journal *Chaos*.

Abstract

Methods for creating custom planar networks of coupled chemical oscillators and perturbing individual oscillators within the network are presented. The oscillators consist of the Belousov-Zhabotinsky (BZ) reaction contained in an emulsion. Networks of drops of the BZ reaction are created with either Dirichlet (constant-concentration) or Neumann (no-flux) boundary conditions in a custom planar configuration using programmable illumination for the perturbations. The differences between the observed network dynamics for each boundary condition are described. Using light, we demonstrate the ability to control the initial conditions of the network and to cause individual oscillators within the network to undergo sustained period elongation or a one-time phase delay.

The spontaneous synchronization of coupled oscillators has a long history starting from Christiaan Huygens' observation of pendulum clocks [82, 91] and has natural manifestations ranging from heart beats and circadian rhythms within single organisms [136] to the synchronized flashing of fireflies and locking of human footsteps in groups of organisms [109]. Numerous review articles have been written [108, 137, 2, 6, 5] and several textbooks have been published [91, 107, 53, 42, 69], yet relatively few experimental systems exist to empirically test synchronization behavior. Those experimental systems that do exist, such as arrays of nickel electrodes [47, 46, 50, 96, 97, 132, 133], transistors [70], metronomes [89, 66], and the Belousov-Zhabotinsky (BZ) reaction with coupled reactors [65, 111, 55], catalyst beads [112, 115, 114], in PDMS arrays [86, 72], or in an emulsion environment [117, 116, 13, 120], are either limited in their ability to control the network structure, boundary conditions, or the nature of the coupling between oscillators, or rely on electrical wiring. In this paper we present methods of creating custom planar networks of inhibitory coupled oscillators using a BZ emulsion, demonstrate the ability to control boundary and initial conditions, and perturb individual oscillators within the network using externally applied light. Such technology enables synchronization engineering [46, 86, 72, 18, 17] of networks of nonlinear chemical oscillators for applications in fields such as soft robotics [37, 45, 122].

5.1 Introduction

The aims of this paper are to present methods for the creation of custom planar networks of diffusively coupled chemical oscillators based on the Belousov-Zhabotinsky (BZ) chemical reaction, methods to control boundary and initial conditions, and the ability to perturb individual oscillators within the network using externally applied light. The BZ reaction [135] has a rich history of experimental and theoretical study [32, 26, 123, 144, 125, 129, 84, 25, 31, 33, 34]

and consequently, is well understood chemically. One BZ based network involves loading the catalyst onto beads which are then immersed into a catalyst-free BZ mixture [112, 115, 114]. The BZ-beads system has recently been used to demonstrate the existence of chimera states [1, 114], but it is limited in its ability to define custom network geometries and to separate the rates of inhibitory and activation coupling. Another approach to BZ based networks consists of a periodic array of the BZ catalyst immersed in catalyst-free BZ solution, which was used to test adaptive optical coupling and therefore intentionally minimized diffusive coupling [86, 72]. Under those circumstances, maintenance of dynamical attractor states required external application of light. Likewise the BZ-bead system has been used to test adaptive optical coupling with externally applied light [44]. In contrast, coupling in our studies is entirely diffusive and dynamical attractors are autonomous. Previously, we developed a BZ based network in an emulsion environment consisting of monodisperse drops of aqueous BZ immersed in a continuous oil phase [117, 116, 13, 120]. The BZ solution contains polar and apolar species, but only the apolar species partition into the intervening oil. The predominant apolar species is an inhibitor, which produces two notable consequences. First, inhibitory coupling leads pairs of coupled drops to synchronize out-of-phase. Second, the BZ emulsion system is suitable for testing Turing's theory of morphogenesis because the interdrop transport rate of the inhibitor is much greater than the activator rate [124, 120]. However, the emulsion system also suffered from limited abilities to define custom network geometries and control boundary conditions; two issues which are addressed here.

Section 5.2 describes the ability to create planar networks with Dirichlet (constant-concentration) boundary conditions using optical isolation, or with Neumann (no-flux) boundary conditions using physical isolation, and examines the effects of the boundary conditions on the network patterns by comparing different implementations of the same network. In Section 5.3, the ability to perturb individual oscillators within the network is demonstrated

by setting the initial conditions of the oscillators and by measuring the light induced period elongation and phase response curve to light of individual oscillators. Section 5.4 concludes by describing how this work builds towards synchronization engineering of the BZ emulsion and lays out future research goals. Appendix E further elucidates creating the BZ emulsion, the steps involved in creating devices that hold BZ drops with various boundary conditions, and using those functional devices in a programmable illumination microscope.

5.2 Network Creation

5.2.1 Optical Isolation/Dirichlet Boundary Conditions

Beginning with a planar, close-packed emulson of BZ drops confined between two glass walls, networks with constant-concentration boundary conditions are created by optically isolating a subset of the drops. Optically defined networks utilize the optical inhibition properties of tris(bipyridine)ruthenium(II) (Rubpy) catalyzed BZ [31, 121] and the Programmable Illumination Microscope (PIM) [119]. The PIM is a tool developed for maskless-photolithography [41, 75], optogenetics [105], and nonlinear dynamics [120]. Here the PIM is used to track and illuminate individual drops for network creation.

In Figure 5.1 we show the optical inhibition and network creation properties of the PIM/BZ system for the simplest networks of 1 and 2 drops. Figure 5.1(a) demonstrates a single isolated oscillator. The image shows the inhibitory light projected on all but one drop (marked in red) within the field of view. Intensity traces of the uninhibited drop and a representative inhibited drop (marked in cyan) are shown in Figure 5.1(b). The uninhibited drop (red trace) clearly oscillates while the inhibited drop (cyan trace) does not. This behavior is readily reproducible for any configuration of inhibited and uninhibited drops

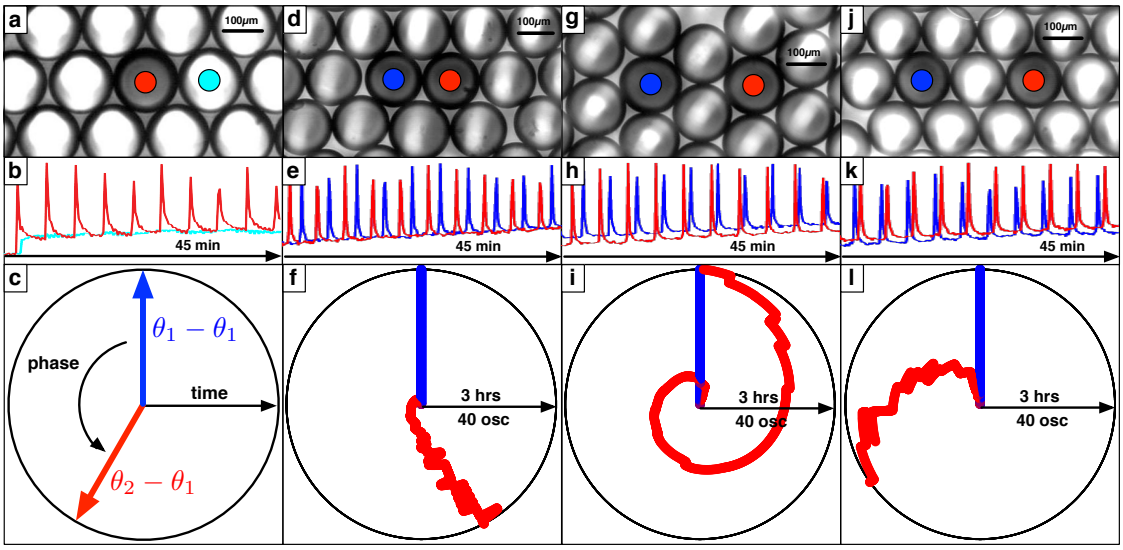

Figure 5.1: Optical isolation of single drops and pairs of drops. **a**) A single optically isolated drop with **b**) intensity traces. **c**) The schematic of a radial-phase-time plot. **d**) An oscillating pair of nearest neighbor drops with **e**) intensity traces color coded as in panel (d). **f**) A radial-phase-time plot of the pair of drops shown in panel (d). **g**) An oscillating pair of diagonally neighboring drops with **h**) intensity traces color coded as in panel (g). **i**) A radial-phase-time plot of the pair of drops shown in panel (g) with a dispersion ratio of 2.5% (see text for definition). **j**) An oscillating pair of third-nearest neighbor drops with **k**) intensity traces color coded as in panel (j). **l**) A radial-phase-time plot of the pair of drops shown in panel (j) with a dispersion ratio of 0.9%. Image adapted from [118].

provided the spot of light is projected into the center of the drop and the intensity of light is not too high. However, the illuminated drops do influence neighboring non-illuminated drops. Light leads to the generation of bromine, which diffuses to non-illuminated drops and slows their frequency. Additionally, a small fraction of the light is reflected from the glass and can illuminate neighboring drops if the glass walls containing the sample are not perpendicular to the optic axis. We typically adjust the size and intensity of the illuminated region to be the minimum required to suppress oscillation in the illuminated drops so as to not suppress oscillation in neighboring drops. Measurements of the period of drops as a function of the intensity of illumination are described later in this paper.

In Figure 5.1(c) a schematic of a radial-phase-time plot is shown. Radial-phase-time plots are a convenient way of succinctly summarizing the synchronization behavior of an oscillatory network and are used throughout this paper. In a radial-phase-time plot, the radial axis is time and the angular axis follows phase in a right-handed direction. Plotted are the phase differences ($\phi_{i1} = \theta_i - \theta_1$) between the phases of the color coded drops (θ_i) and the reference drop (θ_1, blue). The phase difference is plotted to highlight the occurrence of constant phase differences.

Figures 5.1(d-f) demonstrate the synchronization between a nearest neighbor pair of drops. Figure 5.1(d) shows the locations of the two drops with all other drops inhibited. Figure 5.1(e) shows intensity traces of the two drops. Figure 5.1(f) is a radial-phase-time plot of the drops shown in Figure 5.1(d); the two oscillatory drops start in phase and develop a constant phase difference of $\phi = 0.8\pi$. Two identical oscillators in isolation are predicted to have anti-phase synchronization with a phase difference of exactly π whereas in experiment a range of constant phase differences near π are observed. We speculate the difference is due to some unknown heterogeneity in the boundary condition, or slight differences in the periods of the oscillators. For example, drops on the boundary may be illuminated with slightly different intensities, or the acid concentration of the drops may vary slightly.

Figures 5.1(g-i) demonstrate the lack of synchronization between a diagonally neighboring pair of drops. Figure 5.1(g) shows the locations of the two drops with all other drops inhibited. Figure 5.1(h) shows intensity traces of the two drops. Figure 5.1(i) is a radial-phase-time plot of the drops shown in Figure 5.1(g); the two oscillatory drops start in phase and undergo constant phase slipping, demonstrating a lack of synchronization. The dispersion ratio is calculated as $\Delta\omega/\omega_0$ where $\Delta\omega = |\omega_i - \omega_0|$ and ω_0 is the angular frequency of the reference drop. For the pair of drops shown in Figures 5.1(g-i) the dispersion ratio is 2.5%. Figures 5.1(j-l) demonstrate the lack of synchronization between a third-nearest

neighbor pair of drops. The very slow phase change between the oscillating drops indicates that they have nearly identical frequencies. For the pair of drops shown in Figures 5.1(j-l) the dispersion ratio is 0.9%.

The geometry of close-packed spheres in 2D dictates which ring networks can be created from a close-packed emulsion. Rings of three and six occur in the ordered lattice, while rings of four and five occur at relatively mechanically stable packing defects. Rings of eight and nine can be constructed as elliptical and triangular forms in the regular lattice (rings with two or three drops inside), but rings of seven are found only at defect boundaries and are mechanically highly unstable. A ring of seven has yet to be optically isolated from a close-packed emulsion for longer than a transient period.

To create geometries not found within close-packed spheres, we developed manufacturing techniques capable of constructing custom planar geometries. A ring of seven with constant chemical concentration boundary conditions is created by manufacturing an annulus shaped cavity from a 100μm thick polydimethylsiloxane (PDMS) layer contained between two glass sheets. We manufacture a "moat" outside the annulus that also contains drops. The drops outside of the annulus are held stationary optically, creating constant-concentration conditions for drops within the annulus. It is worth noting that as this is a closed system no chemical concentrations are truly constant but rather that the concentrations within the non-oscillatory drops change very little within the time frame of the experiment. See Appendix E for more details on the manufacturing process. Figures 5.2(a) and 5.2(b) demonstrate a ring network of seven implemented in thin PDMS. The inner annulus of the device is sized to hold the desired number of drops in a circular network. The outer channel (moat) of the device is filled with optically inhibited drops (indicated by a white x) that provide the constant-concentration boundary conditions. The PDMS layer between the annulus and outer channel diffusively couples the two features and serves only to maintain the geometry.

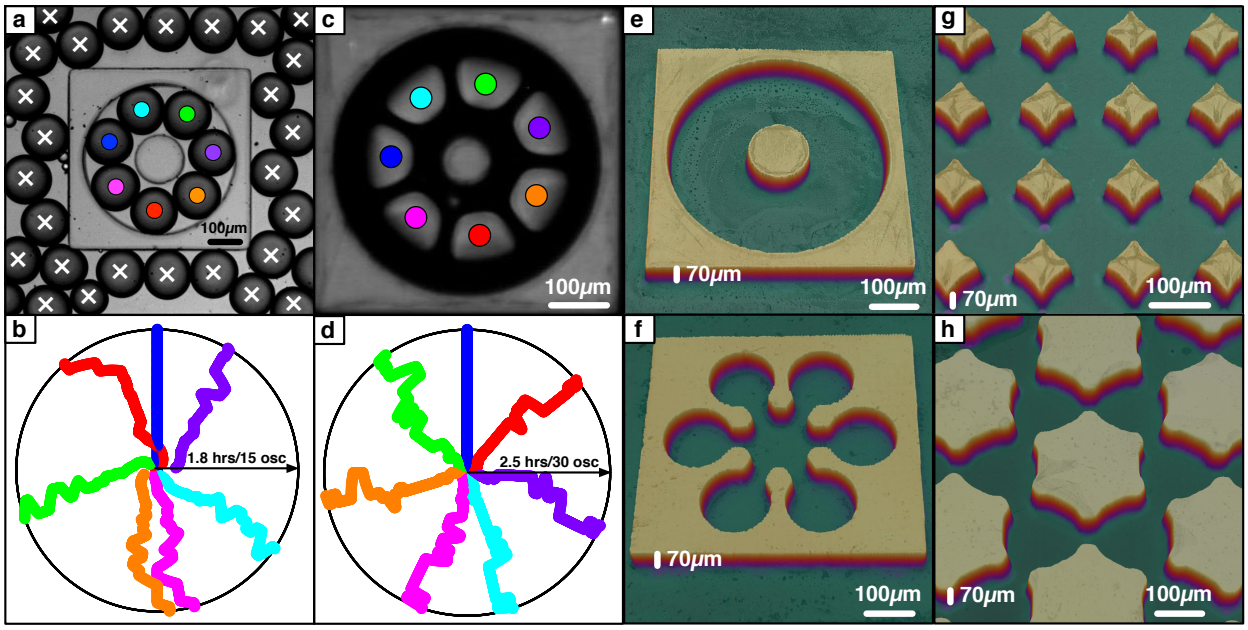

Figure 5.2: Planar networks with custom geometries. **a**) A polydimethylsiloxane (PDMS) device designed to create a ring network of seven with constant-concentration boundary conditions. The drops color coded as in panel (b). **b**) A radial-phase-time plot of the ring of seven shown in panel (a). **c**) An etched silicon device designed to create a ring network of seven with no-flux boundary conditions. The drops are color coded as in panel (d). **d**) A radial-phase-time plot of the ring of seven shown in panel (c). **e-h**) Network patterns etched into silicon wafers imaged using an optical profilometer. **e**) The ring network, **f**) a six-star network, **g**) a square lattice, and **h**) a triangular lattice. Image adapted from [118].

This diffusive coupling is evident as whenever a gas bubble is present in the outer channel the drops within the annulus cease oscillating. We explain this behavior as arising from bromine permeating through the PDMS to the gas causing a depletion of bromine within the drops in the annulus [117, 116, 13].

The expected patterns from ring networks of BZ emulsion have been examined previously using linear stability analysis (LSA) [120]. These results indicate that the network patterns should depend on the parity of the number of members. Networks with an even number of members should have a π phase separation between nearest neighbors resulting in two phase

clusters separated by π radians. Networks with an odd number of members (N) should have a $(N-1)\pi/N$ phase separation between nearest neighbors resulting in N phase clusters evenly distributed on the phase circle with a $2\pi/N$ phase difference between clusters instead of the π phase separation found for even-membered rings. The pattern observed in the radial-phase-time plot in Figure 5.2(b) resembles the expected behavior for a inhibitorily coupled ring of seven with seven phase clusters separated at $2\pi/7$. We speculate that deviation from the expected behavior is caused by the boundary-conditions resulting from the square geometry of the outer channel and the non-uniform packing of drops in the outer channel.

5.2.2 Physical Isolation/Neumann Boundary Conditions

Networks can be created with no-flux boundary conditions by etching containment patterns into silicon wafers and forcing the BZ emulsion into the cavities under a glass sheet. Crystalline silicon and amorphous silicon dioxide are impermeable to diffusion and thus constitute no-flux boundary conditions [117, 116, 13]. The devices are creating using Deep Reactive-Ion Etching (DRIE) [54, 142] where a process of plasma etching followed by surface treatment is repeatedly applied, allowing the plasma to etch deep into a silicon wafer with a nearly perpendicular profile, including etching entirely through the wafer [3]. The walls are slightly scalloped but this is controllable by adjusting the etch rate per cycle [71]. See Appendix E for more details. Figures 5.2(e-h) show profilometer images of empty DRIE etched devices.

A no-flux boundary condition device for a ring of seven drops was created by etching an annulus with an outer radius of 250 μm, inner radius of 100 μm (a functional radius of 150 μm), and depth of 70 μm into a silicon wafer (Figure 5.2(e)). The devices were loaded by placing 50 μL of emulsion on top of the empty annulus and sealing with a glass sheet (Figure 5.2(c)). Drops in Figure 5.2(c) are color coded to coincide with the corresponding

radial-phase-time plot (Figure 5.2(d)), which exhibits nearly perfect seven-phase clustering with a $2\pi/7$ separation between clusters, the expected pattern for a ring of seven. In the corresponding video the drops labeled in Figure 5.2(c) oscillate in the following sequence "blue-green-orange-pink-cyan-purple-red-blue-etc." corresponding to every other drop as progressing clock-wise around the ring. The radial-space-time plot of Figure 5.2(d) conveys the phase difference between successive oxidation transitions of the drops with the color-coded sequence of transitions proceeding in a counter-clockwise direction.

Etching devices out of a silicon wafer allows for customized planar geometries. For example, a six-star network (Figure 5.2(f)) can be constructed using no-flux boundaries provided by silicon, but could not be constructed with constant boundaries using either PDMS or optical isolation because of diffusive coupling between members of the arms of the star. Additionally, coupling strength depends on drop separation. For example, drops no longer synchronize in six-star networks, when the drops are separated by more than half their diameter. Figures 5.2(e-h) shows images from an optical profilometer of etched silicon devices used to make (e) a ring network, (f) a six-star network, (g) a square lattice, and (h) a triangular lattice. Future work will focus on the network patterns from star graphs with varying coupling strength and central node degree, and on the network patterns from various lattice structures.

5.2.3 Boundary Effects

In this section, we analyze the network patterns seen in circular networks with three, four, five, and six members as a function of boundary condition. We implement constant-concentration boundaries in two ways; with optical isolation within a close-packed emulsion and with optical isolation using drops stored in wells constructed from a thin PDMS barrier.

We implement no-flux boundaries by using etched silicon.

Network patterns can be observed for ring networks of up to six members with constant-concentration boundary conditions implemented with optical isolation within a close-packed emulsion. Ring networks of seven plus members can be created with constant-concentration boundary conditions implemented in thin PDMS boundaries from optically isolated drops and with no-flux boundary conditions implemented in etched silicon. Network patterns for ring networks with three, four, five and six members from all three implementations are shown in Figure 5.3 and network patterns for ring networks with seven members implemented in thin PDMS and etched silicon are shown in Figures 5.2(a-d).

Figure 5.3(a) shows the network patterns for a ring of three implemented with optical isolation within a close-packed emulsion (left), implemented with optical isolation with thin PDMS boundaries (middle), and implemented with etched silicon (right). The $2\pi/3$ solution is demonstrated in all three implementations with the etched silicon implementation demonstrating an initial transient and with the thin PDMS implementation temporarily demonstrating the unstable 00π state [59] where the three drops form two anti-phase phase clusters. The sequence of colors in the radial-phase-time plots demonstrates the handedness of the network pattern where the close packed implementation is right-handed and the other two implementations are left-handed.

Figure 5.3(b) shows the network patterns for a ring of four implemented within a close-packed emulsion (left), with thin PDMS boundaries (middle), and with etched silicon (right). All three implementations generally demonstrate two anti-phase phase clusters with varying degrees of finer details. The etched silicon implementation most closely matches the predicted pattern and, due to the impermeable post preventing cross-network diffusion, most closely resembles the predicted LSA structure. The finer details within the close-packed emulsion and thin PDMS implementations can possibly arise from cross-network diffusion through

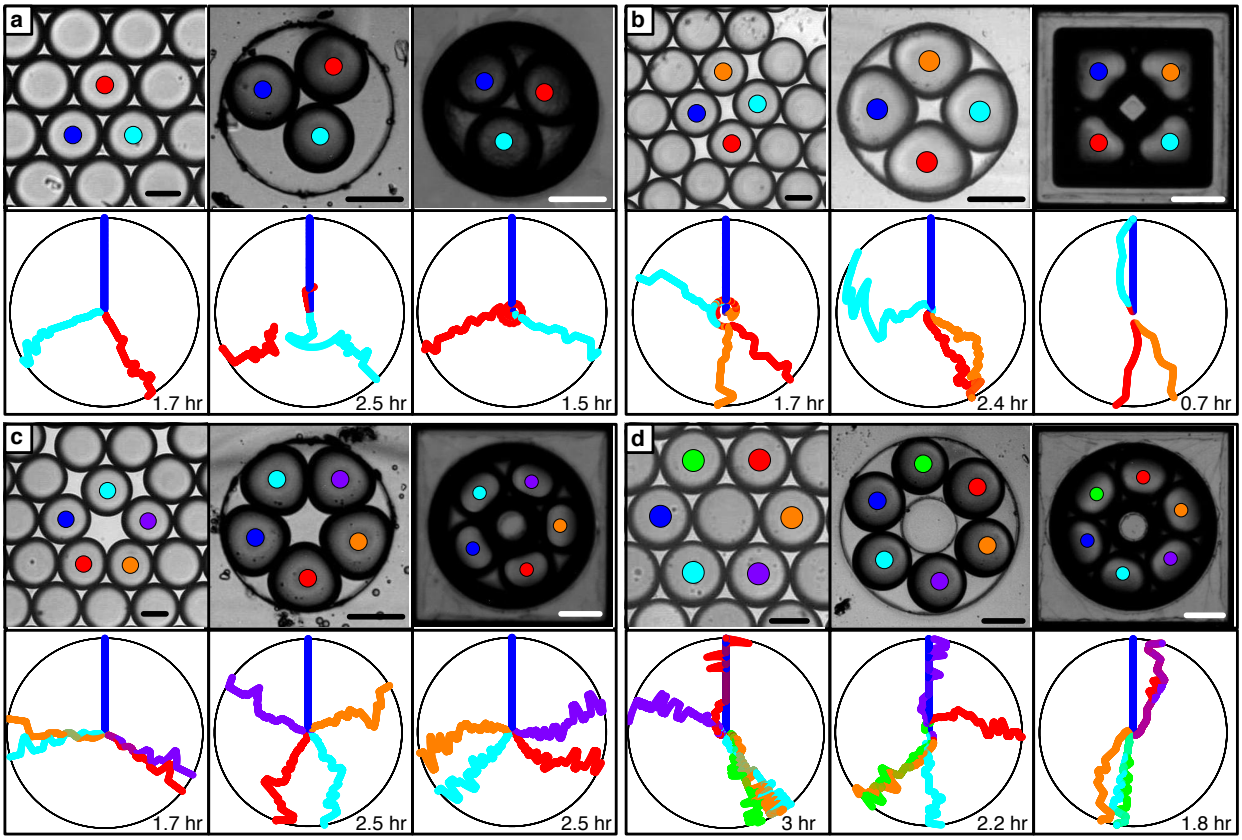

Figure 5.3: Network patterns observed from ring networks of three (**a**), four (**b**), five (**c**), and six (**d**) members with constant-concentration and no-flux boundary conditions. **Top**: Images of the networks with the oscillating drops color coded as below. All scale bars are 100μm. **Bottom**: Radial-phase-time plots of the networks above. **Left**: Circular networks with constant-concentration boundary conditions implemented via optical isolation in close-packed drops. Only the color coded drops are oscillatory; the other drops are optically inhibited. **Middle**: Circular networks with constant-concentration boundary conditions implemented in thin PDMS with optically inhibited drops in surrounding channels. The surrounding channels are not shown. **Right**: Circular networks with no-flux boundary conditions implemented in etched silicon. Image adapted from [118].

the central region creating additional network edges with lesser weights. These additional edges will induce repulsive behavior within the phase clusters resulting in the finer structure demonstrated.

Figure 5.3(c) shows the network patterns for a ring of five implemented within a close packed emulsion (left), with thin PDMS boundaries (middle), and with etched silicon (right). The close packed emulsion implementation demonstrates the "pseudo-triangle" state where the five drops assume the $2\pi/3$ pattern expected from a triangular ring of three with two sets of two drops each phase-locked together acting in unison as a single entity of the triangle. While this is not the most expected behavior for a ring of five (as determined by growth rate in the LSA), it is the second most expected state. In experiments both states are commonly found. The thin PDMS implementation is representative of the more typically expected state. The etched silicon implementation demonstrates behavior somewhere between the other two implementations, likely evidence of a superposition of states. The sequence of colors in the radial-phase-time plots demonstrates the handedness of the network pattern where the thin PDMS implementation is a left-handed pentagram, the etched silicon implementation is a right-handed pentagram, and the pseudo-triangle from the close packed implementation is a right-handed pseudo-triangle.

Figure 5.3(d) shows the network patterns for a ring of six implemented within a close-packed emulsion (left), with thin PDMS boundaries (middle), and with etched silicon (right). All three implementations generally demonstrate two anti-phase phase clusters with varying degrees of finer details. Additional examples of the network patterns for rings of six are shown in Figure 5.4 with a histogram of the nearest neighbor phase differences. The histograms combine the nearest neighbor phase differences at every time point for all eight experiments shown. The phase differences are calculated using $\phi_{ij} = |\theta_i - \theta_j|$ for $|\theta_i - \theta_j| \leq \pi$ and as $\phi_{ij} = ||\theta_i - \theta_j| - 2\pi|$ for $|\theta_i - \theta_j| > \pi$ to account for the symmetry of phase differences about

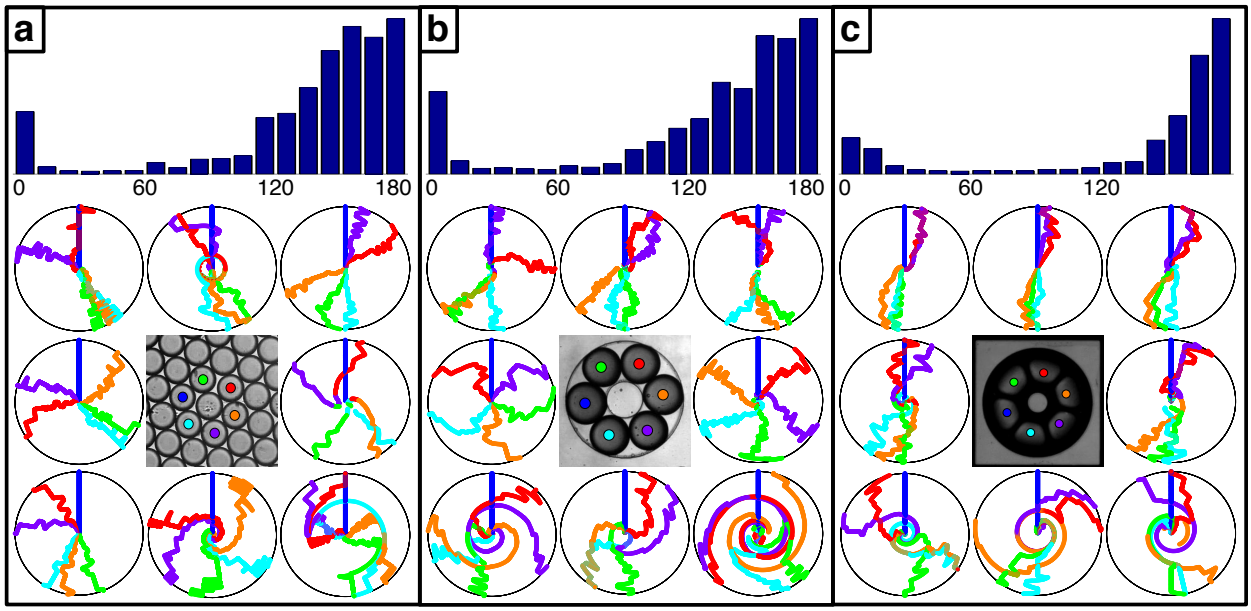

Figure 5.4: Nearest neighbor phase differences and network patterns for ring networks of six implemented via optical isolation in close packed drops. (**a**), in thin PDMS with optically inhibited drops in surrounding channels (**b**), and in etched silicon (**c**). **Top**: Histograms of the phase differences between nearest neighbor drops. In all cases the drops were started in-phase. **Bottom**: Radial-phase-time plots demonstrating the variety of observed patterns and a color coded image representing the locations of the drops. The top left plots are the same as in Figure 5.3(d). Image adapted from [118].

π. The small peaks in the histograms at $\phi = 0$ demonstrates that the drops were all started in phase and initial transients were not removed so that the rapidity of synchronization is also evident. The histograms in the etched silicon implementation are the most sharply peaked at π radians and most closely match the predicted pattern. We assume this is due to the impermeable post on the inner annulus preventing cross-network diffusion and the homogeneity of the no-flux boundary on the outer annulus. The close-packed and thin PDMS implementations demonstrate a broader range of behavior. Similarly to the rings of four, the additional patterns here could possibly arise from cross-network diffusion through the central region and coupling to heterogeneities on the outer boundary.

Figures 5.2(a-d) show the network patterns for a ring of seven implemented with thin PDMS boundaries (a-b) and with etched silicon (c-d). Both implementations demonstrate the expected behavior for a ring of seven with the etched silicon implementation again most closely matching both the expect behavior and the assumed graph structure. For rings of seven there are four "hands" which can be described as left-handed and right-handed heptagrams and left-handed and right-handed figure-eight heptagrams. The etched silicon implementation demonstrates the left-handed heptagram where the order of oscillation follows a regular left-handed {7/2} heptagram. The notation {7/2} indicates a seven sided figure with the sequence of oscillation following the 2^{nd} neighbor. The thin PDMS implementation demonstrates the right-handed figure-eight heptagram where the order of oscillation includes four left-handed {7/2} transitions, one right-handed {7/2} transition, and two right-handed {7/3} transitions that give the pattern its reversing "figure-eight" appearance. This arrangement is referred to as the right-handed variant since the {7/3} transitions are right-handed.

5.3 Network Perturbation

In addition to being able to create custom planar networks, the photo-activation of the Rubpy catalyst in BZ via the PIM allows for the perturbation of individual oscillators in networks created by any implementation. In the following sections, we will demonstrate the ability to set the initial conditions of the oscillators within the network, elongate the period of select oscillators within a network, and perturb the phase of select oscillators within the network.

5.3.1 Initial Conditions

In Figure 5.5(a) a line of six drops is optically isolated from a closed packed array of drops. The initial conditions of this linear network can be set by utilizing the delay between the end of optical inhibition and the onset of oscillations. While the drops are optically inhibited, all of the drops are held in the same oxidized state and thus there is no diffusive coupling between the drops. Immediately after optical inhibition is ended, the drops transition to a reduced (dark) state and after approximately one period begin to oscillate in-phase and remain in-phase for the first six oscillations. Figure 5.5(a) also demonstrates the ability to "reset" the drops back to in-phase. Staggering the ending of optical inhibition for each drop can create other initial conditions.

5.3.2 Period Elongation

The period of oscillators within a network can be elongated by under-inhibiting select drops as in Figure 5.5(b). Illuminating drops with an intensity of inhibitory light below the inhibition threshold (I_c) results in the drops oscillating with an elongated period. Period elongated drops are continuously illuminated with light undergoing the standard illumination duty cycle. Figure 5.5(c) is a plot of the ratio of the period of oscillation with light to that without light (T/T_0) of isolated drops as a function of fraction of light needed to inhibit oscillation (I/I_c). The data is fit to the function $T/T_0 = \alpha(1 - I/I_c)^{-1/2} + \beta$, consistent with behavior near a saddle-node bifurcation [107] with fitting parameters $\alpha = 0.1993$ and $\beta = 0.7226$. It is worth noting that an illumination of $I/I_c = 0.4$ results in a period of $T/T_0 < 1$ across numerous trials indicating that something interesting is going on for low intensity illumination which is worthy of future investigation.

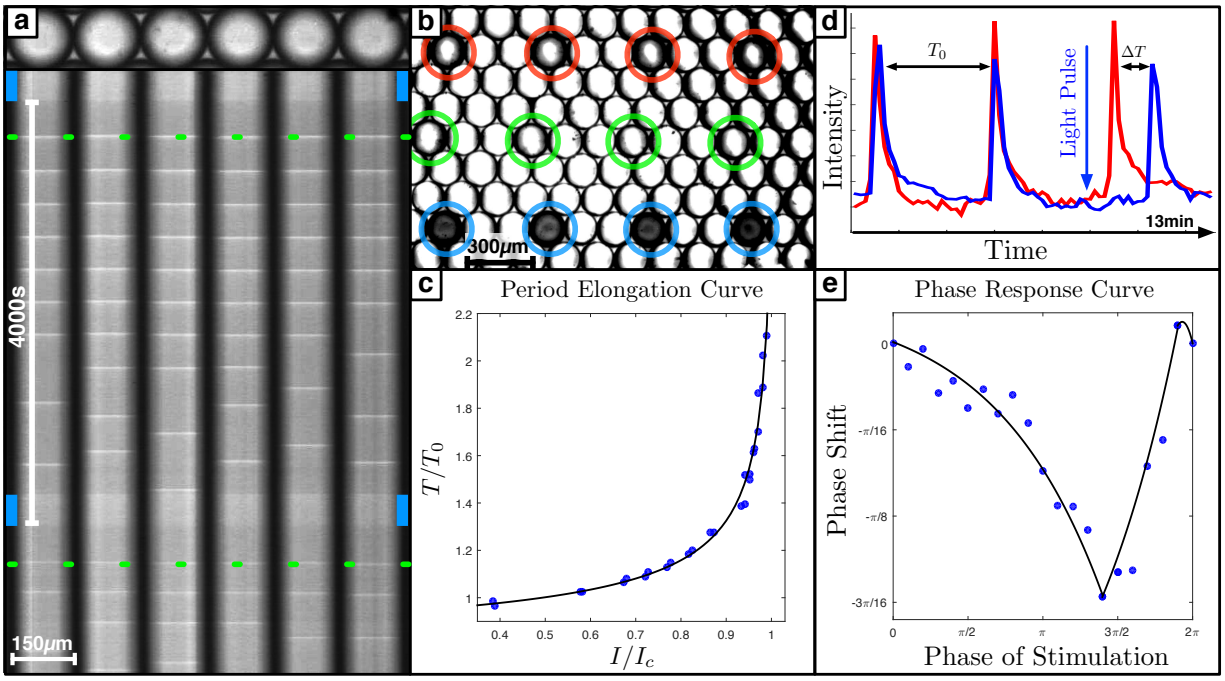

Figure 5.5: Setting the initial conditions, the period elongation curve, and phase response curve for BZ emulsion oscillators. **a**) A space-time plot (bottom) demonstrating setting the initial conditions of the drops (top) and resetting the phase back to zero at a later time. The blue bars indicate when the inhibitory light is on and the green dashes point out the first in-phase oscillation. **b**) A demonstration of the experiments conducted to measure the period elongation curve shown in (c). Twelve drops are optically isolated and allowed to oscillate with varying levels of inhibitory light. The bottom/blue four receive no inhibition, the middle/green four receive high inhibition, and the top/red four receive middling inhibition. **c**) The period elongation curve of isolated drops as a function of the inhibitory light plotted as a fraction of the inhibition threshold. **d**) A schematic of the experiments conducted to measure the phase response curve shown in (e). The drop represented with the blue trace received an inhibitory pulse at a specified phase, while the red trace is from the same drop, but recorded while unperturbed. The difference in period between the blue (perturbed) trace and the red (unperturbed) trace is used to calculate the phase response. **e**) The phase response curve of isolated drops. Image adapted from [118].

5.3.3 Phase Response Curve

The Phase Response Curve (PRC) characterizes the phase shift of an oscillator in response to a single, short perturbation as a function of the phase of the perturbation. Here we measure the PRC of a single pulse of light. Data was acquired by optically isolating 12 drops in a similar fashion as done in Figure 5.5(b). Then a single pulse of light was applied at a specified phase to each drop and the light induced phase shift was measured by measuring the elongation of a single period as shown in Figure 5.5(d). Using 12 drops in parallel facilitated rapid accumulation of statistics. Figure 5.5(e) shows the phase response curve for optically isolated drops using the formula $\Delta\theta = -2\pi\Delta T/T_0$ to calculate the phase response $\Delta\theta$ from the change in period ΔT.

5.4 Conclusion

We have created custom planar networks of non-linear chemical oscillators with either Dirichlet (constant-concentration) or Neumann (no-flux) boundary conditions and demonstrated the ability to perturb the phase and period of individual oscillators within the network. Constant-concentration boundary conditions were created using optical isolation in either a close-packed emulsion or in photolithographically manufactured wells containing drops in thin slabs of PDMS. No-flux boundary conditions were created by etching wells into silicon wafers. The differences in network patterns between implementations of the same graph with different boundary conditions was also examined. The ability to perturb individual oscillators by the external application of light was demonstrated by setting the initial conditions of the network, resetting the phase of the network, measuring the period elongation curve of isolated oscillators, and measuring the phase response curve of isolated oscillators.

It should be noted that this method has certain limitations such as the requirement that the network be planar. Networks with edges that cannot be constructed on a plane would require a three-dimensional device which is beyond the scope of the current research. Another limitation of the method described here is the requirement that the nodes be spaced physically near each other as the coupling strength between nodes is controlled by the physical length of the edges. This limitation renders graphs with a high degree or with edges connecting distant nodes difficult to manufacture.

Despite these limitations, the ability to create custom planar networks of nonlinear chemical oscillators and the ability to perturb individual oscillators within the network is a significant advance towards being able to achieve full synchronization engineering —the ability to implement a desired state with a specified network geometry. From what we have shown a desired planar network could be constructed with no-flux or constant-concentration boundary conditions, the initial conditions can be specified, individual oscillators can have their period elongated, and individual oscillators can be perturbed to create a desired synchronization pattern —a significant advance towards implementing the desired state within a specified network geometry. It is our intent to apply these technologies to the field of soft robotics.

Chapter 6

Conclusion

The primary aim of this Dissertation was to study the synchronization dynamics of coupled chemical oscillators due to topology. This work was performed using the Belousov-Zhabotinsky (BZ) reaction in an emulsion environment the background of which is described in Chapter 2. To conduct the experiments a Programmable Illumination Microscope (PIM) was constructed to selectively illuminate individual drops of BZ within the emulsion the design of which is described in Chapter 3. The first application of the PIM was to optically create diffusively coupled rings of BZ oscillators in order to test Turing's theory of morphogenesis. This test supported the utility of Turing's mathematical approach and validated his prediction that such a system could undergo morphogenesis without additional requirements. While testing Turing's theory it was also discovered that additional features were present that were not predicted from the mathematical approach Turing used and are still not fully explained. The test of Turing's theory of morphogenesis is described in Chapter 4. To study topologies beyond the ring network additional technologies were developed to enable the creation of custom planar networks of BZ drops. These technologies allow for precise control of the network geometry and boundary conditions as well as allowing for

perturbations of individual oscillators within the network. The development of these technologies is described in Chapter 5. The work presented in this Dissertation is a significant advance to the field of studying the synchronization dynamics of coupled chemical oscillators by probing the effects of topology on the emergent network behavior. More specifically the tools and technologies developed here facilitate the continued exploration of synchronization dynamics within networks by allowing for precise definition of the network geometry and by enabling the perturbation of individual nodes within the network as demonstrated by the test of Turing's theory.

The following section, Section 6.1, provides an overview of experiments in progress that utilize the advances presented in this Dissertation.

6.1 Future Experiments

A particularly interesting network to study is the star graph due to its implications as a fundamental component of the power grid [94]. Described here is the mathematical definition of a star graph and a linear stability analysis utilizing the structural modes of the star graph and the Vanag-Epstein (VE) model of the Belousov-Zhabotinsky (BZ) reaction. This analysis demonstrates that a topological "pruning" of the network can have dramatic effects on the synchronization dynamics.

6.1.1 Theoretical Foundation

Given the diversity of conventions it is worth briefly defining the notation used here. The star graph S_k is the graph with k outer nodes all with a single connection to the central node, node zero, with $N = k + 1$ total nodes as shown in Figure 6.1. The $N \times N$ Graph Laplacian $\mathcal{L}$ is defined as $\mathcal{L} = \mathcal{A} - \mathcal{D}$ where $\mathcal{A}$ is the adjacency matrix and $\mathcal{D}$ is the degree matrix.

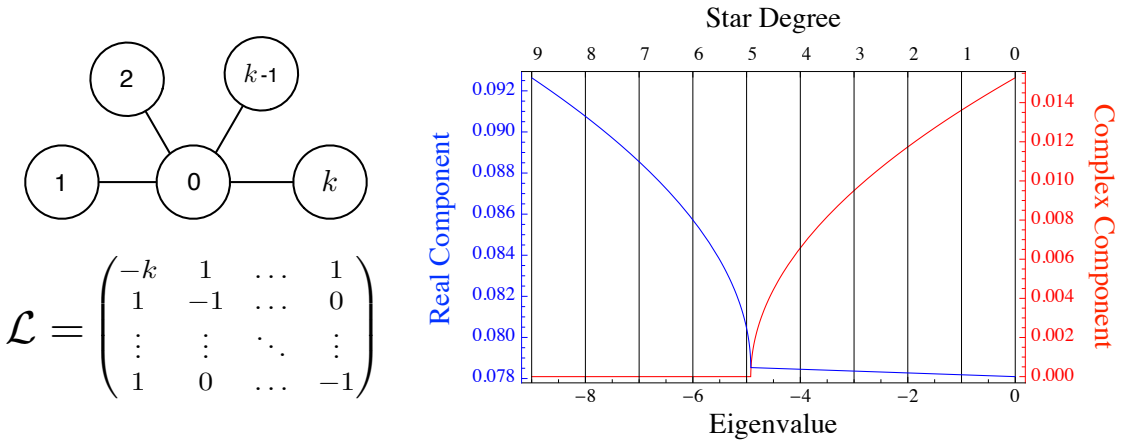

Figure 6.1: A diagram of a general star network with the Graph Laplacian $\mathcal{L}$ and linear stability analysis. For stars of degree $k \leq 4$ the LSA predicts oscillatory behavior while for stars of degree $k \geq 5$ the instability is stationary. The linear stability analysis is calculated as outlined in the text with μ calculated from Equation 4.2 for 150μm drops with a 5μm spacing. A concentration of 360mM MA is used and all other parameters as listed in Table 4.2.

The eigenvectors of $\mathcal{L}$ are referred to as the structural modes u_n where $n = [0, k]$ and the eigenvalues are α_n. The linear stability analysis examines the fluctuations $\tilde{x} = x - x_{ss}$ (where x_{ss} is the steady state value for a parameter x) which are stable based on the eigenvalues λ_{nm} of $J + \alpha_n D$ where J is the Jacobian, D is the diffusion matrix for the system, and $m = [1, j]$ for the j chemical species. For the system described here the Jacobian is that of the VE model, Equations D.1, where $j = 4$ and the diffusion matrix is that of Equation D.2.

For $k \geq 2$ there are three values for α_n and three modes u_n. The $n = 0$ mode (also present when $k = 0, 1$) of $\alpha_0 = 0$ and u_0 corresponds to the "in-phase" state where all nodes are in-phase. The $n = 1$ mode (also present when $k = 1$) of $\alpha_1 = -N$ and u_1 corresponds to the "anti-phase" state where nodes 1+ are in-phase and mutually anti-phase to node 0. The $n = 2+$ modes of $\alpha_{2+} = -1$ and u_{2+} are degenerate combinations of two outer nodes anti-phase and the rest stationary. From calculations using experimentally relevant parameters

it is found that the $n = 1$ ("anti-phase") mode dominates.

For chemical concentrations commonly used in experiments the results of the linear stability analysis for the $n = 1$ mode are shown in Figure 6.1. At the parameters used the VE model predicts two chemically viable fixed points which results in eight plots for λ with one degenerate pair having positive real components, the positive complex fork of which is shown in Figure 6.1. For these concentrations an isolated drop (k=0) oscillates but as the star degree is increased the system undergoes a transition such that the central drop ceases oscillations. For the conditions shown in Figure 6.1 this transition threshold is for stars of degree 5 or higher.

6.1.2 Experimental Outlook

The linear stability analysis shown in Figure 6.1 suggests that a topological "pruning" of the network could have a significant effect on the observed dynamics. A topological "pruning" would be the optical inhibition of a single node of the network that effectively removed that node from the network and resulted in an augmentation to the star degree or even the very definition of the network. For example, based on the conditions used in Figure 6.1 a S_5 star and a S_4 star would likely have very different synchronization dynamics. Pruning the fifth node of the S_5 star should induce a topological transition to the dynamics of the S_4 star which should then be reversible by ceasing the inhibition. Additionally, pruning the central node of the S_4 or S_5 star should reversibly destroy the synchronization dynamics entirely by removing all network connectivity. Experiments to test both of these hypotheses are in progress.

Appendix A

Alignment of the Programmable Illumination Microscope

This appendix is adapted from the appendix to [119] which is under review for publication at the *The American Journal of Physics*.

Alignment

A critical aspect in the usage of the PIM is the alignment of the field of view with the field of projection. Special care needs to be taken with the initial alignment and it is also recommended to check the alignment before every usage. The alignment software consists of seven steps which are outlined below and shown in Figure A.1 with output images. It is recommended that step seven is repeated before every usage.

Step One: Establish the software environment. This step creates the necessary output directories and locates the software dependencies. After this step the Matlab environment is ready.

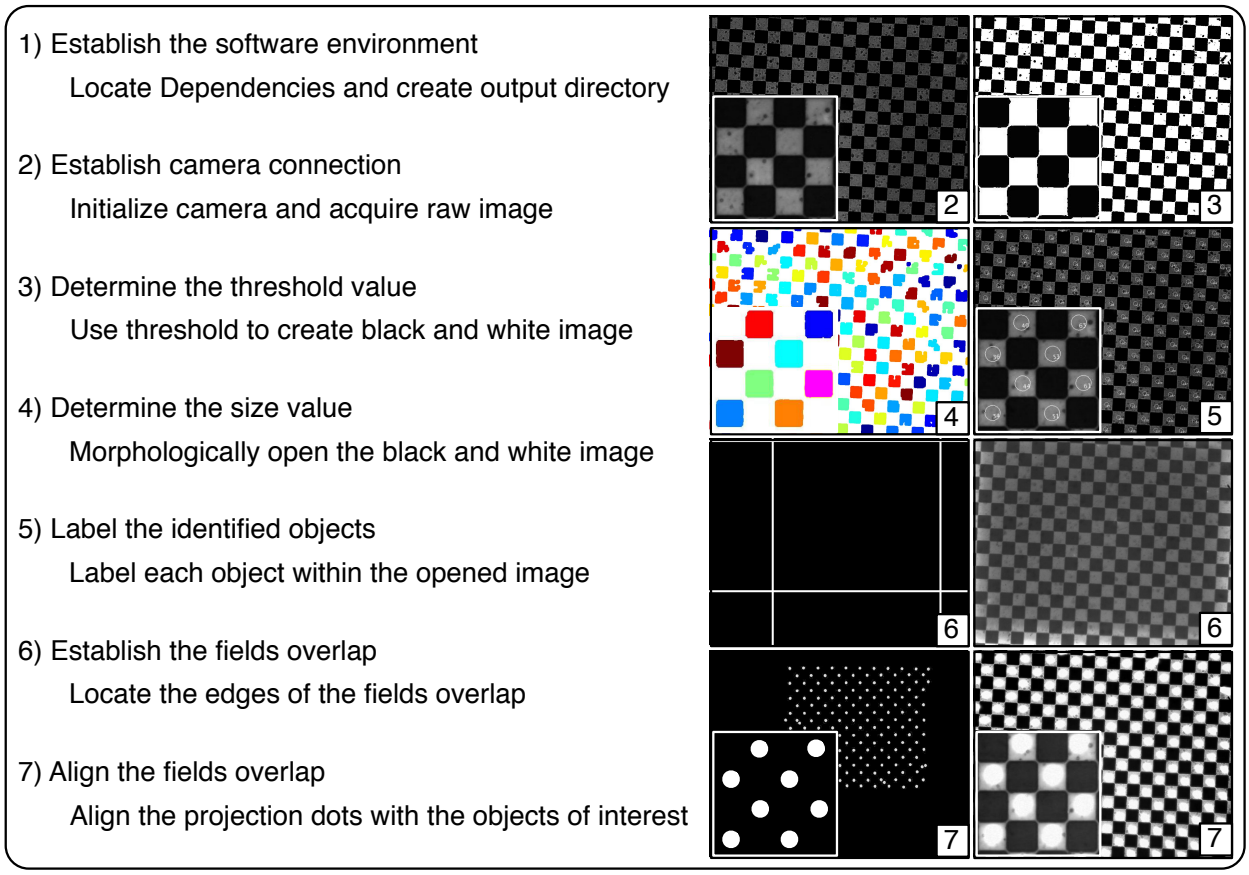

Figure A.1: An illustration of the alignment procedure for the PIM. The seven steps on the left correspond to the seven steps in the alignment software. The images at right are examples of the output using a checkerboard alignment grid (100μm squares) with a zoomed in region superimposed. Step one establishes the software environment on the computer independent of the PIM (no output). Step two establishes the connection with the camera and results in a raw image of the sample (raw image shown). Step three determines the threshold value to create a black and white image of the sample (black and white image shown). Step four determines the size value to morphologically open the black and white image and identify the objects of interest within the image (labelled image shown). Step five labels the objects of interest on the raw image for identification (tracked image shown). Step six establishes the overlap between the field of view and the field of projection (overlap within the field of projection shown on left and corresponding image from the field of view on the right). Step seven aligns the field of view with the field of projection (projection shown on left and corresponding image on the right). Image adapted from [119].

Step Two: Establish camera connection. This step creates the connection between Matlab and the camera. During this step the camera settings, illumination intensity, and focal plane are adjusted to capture an image of the sample.

Step Three: Determine the threshold value. This step creates a black and white image of the sample using the determined threshold value.

Step Four: Determine the size value. This step uses morphological opening to identify the objects of interest within the black and white image using the determined size value.

Step Five: Label the identified objects. This step creates labels on the raw image for each object of interest. The output image demonstrates that the software is correctly identifying the objects of interest. After this step the camera and software environment are ready.

Step Six: Establish the fields overlap. This step identifies the region of the field of projection that includes the field of view. A small routine within this section projects a white bar on an otherwise black screen that starts at the edge of the field of projection and is moved across the field of projection until detected by the camera. The current location of the bar within the field of projection is then recorded as the edge of the field of view. This is repeated for the other three sides until an outline of the field of view within the field of projection is identified. This outline provides the starting point for a finer alignment.

Step Seven: Align the fields overlap. This step aligns the field of view with the field of projection. Using the previously identified outline of the overlaps dots of light are projected onto the objects of interest. The location of the dots on the sample are checked manually and five parameters are adjusted until the dots align with the objects of interest to the users satisfaction. The five parameters are: horizontal and vertical compression, adjustments to the spacing of the dots that controls how far apart they appear, horizontal and vertical positioning, adjustments to the positioning of the dots that controls their location, and rotation, adjustments to the angular rotation between the field of view and the field of

projection.

Typical usage of the PIM after initial alignment starts with a brief repeat of steps one through five that loads saved parameters and is complete in under a minute. Step six is skipped entirely and the previous values are loaded from a saved file. Step seven is repeated in full using the previous values as a starting point. Repeating step seven can typically be completed in a couple of minutes. Note that the projector should be allowed to fully warm up (roughly thirty minutes for our systems) before aligning as the various structural components will likely have different rates of thermal expansion.

Appendix B

Components of the Programmable Illumination Microscope

This appendix is adapted from the appendix to [119] which is under review for publication at the *The American Journal of Physics*.

Components List

Most (if not all) components can be purchased used off of eBay. Most pieces of our apparatus came from from eBay, Thor Labs, and 80/20 Inc.

Key Components:

- Projector: NEC VT800, however this model has been discontinued and replaced with the NEC VT695. The NEC VT695 retails for $1399 but is currently available on eBay for $150. Removing the projector lens requires opening the projector enclosure, but the reversed lens can be positioned close enough to the LCD panel without having to modify the enclosure. We have also used the NEC NP1150 (retail: $3499 eBay: $350)

which has a convenient "lens release" to change the optics without opening the case and to position the reversed lens without modifying the enclosure. We recommend both the NEC VT695 and NEC NP1150 with the NEC NP1150 being simpler to use as it has both geometric lens shift and lens release. The NEC VT695 has neither of these features. The DLP projector used was a Dell 1210S (retail: $450 eBay: $150) and we never managed to make images of the same quality using the DLP projector as the LCD projectors.

- Computer: Apple iMac (Mid-2010 21.5" dual-core 3GHz i3) refurbished from the Apple Education Store for $1079. Currently available on eBay for $550.
- Camera: Allied Vision Marlin F131-B (eBay: $375).
- Reduction lens: 50mm Canon FD 1:1.4 lens (eBay: $50).
- Objective: Infinity corrected Olympus PlanN 4x (Thor: $200 eBay: $100).
- Microscope X-Y Stage: Generic stage (eBay: $50).
- Translation Stage: NewPort NCR 420 (eBay: $100).
- Beamsplitter: Chroma 21000 50/50 Beamsplitter (Chroma: $125).
- Focusing Lens: Thor Labs achromat 200mm (Thor AC254-200-A: $71)

Structural Components:

- Lens Mount Adapter: Canon FD to C-Mount (eBay: $25) and internal C-Mount to external SM1 (Thor SM1A10: $18)
- Camera Mount Adapter: internal SM1 to external C-Mount (Thor SM1A9: $18) and external SM2 coupler (Thor SM1T2: $18)

- Microscope Objective Mount Adapter: external SM1 to internal RMS (Thor SM1A3: $16)
- Beam Cube: 30mm Cage Cube (Thor C6W: $60), Base Plate (Thor B1C: $18), Top Plate (Thor B3C: $23), Filter Mount (Thor FFM1: $56), and Port Hole Cover (Thor SM1CP2: $17)
- Optics Mounts: SM1 Plates x4 (Thor CP02T: $20 each)
- Camera Light Hood: (Thor SM1S30: $ 20)
- Rails: Connecting Rails (Thor ER8-P4 $44)
- Stands: Posts x3 (Thor TR4: $6 each) and Stands x3 (Thor PH4: $9 each)
- Frame: We machined our own frame out of 14 feet of 80/20 1515 framing (eBay: $50), 12 80/20 3368 corner connectors (eBay: $6 each), 4 80/20 4302 inside corner brackets (eBay: $3 each), 1 package of 80/20 3320 mounting connectors (eBay: $15), and scrap aluminum.

Optional Components: (Köhler illumination)

- LED: Cyan LED (Luxeon: $8 eBay: $5), 350 mA Driver (Luxeon: $20, eBay: $14), 13V Power Supply (eBay: $10), and Mounting Plate (Thor CP01: $15)
- Lenses: 30mm x2 (Thor AC254-030-A: $77 each)
- Irises: iris x2 (Thor SM1D12D: $58 each)
- Neutral Density Filter: OD10 filter (Thor NE10A-A: $68)
- Green Filter: Bandpass filter (Thor FB510-10: $84)

- Optics Mounts: Thick SM1 Plates for lenses and bandpass filter x3 (Thor CP02T: $20 each)
- Optics Mounts: Thin SM1 Plates for irises and neutral density filter x3 (Thor CP02: $16 each)
- Rails: Connecting Rails (Thor ER8-P4 $44)
- Stands: Posts x2 (Thor TR4: $6 each) and Stands x2 (Thor PH4: $9 each)

Appendix C

Derivation of the Coupling Strength Between Two Drops

This appendix is adapted from the supplement to [120] which has been published by the *Proceedings of the National Academy of Sciences of the United States of America*.

Coupling Strength Derivation

A key assumption in the Turing model is that cells are diffusively coupled, as characterized by the diffusive rate, μ_c, where $dc_i/dt = \mu_c (c_{i-1} + c_{i+1} - 2c_i)$. with c_i the concentration of a single chemical species in the i^{th} cell. However, Turing did not specify a form for the coupling term μ, so it is treated as a fitting parameter in comparison of theory with experiment. We supplement Turing's model by calculating how the coupling term depends on our system's physical and chemical parameters.

Following Turing, our model consists of a ring of identical cells, which are considered to be small enough so that diffusion makes the concentration inside each cell uniform on a

time scale that is much shorter than any chemical reaction dynamics. To calculate μ_c we first consider a one dimensional case, illustrated in Figure 4.3c. Consider two cells each with an aqueous dimension of length a separated by an oil gap of length b such that the total center to center distance is $a + b$. Again, like Turing, we assume that no chemical species accumulate in the oil phase. Conservation of mass demands that $\partial c/\partial t = -\partial J/\partial x$, where c is the concentration and J is the concentration flux. Additionally, Fick's first law states that $J = -D\nabla c$. When discretized we have:

$$\frac{\Delta c}{\Delta t} = -\frac{\Delta J}{\Delta x} = \frac{J_{i-1,i} - J_{i,i+1}}{a}$$

where we make the additional assumption that the concentration is uniform within the aqueous phase, so the only fluxes are across the oil gaps:

$$J_{i-1,i} = \frac{DP_c}{b}\left(c_{i-1} - c_i\right) \quad J_{i,+1i} = \frac{DP_c}{b}\left(c_i - c_{i+1}\right)$$

Which, when substituted into our conservation of mass equation yields:

$$\frac{\Delta c}{\Delta t} = \frac{DP_c}{ab}\left(c_{i-1} + c_{i+1} - 2c_i\right) \Rightarrow \mu_c = \frac{DP_c}{ab}$$

where D is the diffusion constant in oil for chemical species c and P_c is the oil/water partition coefficient for species c. For our analysis we used the values $D = 3 \times 10^{-9} m^2/s$, $P_x = 0.05$, $P_y = P_z = 0$, and $P_u = 2.5$.

The above result for μ_c was derived for cells on a line in one dimension. Experimentally, our BZ drops confined in cylindrical capillaries resemble spherocylinders. We can improve on the previous result by using the Derjaguin approximation to calculate the diffusive flux between two spherocylinders confined in a cylindrical capillary of diameter d. From the

geometry of Figure 4.3d we know that the gap β at any point is $\beta = b + 2\Delta$ where $\rho^2 + (r - \Delta)^2 = r^2$. We can solve for Δ and find $\Delta = r \pm \sqrt{r^2 - \rho^2}$. As $\Delta \to 0$ when $r \to \infty$ we can state that:

$$\Delta = r - \sqrt{r^2 - \rho^2}$$

Thus we know β as a function of ρ is:

$$\beta = b + 2\left(r - \sqrt{r^2 - \rho^2}\right)$$

As $a + b$ is a constant, and from the geometry we can see that $\alpha + \beta$ is the same constant, we can write α as a function of ρ as:

$$\alpha = a - 2\left(r - \sqrt{r^2 - \rho^2}\right)$$

To apply the Derjaguin approximation we calculate the average flux in cylindrical coordinates from

$$\mu_c = \frac{1}{A}\int_\theta \int_\rho \mu_c(\rho)\rho d\rho d\theta$$

which when the proper symmetries are applied becomes:

$$\mu_c = \frac{2}{r^2}\int_0^r \mu_c(\rho)\rho d\rho$$

Using the form of μ_c derived above and replacing the drop width a with $\alpha(\rho)$ and the gap size b with the gap $\beta(\rho)$ we have:

$$\mu_c = \frac{2}{r^2}\int_0^r \frac{DP_c}{\alpha(\rho)\beta(\rho)}\rho d\rho$$

which in experimental units of d is:

$$\mu_c = \frac{8}{d^2}\int_0^{\frac{d}{2}} \frac{DP_c}{\left(a-d+2\sqrt{\frac{d^2}{4}-\rho^2}\right)\left(b+d-2\sqrt{\frac{d^2}{4}-\rho^2}\right)}\rho d\rho$$

Solving the integral yields:

$$\mu_c = \frac{2DP_c\,(b+d)}{d^2\,(a+b)}\left(\ln\left(\frac{b+d}{b}\right)+\frac{a-d}{b+d}\ln\left(\frac{a-d}{a}\right)\right)$$

This model is valid for unconfined drops with a diameter greater than, or equal to, the capillary diameter. When the drops are spheres with a diameter equal to the capillary diameter, $(a = d)$:

$$\mu_c = \frac{2DP_c}{a^2}\ln\left(\frac{a+b}{b}\right)$$

In the weak coupling limit of spherical drops separated by a great distance, $a << b$, the result simplifies further to

$$\mu_c = \frac{2DP_c}{ab}$$

This last result is similar to the coupling strength in 1D; the factor of 2 difference comes from the circular shape of the drop in the capillary.

We cannot directly measure μ_c and so instead examine the effect that coupling has on the dynamics of two weakly coupled chemical oscillators. An individual BZ drop oscillates on a limit cycle. If two oscillators are weakly coupled, then, to first order, they remain on the limit cycle, but synchronize with a phase difference of either 0 or π radians. In the limit of weak coupling, the dynamics of the phase difference between two coupled drops evolves exponentially with rate constant, z, proportional to the coupling strength. To perform the corresponding experiments, we fill cylindrical capillaries with drops and use light to

chemically isolate a pair of adjacent drops (see Figure 4.3a). The phase difference between the two drops is measured as a function of time, from which the rate of synchronization z is measured (see Figure 4.3e). For each measured rate constant z we calculate a theoretical rate constant z_{th} by integrating Equations 4.1 and 4.2. Measured and calculated rate constants for a wide range of drop sizes and separations are compared in Figure 4.3f,g. To compare experimentally measured synchronization rates to rates calculated from the full nonlinear solution of Equations 4.1 and 4.2, given in the main text, we introduced one adjustable parameter, f, in Equation 4.2, by replacing μ_c with $f\mu_c$. While the functional form of the coupling strength (Equation 4.2) fits the time-dependent synchronization data well for a wide range of oil gaps and drop diameters, the combination of the Turing model (Equation 4.1) with our explicit calculation of the interdrop coupling (Equation 4.2), overestimates the coupling strength by nearly two orders of magnitude; while theory predicts $f = 1$, experimentally we find $f = 0.0152$.

On the one hand, our theory of coupling strength is not very good, giving a deviation between theory and experiment of a factor of 60. On the other hand, it is an improvement over Turing's model in which no functional form of μ_c is given, requiring that μ_c must be experimentally determined for each combination of drop size and spacing. Our model requires making only one measurement for an arbitrary drop size and spacing to determine the coupling strength by measuring f. Once that single fitting parameter is obtained, then $f\mu_c$, with μ_c given by Equation 4.2, can be used to predict all other coupling strengths as a function of drop size and spacing.

Appendix D

Linear Stability Analysis for a Periodic Ring

This appendix is adapted from the supplement to [120] which has been published by the *Proceedings of the National Academy of Sciences of the United States of America*.

Linear Stability Analysis

The linear stability analysis (LSA) for a periodic ring of N cells is performed using the four-variable Vanag-Epstein (VE) model. We begin with the reaction-diffusion Equation 4.1

$$\frac{d\boldsymbol{c}_r}{dt} = \boldsymbol{F_c}(\boldsymbol{c}_r) + \boldsymbol{M_c}\left(\boldsymbol{c}_{r-1} + \boldsymbol{c}_{r+1} - 2\boldsymbol{c}_r\right) \tag{4.1}$$

where $\boldsymbol{c}_r$ is a vector containing the concentrations of the chemical species in the r^{th} cell, $\boldsymbol{F_c}$ is a vector function describing the chemical kinetics of the c-species, and $\boldsymbol{M_c}$ is a diagonal matrix containing the coefficients of diffusive transport (μ_c) of the c-species from drop to

drop [10]. For the VE model with four concentrations, $\boldsymbol{c} = (x, y, z, u)$, and $\boldsymbol{F_c}$ is given as

$$\begin{aligned} f_1(x,y,z) &= -k_1xy + k_2y - 2k_3x^2 + k_4x(c_0 - z)/(c_0 - z + c_{min}) \\ f_2(x,y,z,u) &= -3k_1xy - 2k_2y - k_3x^2 + k_7u + k_9z \\ f_3(x,z) &= 2k_4x(c_0 - z)/(c_0 - z + c_{min}) - k_9z - k_{10} \\ f_4(x,y,z) &= 2k_1xy + k_2y + k_3x^2 - k_7u \end{aligned} \tag{D.1}$$

with the constants and variables defined in Table 4.2. The coupling matrix is

$$\boldsymbol{M_c} = \begin{pmatrix} \mu_x & 0 & 0 & 0 \\ 0 & \mu_y & 0 & 0 \\ 0 & 0 & \mu_z & 0 \\ 0 & 0 & 0 & \mu_u \end{pmatrix} \tag{D.2}$$

with different coefficients, μ_c, to take into account the fact that different species will partition to different extents between the oil and aqueous phases. The first step in LSA is finding the steady states, $\boldsymbol{c}_s$, by solving analytically, $\boldsymbol{F_c} = 0$. Next, the chemical rate Equations D.1 are linearized about the steady state and the dynamics of a small perturbation $\boldsymbol{c}_r = \boldsymbol{c}_s + \delta\boldsymbol{c}_r$ is explored in the linearized equations

$$\partial_t \delta\boldsymbol{c}_r = \boldsymbol{A}\delta\boldsymbol{c}_r + \boldsymbol{M_c}(\delta\boldsymbol{c}_{r-1} + \delta\boldsymbol{c}_{r+1} - 2\delta\boldsymbol{c}_r) \tag{D.3}$$

with $\boldsymbol{A}= \partial\boldsymbol{f}/\partial\boldsymbol{c}$ the Jacobian matrix of Equations D.1 with coefficients

$$a_{ij} = \left.\frac{\partial f_i}{\partial c_j}\right|_{\boldsymbol{c}_s} \tag{D.4}$$

To solve the linearized Equations D.3, they are Fourier transformed by setting

$$\delta\boldsymbol{c}_r = \delta\boldsymbol{c}_q e^{\sigma_q t} e^{iqr} \tag{D.5}$$

with $q = 2\pi s/N$ where $s \in [0, s_{\max}]$ is an integer with $s_{\max} = N/2$ for N even and $s_{\max} = (N-1)/2$ for N odd. This leads to the following eigenvalue equation

$$0 = \boldsymbol{A} - \sigma_q \boldsymbol{I} - 4\sin^2\frac{q}{2}\boldsymbol{M_c} \tag{D.6}$$

from which the eigenvalue σ_q is found as a function of q. If all eigenvalues have negative real parts, there is a stable steady state. If one or more eigenvalue has a positive real part, then the steady state is unstable. The largest positive value of σ_q represents the fastest growing mode, and its q is associated with the corresponding Turing case. If σ_q is positive real, the Turing instability is non-oscillatory, corresponding to a *stationary Turing instability*; if σ_q is complex with a positive real part, then there is an *oscillatory Turing instability.* The eigenvalue σ_q was found numerically using the parameters shown in Table 4.2 and a fixed ratio of μ_x=$\mu_u/50$ and $\mu_y = \mu_z = 0$. Using Mathematica, we calculated the state diagram as a function of the bromine coupling strength, μ_u, and malonic acid concentration m, shown in Figure 4.5. *There are no adjustable parameters in calculating the state diagram.*

In more detail, when solving $\boldsymbol{F_c} = 0$, we found six analytical steady states, which were then converted to numerical steady states and filtered to remove trivial and unphysical solutions. The remaining steady states (usually two, never more, occasionally only one) were then categorized as reduced if $z_{ss} \approx c_{min}$ or oxidized if $z_{ss} \approx c_0$. The analytical Jacobian matrix was then converted to numerical Jacobian matrices using the parameters and steady state solutions. The numerical Jacobian matrices and diagonal diffusion matrices were used to solve for the eigenvalues of each specified value of μ_u and m. Given two steady state solutions for each parameter set and a four variable system, each parameter set yields eight eigenvalues, and each eigenvalue is a function of the wavenumber q. The maximum value for the real component of each eigenvalue was calculated, and that with the largest

real maximum was identified as the dominant mode. If all eight maximal real values were negative, then that case was identified as a stable steady state with no associated Turing pattern.

In Figure 4.5a, along the left axis corresponding to low malonic acid concentration (MA $<$ 1 mM) and independent of coupling strength, there is one stable steady state corresponding to the oxidized state. Everywhere else, there are two steady states; one stable and oxidized, the other unstable and reduced. Along the bottom axis, corresponding to zero coupling strength $\mu = 0$, LSA predicts that the unstable reduced steady state undergoes a non-oscillatory Turing instability (case (a)) for 1 mM $<$ MA $<$ 370 mM and an oscillatory Turing instability (case (b)) for MA $>$ 370 mM. Away from the axes, the reduced steady state is unstable to one of the Turing instabilities corresponding to cases (b-f).

Once the dominant eigenmode was identified, that parameter set could then be further categorized. First the wavenumber q_T at which the real maximum occurs is identified as the dominant wavenumber and thus the associated Turing wavelength is $\lambda_T = 2\pi/q_T$. Second, the magnitude of the imaginary component of the dominant eigenvalue at the dominant wavenumber q_T is identified as the frequency ω_T. See Figure 4.9 for examples. The six Turing states are defined by their dominant wavenumber q_T and associated frequency ω_T. However, given the numerical rounding and desire to compare with experiment, a small amount of leeway was allowed for defining states in the LSA. The mode was identified as stationary if $\omega_T < 10^{-7}$ rather than strictly equal to zero, the wavelength was identified as minimal if $\lambda_T < 2.02$ (measured in units of cell number) rather than strictly equal to 2, and the wavelength was identified as maximal if $\lambda_T > 39.6$.

Appendix E

Construction of Custom Planar Network Containment Devices

This appendix is adapted from the supplement to [118] which is in preparation to be submitted to *Chaos*.

Planar Network Containment Devices

The following sections detail the methods used to create our devices and are intended to assist those who wish to implement their own planar networks in a BZ emulsion system. The experiments described here use a BZ formulation with final concentrations of 400mM Malonic Acid, 80mM Sulfuric Acid, 300mM Sodium Bromate, 10mM Sodium Bromide, 3mM Ferroin, and 1.2mM Rubpy. Some experiments used slight variations on this formulation with concentrations of 640mM Malonic Acid, 2.5mM Sodium Bromide, and/or 0.4mM Rubpy. These variations are minor as within these concentration ranges the only noticed effects are slight variations in period, initial transients, and photosensitivity.

Close-Packed BZ Emulsion

The BZ emulsion is created using a typical flow-focusing microfluidic device with surfactant (RAN Biotechnologies FluoroSurfactant) stabilized oil (3M^{TM} Novec^{TM} 7500 Engineered Fluid) and collected in an Eppendorf tube. An approximately 1cm length piece of 2mm$\times$100μm rectangular glass capillary (VitroTubes^{TM}) is cut with a diamond scribe. The cut piece is held in forceps and one end is inserted into the emulsion. Capillary action is sufficient to fill the capillary. After the capillary is entirely filled leaving no air gaps, the ends are dipped in epoxy (Bob Smith Quik-Cure^{TM} five minute epoxy) and placed flat on a microscope slide. It is important to seal the capillary gas tight otherwise CO_2 bubbles form which displace the oil, quench the oscillation, and move drops. More epoxy is carefully applied to the ends of the capillary to attach it to the slide. The portion of the capillary to be imaged remains clear of epoxy. After the epoxy has cured, the slide is placed in the microscope for experimentation.

Thin PDMS Devices

The thin PDMS devices are created using a four step process. The first step is to create a silicon master with the desired features in inverse using standard photolithography methods.

The second step is to create a PDMS cast of the silicon master as shown in Figure E.1(a) where the silicon master is placed in a specially designed frame that allows for the curing of 40-50g of PDMS to create an inverse cast of the silicon master. The frame consists of a stable base and a circular outer ring. When bolted together the two parts of the frame contain the fluid PDMS. The silicon master is adhered to the base of the frame using silicon based vacuum grease. After curing, the mold frame is removed and the PDMS cast is peeled off of the silicon master.

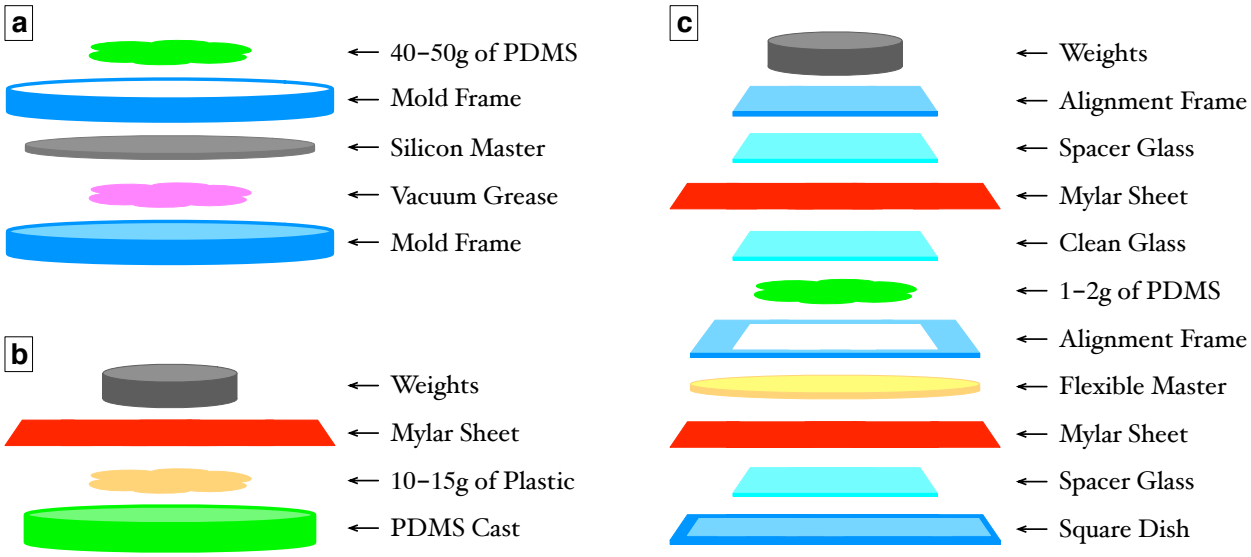

Figure E.1: Schematic illustrations of the steps to make thin PDMS devices. **a)** Making a PDMS cast of a silicon master. A silicon master with the desired features in inverse is prepared by traditional photolithographic methods and attached to a hard plastic frame with silicon based vacuum grease. An outer containment frame is attached and 40-50g of PDMS are poured over the top. After degassing and curing, the PDMS cast can be removed from the frame and detached from the silicon master. **b)** Making a flexible plastic master from a PDMS cast. A PDMS cast of the desired features is filled with 10-15g of plastic urethane resin and thoroughly degassed. After degassing, the resin is covered with a protective mylar sheet and pressed flat with weights. After curing, the flexible master can be removed from the PDMS cast. **c)** Preparing a thin PDMS device from a flexible plastic master. A flexible plastic master with the desired features in inverse is placed in a square dish on top of a protective mylar sheet and a glass spacer. A laser cut alignment frame is placed over the flexible master and aligned with the features. 1-2g of PDMS are poured over the features and degassed. While degassing, a glass slide is freshly plasma cleaned and then placed on the degassed PDMS, snugly fitting within the alignment frame. Another protective mylar sheet is placed over the clean glass followed by another glass spacer, the top of the alignment frame, and flat weights. The entire stack is further degassed before curing. After curing, the stack is carefully disassembled as the PDMS has cured onto the clean glass. Image adapted from [118].

The third step is to create a flexible plastic master with the desired features in inverse using the PDMS cast of the silicon master as shown in Figure E.1(b). 10-15g of urethane resin (Smooth-On Crystal Clear® 204 urethane casting resin) is prepared and poured into the PDMS cast. Special care needs to be taken to thoroughly degas the resin as it is very viscous and prone to retaining bubbles. After degassing, the resin is pressed flat within the PDMS cast using flat-bottomed weights. A mylar sheet is placed between the resin and the weights to prevent the resin from adhering. After curing, the flexible master can be peeled off of the PDMS cast.

The fourth step is to create the thin PDMS device using the flexible plastic master as shown in Figure E.1(c). The flexible master is placed in a square dish on top of spacer glass and a mylar sheet. The spacer glass creates a space for excess PDMS to drain into and the mylar sheet prevents the PDMS from adhering to the plastic dish. A laser cut alignment frame is placed over the flexible master and the master is positioned so that the features are aligned with the frame. 1-2g of PDMS are poured over the features and degassed. While degassing, the glass microscope slide that will carry the thin PDMS device is freshly plasma cleaned. The glass slide is taken directly from the plasma oven and placed immediately onto the degassed PDMS. This step and the composition of the glass (Gold Seal™) has shown to be critical to prevent the PDMS from later peeling off of the glass carrier. Another mylar sheet is placed over the carrier glass followed by another spacer glass, the top piece of the alignment frame, and flat-bottomed weights. The applied wights will squeeze excess PDMS into the space at the bottom leaving only a very thin layer on the carrier glass. The exact thickness of this layer will depend on the viscosity of the PDMS fluid and the weight applied. The assembled alignment frame prevents any relative movement between the PDMS and the carrier glass as the alignment frame is laser cut so that the carrier glass fits snugly within the alignment frame. The entire stack is further degassed before the PDMS is cured. After

curing, the stack is carefully disassembled and excess PDMS is cut from the outside of the carrier glass/flexible master sandwich. The last step of the disassembly is to carefully peel the flexible master off of the carrier glass.

Etched Silicon Devices

The etched silicon chips are created using standard DRIE technology which is a four step process. The first step is to create a silicon master with the desired features using positive resist. It is critical that positive resist that can be washed off post-curing with acetone is used.

The second and third steps are carried out repeatedly within the DRIE machine. The second step applies a nearly isotropic plasma that etches exposed silicon but does not etch the positive resist. The third step applies an inert passivation layer that protects the entire surface. The second step is then repeated and the passivation layer is etched away but, due to the directionality of the plasma, the passivation layer is preferentially etched vertically thus protecting vertical edges and preventing undercutting. The second and third steps are continually repeated until the desired etch depth is reached. The iterative process leaves the vertical edges scalloped, but the degree of scalloping is tunable by adjusting the duration of the etch step.

The fourth step is to wash off the positive resist using an acetone bath. If needed, acetone residue can then be washed off using an isopropanol bath. After washing, all applied materials will have been removed except for possibly passivation residue on the vertical edges of the etches.

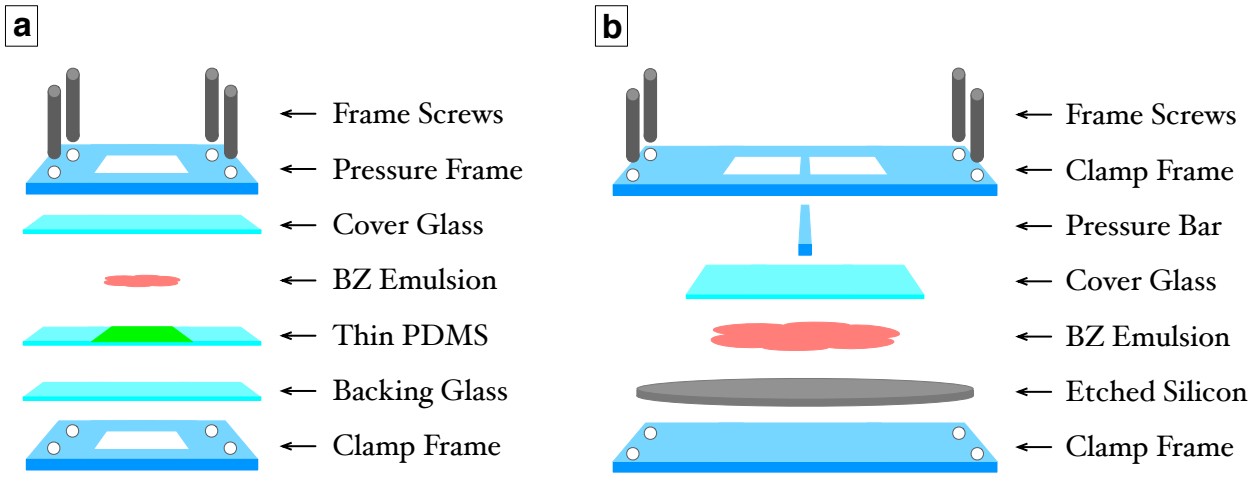

Figure E.2: Schematic illustrations of the device clamps. **a)** Thin PDMS device clamp. The thin PDMS device is placed onto a backing support glass on the bottom of the clamp frame. These devices are imaged using transmission illumination so the top and bottom of the clamp have optical access holes. The BZ emulsion is placed on the device and covered with a cover slide. The top of the clamp is lowered onto the cover slide and the screws are tightened to apply pressure. **b)** Etched silicon device clamp. The etched silicon device is placed onto the bottom of the clamp frame. These devices are imaged using reflection illumination so only the top of the clamp has an optical access hole. The BZ emulsion is placed on the device and covered with a cover slide. A plastic bar is placed under the cross bar of the top of the clamp so that pressure is applied from the center. The top of the clamp is then lowered and the screws are tightened to apply pressure. Image adapted from [118].

Top-Loaded Devices Clamping

The thin PDMS and etched silicon devices are used in experiments by clamping a cover slide onto the features. The two devices use slightly different clamps as can be seen in Figure E.2.

The clamp for the thin PDMS devices has optical access holes on the top and bottom to allow for transmission illumination. The thin PDMS carrier glass is placed on a backing glass for support. The thin PDMS is wetted with oil to prevent air bubbles from being caught in the features. The BZ emulsion is then pipetted onto the features and a cover slide is placed on top. The top of the frame is lowered and pressure is applied by tightening the frame screws.

The clamp for the etched silicon devices has an optical access hole only on the top, as the wafer is opaque so the device must be imaged in reflection only. The silicon device is placed directly in the lower portion of the frame and wetted with oil to prevent air bubbles from being caught in the features. The BZ emulsion is then pipetted onto the features and a cover slide is placed on top. A plastic bar is placed under the cross bar of the top of the clamp so that pressure is applied to the device from the center to prevent buckling. The top of the clamp is then lowered and pressure is applied by tightening the frame screws.

Bibliography

[1] Daniel M. Abrams and Steven H. Strogatz, *Chimera states for coupled oscillators*, Physical Review Letters **93** (2004), no. 17, 1–4.

[2] Réka Albert and Albert-László Barabási, *Statistical mechanics of complex networks*, Reviews of Modern Physics **74** (2002), no. 1, 47.

[3] SE Alper, A Aydemir, and T Akin, *Stepped-etching for preserving critical dimensions in through-wafer deep reactive ion etching of thick silicon*, Solid-State Sensors, Actuators and Microsystems Conference, 2009. TRANSDUCERS 2009. International, IEEE, 2009, pp. 1110–1113.

[4] Shelley L. Anna, Nathalie Bontoux, and Howard A. Stone, *Formation of dispersions using "flow focusing" in microchannels*, Applied Physics Letters **82** (2003), no. 3, 364–366.

[5] Alex Arenas, Albert Díaz-Guilera, Jurgen Kurths, Yamir Moreno, and Changsong Zhou, *Synchronization in complex networks*, Physics Reports **469** (2008), no. 3, 93–153.

[6] Stefano Boccaletti, Vito Latora, Yamir Moreno, Martin Chavez, and D-U Hwang, *Complex networks: Structure and dynamics*, Physics Reports **424** (2006), no. 4, 175–308.

[7] V. Castets, E. Dulos, J. Boissonade, and P. De Kepper, *Experimental evidence of a sustained standing turing-type nonequilibrium chemical pattern*, Physical Review Letters **64** (1990), 2953–29565.

[8] Irene ChouáChen, Krystyn J áVan Vliet, et al., *Shape-and size-dependent patterns in self-oscillating polymer gels*, Soft Matter **7** (2011), no. 7, 3141–3146.

[9] V. Colizza, R. Pastor-Satorras, and V.A. Vespignani, *Reaction-diffusion processes and metapopulation models in heterogeneous networks*, Nature Physics **3** (2007), 276–282.

[10] Michael Cross and Henry Greenside, *Pattern formation and dynamics in nonequilibrium systems*, first ed., Cambridge University Press, 2009.

[11] Michael F. Crowley and Irving R. Epstein, *Experimental and theoretical studies of a coupled chemical oscillator: Phase death, multistability, and in-phase and out-of-phase entrainment*, Journal of Physical Chemistry **93** (1989), 2496–2502.

[12] G. Dechert, K.-P. Lebender, and F. W. Schneider, *Recognition of phase patterns in a chemical reactor network*, Journal of Physical Chemistry **100** (1996), 19043–19048.

[13] Jorge Delgado, Ning Li, Marcin Leda, Hector O. González-Ochoa, Seth Fraden, and Irving R. Epstein, *Coupled oscillations in a 1D emulsion of Belousov-Zhabotinsky droplets*, Soft Matter **7** (2011), 3155–3167.

[14] Dell Inc., *Dell 1210s projector user's guide*, 2009.

[15] Tao Deng, Yung-Hoon Ha, Joy Y. Cheng, C. A. Ross, and Edwin L. Thomas, *Micropatterning of block copolymer solutions*, Langmuir **18** (2002), no. 18, 6719–6722.

[16] M. Dolnik and M. Marek, *Extinction of oscillations in forced and coupled reaction cells*, Journal of Physical Chemistry **92** (1988), 2452–2455.

[17] Florian Dörfler and Francesco Bullo, *Synchronization in complex networks of phase oscillators: A survey*, Automatica **50** (2014), no. 6, 1539–1564.

[18] Florian Dörfler, Michael Chertkov, and Francesco Bullo, *Synchronization in complex oscillator networks and smart grids*, Proceedings of the National Academy of Sciences **110** (2013), no. 6, 2005–2010.

[19] I. R. Epstein and J. A. Pojman, *Introduction to nonlinear chemical dynamics. oscillations, waves, patterns and chaos*, Oxford University Press, New York, 1998.

[20] Irving R. Epstein, *Can droplets and bubbles think?*, Science **315** (2007), 775–775.

[21] Irving R. Epstein and Vladimir K. Vanag, *Complex patterns in reactive microemulsions: Self-organized nanostructures?*, Chaos **15** (2005), 047510.

[22] G. Bard Ermentrout, *An adaptive model for synchrony in the firefly pteroptyx malaccae*, Journal of Mathematical Biology **29** (1991), no. 6, 571–585.

[23] G. Bard Ermentrout and David H. Terman, *Mathematical foundations of neuroscience*, first ed., Springer, 2010.

[24] R. J. Field and M. Burger, *Oscillations and traveling waves in chemical systems*, Wiley, New York, 1985.

[25] Richard J. Field, Endre Körös, and Richard M. Noyes, *Oscillations in chemical systems. II. thorough analysis of temporal oscillation in the bromate-cerium-malonic acid system*, Journal of the American Chemical Society **94** (1972), no. 25, 8649–8664.

[26] Richard J. Field and Richard M. Noyes, *Oscillations in chemical systems. IV. limit cycle behavior in a model of a real chemical reaction*, The Journal of Chemical Physics **60** (1974), no. 5, 1877–1884.

[27] Jean-Marc Flesselles, Andrew Belmonte, and Vilmos Gáspaár, *Dispersion relation for waves in the Belousov-Zhabotinsky reaction*, Journal of the Chemical Society, Faraday Transactions **94** (1998), no. 7, 851–855.

[28] H. Fukuda, H. Morimura, and S. Kai, *Global synchronization in two-dimensional lattices of discrete Belousov-Zhabotinsky oscillators*, Physica D - Nonlinear Phenomena **205** (2005), 80–86.

[29] Hirokazu Fukuda, Naoki Tamari, Hiroki Morimura, and Shoichi Kai, *Entrainment in a chemical oscillator chain with a pacemaker*, Journal of Physical Chemistry A **109** (2005), 11250–11254.

[30] Jianxi Gao, Yang-Yu Liu, Raissa M D'Souza, and Albert-László Barabási, *Target control of complex networks*, Nature Communications **5** (2014), 1–8.

[31] V. Gáspár, G. Bazsa, and M. T. Beck, *The influence of visible light on the Belousov–Zhabotinskii oscillating reactions applying different catalysts*, Zeitschrift für Physikalische Chemie **264** (1983), 43–48.

[32] P. Glandsdorff and I. Prigogine, *Thermodynamic theory of structure, stability and fluctuations*, Wiley, 1971.

[33] László Györgyi, Tamás Turányi, and Richard J. Field, *Mechanistic details of the oscillatory Belousov-Zhabotinskii reaction*, Journal of Physical Chemistry **94** (1990), 7162–7170.

[34] László Hegedűs, Mária Wittmann, Zoltán Noszticzius, Shuhua Yan, Atchara Sirimungkala, Horst-Dieter Försterling, and Richard J. Field, *Hplc analysis of complete BZ systems. evolution of the chemical composition in cerium and ferroin catalysed batch oscillators: experiments and model calculations*, Faraday Discussions **120** (2001), 21–38.

[35] C. Holtze, A. C. Rowat, J. J. Agresti, J. B. Hutchison, F. E. Angilè, C. H. J. Schmitz, S. Köster, H. Duan, K. J. Humphry, R. A. Scanga, J. S. Johnson, D. Pisignano, and D. A. Weitz, *Biocompatible surfactants for water-in-fluorocarbon emulsions*, Lab on a Chip **8** (2008), 1632–1639.

[36] Judit Horváth, István Szalai, and Patrick De Kepper, *An experimental design method leading to chemical turing patterns*, Science **324** (2009), 772–775.

[37] Filip Ilievski, Aaron D Mazzeo, Robert F Shepherd, Xin Chen, and George M Whitesides, *Soft robotics for chemists*, Angewandte Chemie **123** (2011), no. 8, 1930–1935.

[38] Masafumi Inaba, Hiroaki Yamanaka, and Shigeru Kondo, *Pigment pattern formation by contact-dependent depolarization*, Science **335** (2012), 677.

[39] Jacob N. Israelachvili, *Intermolecular and surface forces*, third ed., Academic Press, 2011.

[40] Kazuyoshi Itoga, Jun Kobayashi, Masayuki Yamato, Akihiko Kikuchi, and Teruo Okano, *Maskless liquid-crystal-display projection photolithography for improved design flexibility of cellular micropatterns*, Biomaterials **27** (2006), 3005–3009.

[41] Kazuyoshi Itoga, Masayuki Yamato, Jun Kobayashi, Akihiko Kikuchi, and Teruo Okano, *Cell micropatterning using photopolymerization with a liquid crystal device commercial projector*, Biomaterials **25** (2004), 2047–2053.

[42] Eugene M Izhikevich, *Dynamical systems in neuroscience*, first ed., MIT press, 2007.

[43] Eric Karsenti, *Self-organization in cell biology: a brief history*, Nature Reviews Molecular Cell Biology **9** (2008), 255–262.

[44] Hua Ke, Mark R. Tinsley, Aaron Steele, Fang Wang, and Kenneth Showalter, *Link weight evolution in a network of coupled chemical oscillators*, Physical Review E **89** (2014), no. 5, 052712.

[45] Sangbae Kim, Cecilia Laschi, and Barry Trimmer, *Soft robotics: a bioinspired evolution in robotics*, Trends in Biotechnology **31** (2013), no. 5, 287–294.

[46] István Z. Kiss, Craig G. Rusin, Hiroshi Kori, and John L. Hudson, *Engineering complex dynamical structures: Sequential patterns and desynchronization*, Science **316** (2007), no. 5833, 1886–1889.

[47] István Z. Kiss, Yumei Zhai, and John L. Hudson, *Emerging coherence in a population of chemical oscillators*, Science **296** (2002), 1676–1678.

[48] Shigeru Kondo and Takashi Miura, *Reaction-diffusion model as a framework for understanding biological pattern formation*, Science **329** (2010), 1616–1620.

[49] Nancy Kopell and G. Bard Ermentrout, *Coupled oscillators and the design of central pattern generators*, Mathematical Biosciences **90** (1988), no. 1, 87–109.

[50] Hiroshi Kori, Craig G Rusin, István Z. Kiss, and John L. Hudson, *Synchronization engineering: Theoretical framework and application to dynamical clustering*, Chaos **18** (2008), no. 2, 026111.

[51] L. Kuhnert, K. I. Agladze, and V. I. Krinsky, *Image processing using light-sensitive chemical waves*, Nature **337** (1989), 244–247.

[52] Yoshiki Kuramoto, *Chemical oscillations, waves and turbulence*, Springer, Berlin; New York, 1984.

[53] ———, *Chemical oscillations, waves, and turbulence*, second ed., Dover, 2003.

[54] F Laerme, Andrea Schilp, Karsten Funk, and MAOM Offenberg, *Bosch deep silicon etching: improving uniformity and etch rate for advanced mems applications*, Micro Electro Mechanical Systems, 1999. MEMS'99. Twelfth IEEE International Conference on, IEEE, 1999, pp. 211–216.

[55] Jean Pierre Laplante and Thomas Erneux, *Propagation failure in arrays of coupled bistable chemical reactors*, The Journal of Physical Chemistry **96** (1992), no. 12, 4931–4934.

[56] Jessamine Ng Lee, Cheolmin Park, and George M. Whitesides, *Solvent compatibility of poly(dimethylsiloxane)-based microfluidic devices*, Analytical Chemistry **75** (2003), no. 23, 6544–6554.

[57] István Lengyel and Irving R. Epstein, *Diffusion-induced instability in chemically reacting systems: steady state multiplicity, oscillation, and chaos*, Chaos **1** (1991), no. 1, 69–76.

[58] Ang Li, Meng Chen, Ting-Xin Jiang, Ping Wu, Qing Nie, Randall Widelitz, and Cheng-Ming Chuong, *Shaping organs by a wingless-int/notch/nonmuscle myosin module which orients feather bud elongation*, Proceedings of the National Academy of Sciences of the United States of America **110** (2013), E1452–61.

[59] Ning Li, Nathan Tompkins, Hector Gonzalez-Ochoa, and Seth Fraden, *Tunable diffusive lateral inhibition in chemical cells*, The European Physical Journal E **38** (2015), no. 3, 1–12.

[60] Anna L. Lin, Matthias Bertram, Karl Martinez, and Harry L. Swinney, *Resonant phase patterns in a reaction-diffusion system*, Physical Review Letters **84** (2000), no. 18, 4240–4243.

[61] Anna L. Lin, Aric Hagberg, Ehud Meron, and Harry L. Swinney, *Resonance tongues and patterns in periodically forced reaction-diffusion systems*, Physical Review E **69** (2004), 1–10.

[62] Yang-Yu Liu, Jean-Jacques Slotine, and Albert-László Barabási, *Controllability of complex networks*, Nature **473** (2011), no. 7346, 167–173.

[63] Yi Lu, Gazell Mapili, Gerry Suhali, Shaochen Chen, and Krishnendu Roy, *A digital micro-mirror device-based system for the microfabrication of complex, spatially patterned tissue engineering scaffolds*, Journal of Biomedical Materials Research **77A** (2006), 396–405.

[64] P. K. Maini, Ruth E. Baker, and C. M. Chuong, *The Turing model comes of molecular age*, Science **314** (2006), 1397–1398.

[65] Milos Marek and Ivan Stuchl, *Synchronization in two interacting oscillatory systems*, Biophysical Chemistry **3** (1975), 241–248.

[66] Erik Andreas Martens, Shashi Thutupalli, Antoine Fourrière, and Oskar Hallatschek, *Chimera states in mechanical oscillator networks*, Proceedings of the National Academy of Sciences **110** (2013), no. 26, 10563–10567.

[67] MathWorks, *Matlab "imopen" documentation*, 2015, [Online; accessed 18-January-2015].

[68] Hans Meinhardt, *Turing's theory of morphogenesis of 1952 and the subsequent discovery of the crucial role of local self-enhancement and long-range inhibition*, Interface Focus **2** (2012), no. 4, 407–416.

[69] Vicenc Mendez, Sergei Fedotov, and Werner Horsthemke, *Reaction-transport systems: Mesoscopic foundations, fronts, and spatial instabilities*, Springer, Berlin, Heidelberg, 2010.

[70] Ludovico Minati, *Experimental synchronization of chaos in a large ring of mutually coupled single-transistor oscillators: Phase, amplitude, and clustering effects*, Chaos **24** (2014), no. 4, 043108.

[71] Yoshio Mita, Masakazu Sugiyama, Masanori Kubota, Frederic Marty, Tarik Bourouina, and Tadashi Shibata, *Aspect ratio dependent scalloping attenuation in drie and an application to low-loss fiber-optical switches*, Micro Electro Mechanical Systems, 2006. MEMS 2006 Istanbul. 19th IEEE International Conference on, IEEE, 2006, pp. 114–117.

[72] Kenji Miyakawa, Taiji Okano, and Shoji Yamazaki, *Cluster synchronization in a chemical oscillator network with adaptive coupling*, Journal of the Physical Society of Japan **82** (2013), no. 3, 034005.

[73] Luis G. Morelli, Koichiro Uriu, Saul Ares, and Andrew C. Oates, *Computational approaches to developmental patterning*, Science **336** (2012), 187–191.

[74] P. Müller, K. W. Rogers, B. M. Jordan, J. S. Lee, D. Robson, S. Ramanathan, and A. F. Schier, *Differential diffusivity of Nodal and Lefty underlies a reaction-diffusion patterning system*, Science **336** (2012), 721–724.

[75] J. David Musgraves, Brett T. Close, and David M. Tanenbaum, *A maskless photolithographic prototyping system using a low-cost consumer projector and a microscope*, American Journal of Physics **73** (2005), no. 10, 980–983.

[76] Raphael Nagao, Irving R Epstein, and Milos Dolnik, *Forcing of Turing patterns in the chlorine dioxide–iodine–malonic acid reaction with strong visible light*, The Journal of Physical Chemistry A **117** (2013), no. 38, 9120–9126.

[77] Thomas Naiser, Timo Mai, Wolfgang Michel, and Albrecht Ott, *Versatile maskless microscope projection photolithography system and its application in light-directed fabrication of dna microarrays*, Review of Scientific Instruments **77** (2006), no. 6, 063711.

[78] H. Nakao and A.S. Mikhailov, *Turing patterns in network-organized activator-inhibitor systems*, Nature Physics **6** (2010), 544–550.

[79] NEC Display Solutions, Ltd., *Lcd projector np3150/np2150/np1150 user's manual*, 2007.

[80] NEC Display Solutions, Ltd., *Portable projector vt800 user's manual*, 2008.

[81] Zoltán Néda, Erzsébet Ravasz, Tamás Vicsek, Yves Brechet, and Albert-Lázló Barabási, *Physics of the rhythmic applause*, Physical Review E **61** (2000), no. 6, 6987.

[82] Martinus Nijhoff (ed.), *Oeuvres complètes de christiaan huygens*, vol. 5, p. 246, Societe Hollandaise des Sciences, 1893.

[83] Z. Noszticzius, Werner Horsthemke, W. D. McCormick, Harry L Swinney, and W. Y. Tam, *Sustained chemical waves in an annular gel reactor*, Nature **329** (1987), 619–620.

[84] Richard M. Noyes, Richard J. Field, and Endre Körös, *Oscillations in chemical systems. I. detailed mechanism in a system showing temporal oscillations*, Journal of the American Chemical Society **94** (1972), no. 4, 1394–1395.

[85] Taiji Okano, Akane Kitagawa, and Kenji Miyakawa, *Array-enhanced coherence resonance and phase synchronization in a two-dimensional array of excitable chemical oscillators*, Physical Review E **76** (2007), 1–6.

[86] Taiji Okano and Kenji Miyakawa, *Feedback-controlled dynamics in a two-dimensional array of active elements*, Physical Review E **80** (2009), 1–6.

[87] HG Othmer and LE Scriven, *Instability and dynamic pattern in cellular networks*, Journal of Theoretical Biology **32** (1971), no. 3, 507–537.

[88] Q. Ouyang and H. L. Swinney, *Transition from a uniform state to hexagonal and striped Turing patterns*, Nature **352** (1991), 610–612.

[89] James Pantaleone, *Synchronization of metronomes*, American Journal of Physics **70** (2002), no. 10, 992–1000.

[90] Valery Petrov, Qi Ouyang, and Harry L. Swinney, *Resonant pattern formation in a chemical system*, Nature **388** (1997), 655–657.

[91] Arkady Pikovsky, Michael Rosenblum, and Jürgen Kurths, *Synchronization: A universal concept in nonlinear sciences*, first ed., Cambridge University Press, 2001.

[92] J. Reinitz, *Pattern formation: Turing at 100*, Nature **482** (2012), 2012.

[93] Martin Rohden, Andreas Sorge, Marc Timme, and Dirk Witthaut, *Self-organized synchronization in decentralized power grids*, Physical Review Letters **109** (2012), no. 6, 064101.

[94] Martin Rohden, Andreas Sorge, Dirk Witthaut, and Marc Timme, *Impact of network topology on synchrony of oscillatory power grids*, Chaos: An Interdisciplinary Journal of Nonlinear Science **24** (2014), no. 1, 013123.

[95] J.-C. Roux, Reuben H. Simoyi, and Harry L. Swinney, *Observation of a strange attractor*, Physica D **8** (1983), 257–266.

[96] Craig G Rusin, Hiroshi Kori, István Z. Kiss, and John L. Hudson, *Synchronization engineering: tuning the phase relationship between dissimilar oscillators using nonlinear feedback*, Philosophical Transactions of the Royal Society A **368** (2010), no. 1918, 2189–2204.

[97] Craig G Rusin, Isao Tokuda, István Z. Kiss, and John L. Hudson, *Engineering of synchronization and clustering of a population of chaotic chemical oscillators*, Angewandte Chemie International Edition **50** (2011), no. 43, 10212–10215.

[98] John C. Russ, *The image processing handbook*, 6 ed., CRC Press, 2011.

[99] R. A. Schmitz, K. R. Graziani, and John L. Hudson, *Experimental evidence of chaotic states in the Belousov-Zhabotinskii reaction*, Journal of Chemical Physics **67** (1977), no. 7, 3040–3044.

[100] Jakob Schweizer, Martin Loose, Mike Bonny, Karsten Kruse, Ingolf Mönch, and Petra Schwille, *Geometry sensing by self-organized protein patterns*, Proceedings of the National Academy of Sciences of the United States of America **109** (2012), 15283–8.

[101] Reuben H. Simoyi, Alan Wolf, and Harry L. Swinney, *One-dimensional dynamics in a multicomponent chemical reaction*, Physical Review Letters **49** (1982), no. 4, 245–248.

[102] Sangeet Singh-Gasson, Roland D Green, Yongjian Yue, Clark Nelson, Fred Blattner, Michael R Sussman, and Franco Cerrina, *Maskless fabrication of light-directed oligonucleotide microarrays using a digital micromirror array*, Nature Biotechnology **17** (1999), no. 10, 974–978.

[103] Frances K. Skinner, Nancy Kopell, and Eve Marder, *Mechanisms for oscillation and frequency control in reciprocally inhibitory model neural networks*, Journal of Computational Neuroscience **1** (1994), 69–87.

[104] Oliver Steinbock, Ágota Tóth, and Kenneth Showalter, *Navigating complex labyrinths: optimal paths from chemical waves*, Science **267** (1995), 868–871.

[105] Jeffrey N Stirman, Matthew M Crane, Steven J Husson, Sebastian Wabnig, Christian Schultheis, Alexander Gottschalk, and Hang Lu, *Real-time multimodal optical control of neurons and muscles in freely behaving Caenorhabditis elegans*, Nature Methods **8** (2011), no. 2, 153–159.

[106] Christopher Stone, Rita Toth, Ben de Lacy Costello, Larry Bull, and Andrew Adamatzky, *Coevolving cellular automata with memory for chemical computing: Boolean logic gates in the BZ reaction*, Parallel Problem Solving from Nature–PPSN X, Springer, 2008, pp. 579–588.

[107] Steven H. Strogatz, *Nonlinear dynamics and chaos*, first ed., Westview Press, 1994.

[108] ———, *Exploring complex networks*, Nature **410** (2001), no. 6825, 268–276.

[109] ———, *Sync: how order emerges from chaos in the universe, nature, and daily life*, first ed., Hyperion, 2003.

[110] Steven H. Strogatz, Daniel M. Abrams, Allan McRobie, Bruno Eckhardt, and Edward Ott, *Theoretical mechanics: Crowd synchrony on the millennium bridge*, Nature **438** (2005), no. 7064, 43–44.

[111] Ivan Stuchl and Miloš Marek, *Dissipative structures in coupled cells: Experiments*, The Journal of Chemical Physics **77** (1982), no. 6, 2956–2963.

[112] Annette F. Taylor, Mark R. Tinsley, Fang Wang, Zhaoyang Huang, and Kenneth Showalter, *Dynamical quorum sensing and synchronization in large populations of chemical oscillators*, Science **323** (2009), 614–617.

[113] Shashi Thutupalli, Ralf Seemann, and Stephan Herminghaus, *Simple model squirmers with tunable velocity*, arXiv (2011), 1–4.

[114] Mark R. Tinsley, Simbarashe Nkomo, and Kenneth Showalter, *Chimera and phase-cluster states in populations of coupled chemical oscillators*, Nature Physics **8** (2012), no. 9, 662–665.

[115] Mark R. Tinsley, Annette F. Taylor, Zhaoyang Huang, Fang Wang, and Kenneth Showalter, *Dynamical quorum sensing and synchronization in collections of excitable and oscillatory catalytic particles*, Physica D **239** (2010), 785–790.

[116] Masahiro Toiya, Hector O. González-Ochoa, Vladimir K. Vanag, Seth Fraden, and Irving R. Epstein, *Synchronization of chemical micro-oscillators*, Journal of Physical Chemistry Letters **1** (2010), 1241–1246.

[117] Masahiro Toiya, Vladimir K. Vanag, and Irving R. Epstein, *Diffusively coupled chemical oscillators in a microfluidic assembly*, Angewandte Chemie International Edition **47** (2008), 7753–7755.

[118] Nathan Tompkins, Matthew Carl Cambria, Adam L. Wang, and Seth Fraden, *Creation and perturbation of planar networks of chemical oscillators*, under review at Chaos **x** (2015), no. x, x–x.

[119] Nathan Tompkins and Seth Fraden, *A programmable illumination microscope from low-cost and reused components*, under review at the American Journal of Physics **x** (2015), no. x, x–x.

[120] Nathan Tompkins, Ning Li, Camille Girabawe, Michael Heymann, G. Bard Ermentrout, Irving R. Epstein, and Seth Fraden, *Testing turing's theory of morphogenesis in chemical cells*, Proceedings of the National Academy of Sciences **111** (2014), no. 12, 4397–4402.

[121] Rita Toth and Annette F. Taylor, *The tris(2,2'-bipyridyl)ruthenium-catalysed Belousov–Zhabotinsky reaction*, Progress in Reaction Kinetics and Mechanism **31** (2006), no. 2, 59–115.

[122] Barry Trimmer, *A journal of soft robotics: Why now?*, Soft Robotics **1** (2014), no. 1, 1–4.

[123] Tamás Turányi, László Györgyi, and Richard J. Field, *Analysis and simplification of the GTF model of the Belousov-Zhabotinsky reaction*, Journal of Physical Chemistry **97** (1993), 1931–1941.

[124] A. M. Turing, *The chemical basis of morphogenesis*, Philosophical Transactions of the Royal Society of London **237** (1952), no. 641, 37–72.

[125] John J. Tyson and Paul C. Fife, *Target patterns in a realistic model of the Belousov-Zhabotinskii reaction*, The Journal of Chemical Physics **73** (1980), no. 5, 2224–2237.

[126] Vladimir K. Vanag and Irving R. Epstein, *Inwardly rotating spiral waves in a reaction-diffusion system*, Science **294** (2001), 835–837.

[127] ———, *Pattern formation in a tunable medium: The Belousov-Zhabotinsky reaction in an aerosol ot microemulsion*, Physical Review Letters **87** (2001), no. 22, 1–4.

[128] ———, *Diffusive instabilities in heterogeneous systems*, Journal of Chemical Physics **119** (2003), no. 14, 7297–7307.

[129] ———, *A model for jumping and bubble waves in the Belousov-Zhabotinsky-aerosol OT system*, Journal of Chemical Physics **131** (2009), 1–7.

[130] ———, *Periodic perturbation of one of two identical chemical oscillators couple via inhibition*, Physical Review E **81** (2010), 1–10.

[131] ———, *Excitatory and inhibitory coupling in a one-dimensional array of Belousov–Zhabotinsky micro-oscillators: Theory*, Physical Review E **84** (2011), 066209:1–11.

[132] Mahesh Wickramasinghe and István Z. Kiss, *Spatially organized dynamical states in chemical oscillator networks: Synchronization, dynamical differentiation, and chimera patterns*, PloS One **8** (2013), no. 11, e80586.

[133] ———, *Spatially organized partial synchronization through the chimera mechanism in a network of electrochemical reactions*, Physical Chemistry Chemical Physics **16** (2014), no. 34, 18360–18369.

[134] Arthur T. Winfree, *Spiral waves of chemical activity*, Science **175** (1971), 634–636.

[135] ———, *The prehistory of the Belousov-Zhabotinsky oscillator*, Journal of Chemical Education **61** (1984), no. 8, 661–663.

[136] ———, *The geometry of biological time*, second ed., Springer, 2001.

[137] ———, *On emerging coherence*, Science **298** (2002), 2336–2337.

[138] George B Witman, *Chlamydomonas phototaxis*, Trends in Cell Biology **3** (1993), no. 11, 403–408.

[139] M. Wolfrum, *The turing bifurcation in network systems: Collective patterns and single differentiated nodes*, Physica D-Nonlinear Phenomena **241** (2012), 1353–1357.

[140] Lingfa Yang, Milos Dolnik, Anatol M. Zhabotinsky, and Irving R. Epstein, *Oscillatory clusters in a model of the photosensitive Belousov-Zhabotinsky reaction system with global feedback*, Physical Review E **62** (2000), no. 5, 6414–6420.

[141] Lingfa Yang and Irving R. Epstein, *Oscillatory Turing patterns in reaction-diffusion systems with two coupled layers*, Physical Review Letters **90** (2003), no. 17, 1–4.

[142] Junghoon Yeom, Yan Wu, John C Selby, and Mark A Shannon, *Maximum achievable aspect ratio in deep reactive ion etching of silicon due to aspect ratio dependent transport and the microloading effect*, Journal of Vacuum Science & Technology B **23** (2005), no. 6, 2319–2329.

[143] A. N. Zaikin and A. M. Zhabotinsky, *Concentration wave propagation in two-dimensional liquid-phase self-oscillating system*, Nature **225** (1970), 535–537.

[144] Anatol M. Zhabotinsky, Frank Buchholtz, Anatol B. Kiyatkin, and Irving R. Epstein, *Oscillations and waves in metal-ion-catalyzed bromate oscillating reactions in highly oxidized states*, Journal of Physical Chemistry **97** (1993), 7578–7584.